# Understanding the Motions of the Cheetah Tail Using Robotics

Amir Patel
MSc (Eng) *Cape Town*

Thesis Presented for the Degree of
DOCTOR OF PHILOSOPHY
in the Department of Electrical Engineering
UNIVERSITY OF CAPE TOWN
August 2014

*To my wife, Ilhaam…*

# Declaration

I know the meaning of plagiarism and declare that all the work in the document, save for that which is properly acknowledged, is my own.

Signature of Author . . . . . . . . . . . . . . . . . . . . . . . . . . . . . . . . . . . . . . . . . . . . . .

26 August 2014

# Abstract

The cheetah is capable of incredible feats of manoeuvrability. But, what is interesting about these manoeuvres is that they involve rapid swinging of the animal's lengthy tail. Despite this, very little is understood about the cheetah tail and its motion, with the common view being that it is "heavy" and possibly used as a "counter balance" or as a "rudder".

In this dissertation, this subject is investigated by exploring the motions of the cheetah tail by means of mathematical models, feedback control and novel robot platforms. Particularly, the motion in the roll axis is first investigated and it is determined that it assists stability of high speed turns. This is validated by modelling and experimental testing on a novel tailed robot, *Dima I*. Inspired by cheetah video observations, the tail motion in the pitch axis during rapid acceleration and braking manoeuvres is also investigated. Once again modelling and experimental testing on a tailed robot are performed and the tail is shown to stabilise rapid acceleration manoeuvres. Video observations also indicate the tail movement in the shape of a cone: a combination of pitching and yawing. Understanding this motion is done by setting up an optimization problem. Here, the optimal motion was found to be to a cone which results in a continuous torque on the body during a turn while galloping. A novel two degree of freedom tailed robot, *Dima II,* was then developed to experimentally validate the effect of this motion.

Lastly, measurement of the cheetah tail inertia was performed during a routine necropsy where it was found to have lower inertia than assumed. However, the tail has thick, long fur that was tested in a wind tunnel. Here it was found that the furry tail is capable of producing significant drag forces without a weight penalty. Subsequently, mathematical models incorporating the aerodynamics of the tail were developed and these were used to demonstrate its effectiveness during manoeuvres.

# Acknowledgements

Firstly, I would like to thank the All Mighty for giving me the strength to always persevere and for all the opportunities I have been given. To my parents and sister, thank you for your unfailing support and assistance. Your encouragement has always been an asset to me.

I would like to thank my supervisor, Prof. Martin Braae for giving me my first exposure to Control Engineering. This truly shaped my thinking and indeed my career as an engineer. Thank you for all the support.

To my “adopted supervisor”, Prof. Ed Boje, I cannot express my gratitude to you as I am certain I would not have made it this far without our conversations and your steady guidance. Your enthusiasm for this thesis always inspired me to push the boundaries of my own understanding. I have learned so much from you and I hope to continue to do so.

To my friend, Callen Fisher, your unrelenting assistance and feedback have been essential to this project. We have seen cheetahs, spilled blood together and glued fur to plastic pipes… we have had adventures! I hope to do some incredible, novel and interesting research with you in the future.

I would also like to thank my cousin Javaad Patel for his support. You have taught me a great deal. The Dima robots would not be successful without the practical work done by Justin Coetser, James Gowans, Nick Hunt and Joseph Muziki. Thank you for all your hard work.

I would like to thank the staff of the Electrical Engineering Department particularly, Robyn Verrinder, A/Prof. Azeem Khan and Sammy Tsoeu for all your encouragement, support and advice. I would also like to thank Phillip Titus and Brendon Daniels for all their technical help.

Special thanks to Leeann Louis, Dr. Sandra Corr and Dr. Emily Lane for all the biological help with the cheetahs. Also, my gratitude goes out to Cheetah Outreach in Somerset West, for always being accommodating and allowing me access to film the animals.

Lastly, I would like to thank my wife, Ilhaam for her boundless patience throughout this PhD. *You are my centre when I spin away*…but now I am coming home.

# Table of Contents

# List of Figures

# List of Tables

# Chapter 1

## Introduction

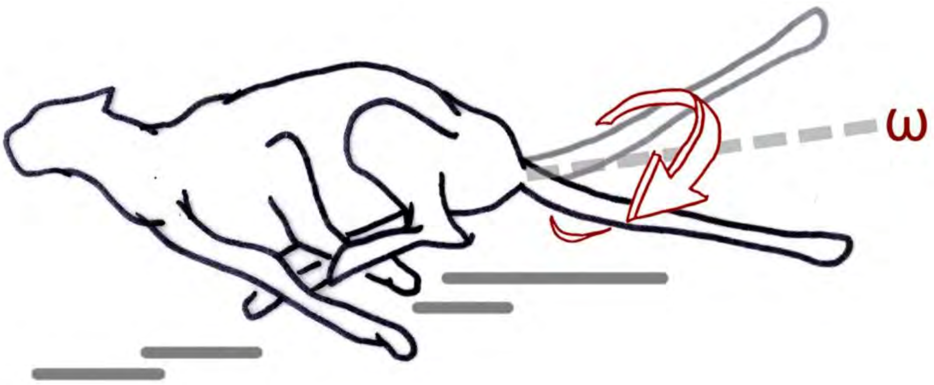

This thesis investigates the use of an actuated tail to aid manoeuvrability. The work is inspired by the agility of the cheetah and develops new knowledge in the understanding of the dynamics of the cheetah's tail. In addition, it contributes to knowledge in the engineering design of bio-inspired tailed robots, including modelling, control design, construction and practical testing.

## 1.1 Motivation

The cheetah (*Acinonyx jubatus*) is the fastest terrestrial animal [1]. However, a study by Wilson et al. [2] indicates that its true success in hunting can also be attributed to its ability to rapidly accelerate and manoeuvre during pursuit of its prey. Additionally, when one views these manoeuvres, the cheetah appears to be actively (and rapidly) swinging its lengthy tail in response to the prey's attempts at evasion (seen in Figure 1.1). Could it be using the tail to aid manoeuvrability? And if so, what would the neuromechanical strategy for doing so be?

Figure 1.1: Cheetahs performing various manoeuvres. The reader will note the apparent use of the tail. Images from National Geographic [3].

The public sphere of knowledge views the cheetah tail as being lengthy and muscular and is used as either a rudder, or counterweight which is employed for balance [4] [5] [6]. Indeed, the biological literature has also described the tail in a similar manner [7] [8]. However, the mechanisms for using the tail are still not well understood [9] [2].

In this dissertation, inspired by cheetah wildlife documentaries [5] [10] [11], an increased understanding of the various tail motions is pursued, especially during tasks requiring a high degree of manoeuvrability. In addition, the Cheetah Outreach conservation centre (Cape Town, South Africa) was visited by the Author during their weekly cheetah exercise runs to capture video footage. These exercises were observed and the footage analysed to determine to what degree there might be correlations between various tail motions and the corresponding manoeuvres.

The multi-disciplinary nature of this research necessitated that the motions be investigated via three approaches. These were:

1. Mathematical models, simulation and feedback control
2. Experimental validation on a physical model (high-speed terrestrial robot) and
3. Data gathered from a cheetah tail necropsy.

This shared and reciprocal approach can benefit both the fields of biology and robotics as depicted in Figure 1.2.

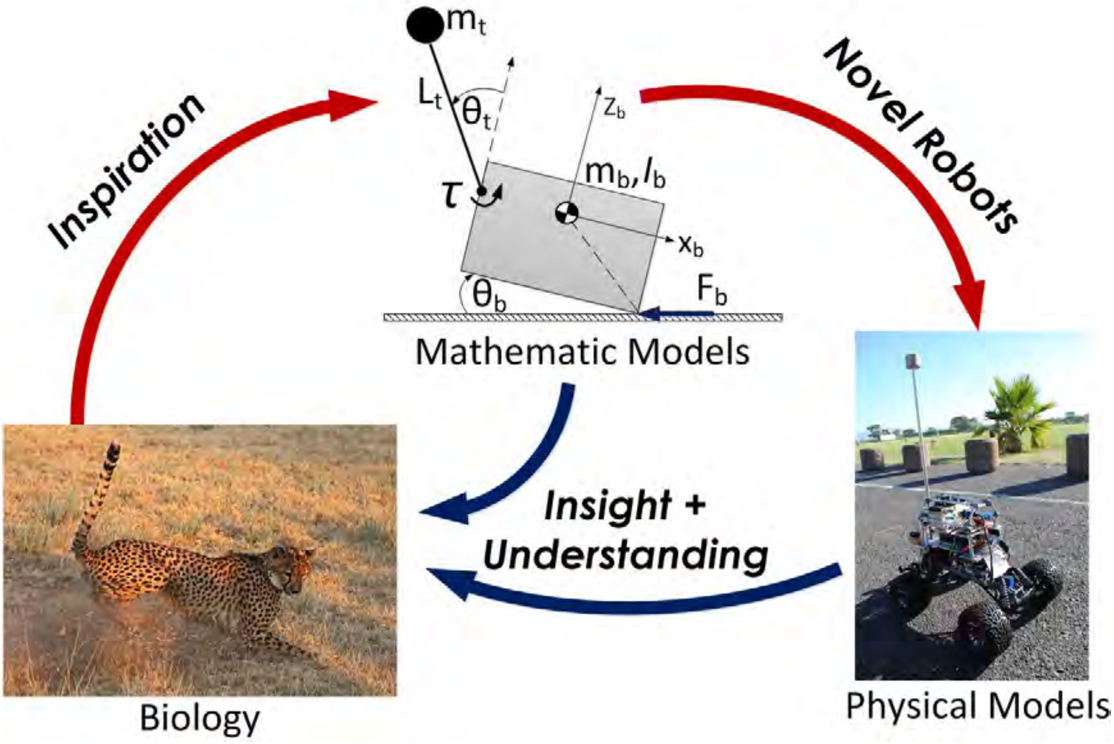

Figure 1.2: The mutualism between engineering and biology is fundamental to this dissertation.

During the observations of cheetah footage, four specific motions were selected for study:

1. Tail motion in the yaw axis
2. Tail motion in the roll axis
3. Tail motion in the pitch axis and
4. Tail motion in a cone (combination of pitch and yaw).

The first motion clearly results in a rapid yawing of the body especially while airborne. This effect has already been studied in the sprawling robots developed by Kohut et al. [12] [13]. Thus, it was decided not to investigate this, except to determine the aerodynamic effects during this motion as described in Chapter 5.

However, the remaining three motions were investigated to determine their dynamic effects on the cheetah body in the context of manoeuvrability. These investigations represent novel contributions to our understanding of the cheetah tail during rapid manoeuvres in terms of dynamic systems and feedback control. These studies also resulted in the development of two bio-spired robotic systems, *Dima I* [14] [15] and *Dima II* seen in Figure 1.3 on the next page.

Lastly, during the closing stages of this research, the Author was given the opportunity to participate in a cheetah necropsy to measure the tail inertia as its value was assumed up until then. The inertia measurement is described and it was discovered that the tail is not as heavy (relative to the body mass) as commonly believed. Simultaneously, a PhD thesis by Hudson [16] became available to the Author which further confirmed these inertia measurements (using a different method).

It should be emphasised that the research performed in Chapters 2, 3 and 4 was performed under the common view that the cheetah tail is heavy [4] [5] [6] and the robotic platform was built with a tail mass of 10% of the body mass as a result of this assumption. However, though this assumption was not accurate for the cheetah, it is believed that the insights gained from the mathematical models and experiments still remain valid.

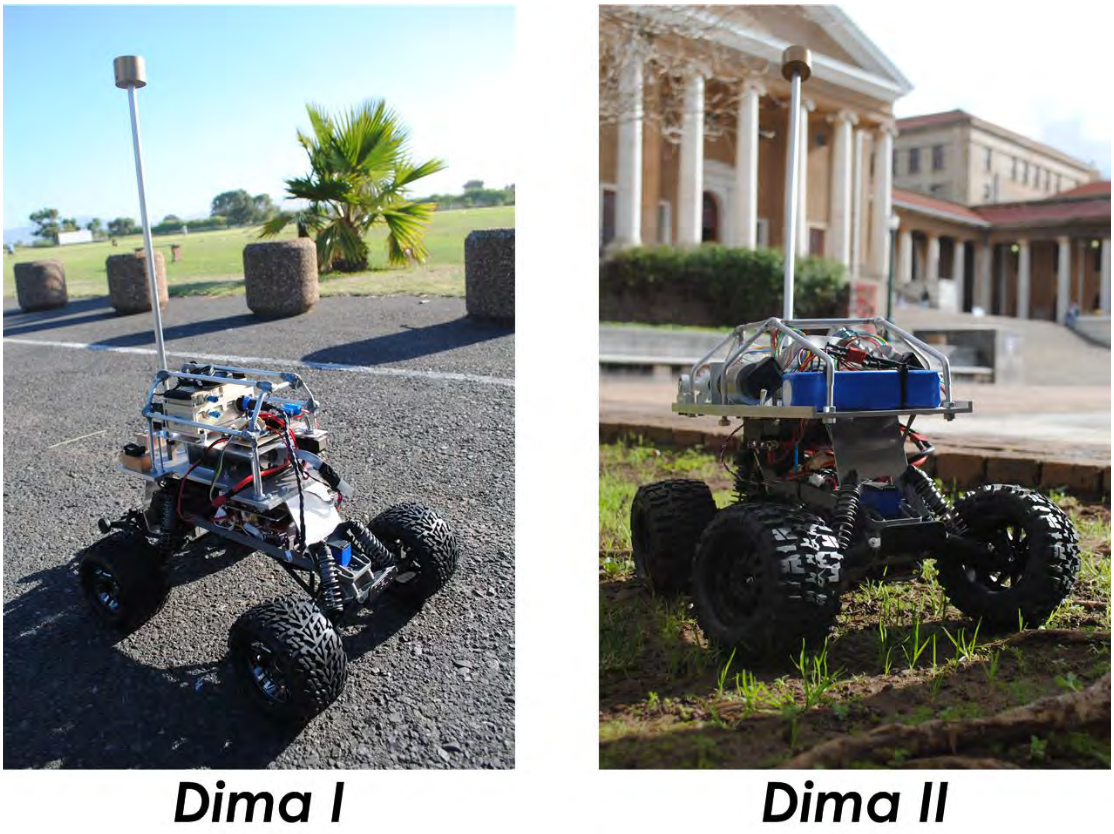
Dima I

Dima II

Figure 1.3: To investigate the motions of the cheetah tail, two novel robot platforms were developed using an off-the-shelf R/C truck. The first, *Dima I*, utilized a single degree of freedom tail. The second, *Dima II*, utilized a two degree of freedom tail.

The cheetah tail fur was available after this necropsy and was used to create an anatomically correct tail rig which was tested in a wind tunnel. It was confirmed that aerodynamic forces can also play a significant role to the actuation of the cheetah tail. This observation was subsequently investigated and further expanded by mathematical modelling.

As specified before, the general theme of this thesis is manoeuvrability. In the next subsection a definition of manoeuvrability is provided as well as a discussion of previous work on the subject.

## 1.2 Manoeuvrability

From a Biomechanical perspective, *manoeuvrability* is defined as an animal’s ability to change its velocity (angular and linear) in a controlled manner for a specific purpose [17] [18]. This can be seen as increasing or decreasing the magnitude of its velocity vector (acceleration and deceleration) or changing its direction (turning). The dexterity with which an animal can do so is crucial for its survival. However, as stated by Alexander [19], the biomechanics study of manoeuvrability has been relatively limited, with the significant portion of research concentrating on steady (periodic) locomotion such galloping, walking and trotting [20]. As a dynamic systems analogy, one can say that the research has focused on *steady state behaviour*, as opposed to *transient behaviour* as depicted by Figure 1.4. This could be attributed to the complex dynamics these transients comprise.

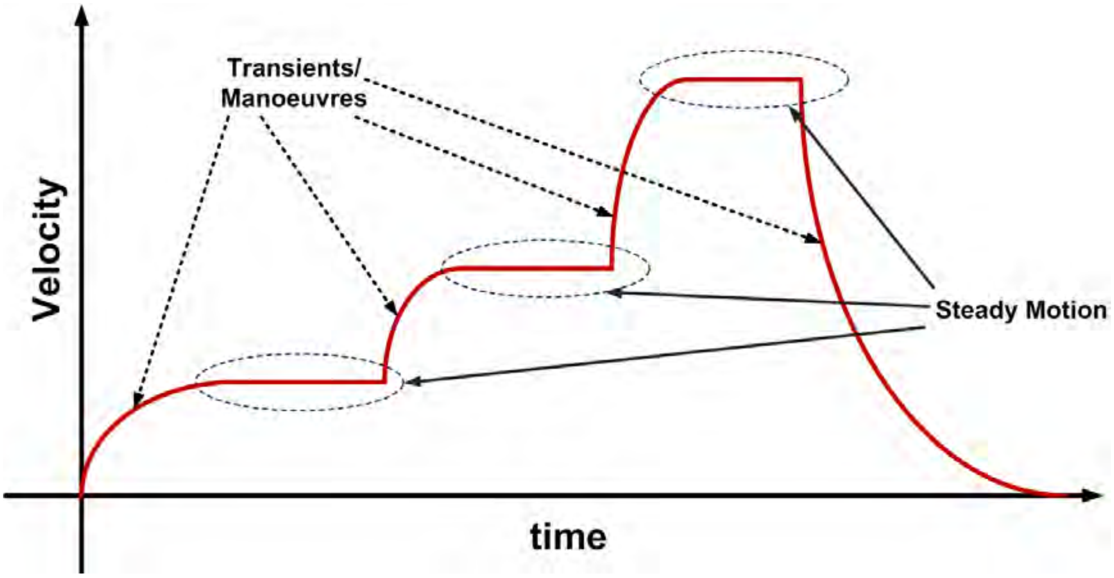

Figure 1.4: Manoeuvres can be considered as the transient dynamics of velocity. The biological literature has generally concentrated efforts on steady motion such as walking, galloping and trotting.

Nevertheless, some outstanding new contributions have been made in this regard for terrestrial animals. The Pitch Avoidance Model [21] developed by Williams et al. essentially determined that quadruped animals limit their deceleration and acceleration to avoid toppling over. In their paper they demonstrate that at low velocities, quadruped acceleration is not limited by muscle power, but in fact by their tendency to pitch nose up (or down). This is similar to torque limiting to avoid “popping a wheely” in motorcycles.

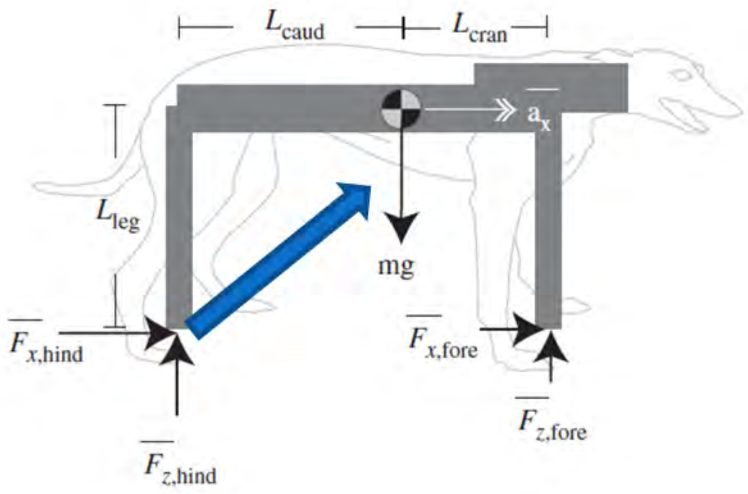

Figure 1.5: Pitch then Power Model free body diagram. If the ground reaction force (GRF) vector (blue arrow) passes in front of the centre of mass, a toppling moment will be experienced. Image adapted from [21].

To describe the kinematics of a greyhound accelerating, Angle et al. [20] developed a model based on high-speed camera data. In their paper they describe the exact motions (in the sagittal plane) that enable a greyhound to accelerate before reaching a gallop. The same authors continued their research on manoeuvrability in greyhounds and went on to study the effects of slipping and friction during these rapid acceleration manoeuvres [22]. Other studies have investigated the acceleration ability of dogs [23] [24] [25], turning ability in horses [26], non-steady locomotion of goats [27], rapid side-stepping of ostriches [28] and the kinetics of turning in chipmunks [29].

Surprisingly, the ability of a cheetah to manoeuvre and the mechanisms it employs are sparsely investigated. Only recently a study was published in the journal Nature by Wilson et al. [2] where the authors built custom tracking collars containing both an Inertial Measurements Unit (IMU) and a GPS to track wild cheetahs in Botswana. Utilizing the data gathered over several months, they determined that in general cheetahs do not run at their top speed as the fastest speed observed was 25.8 m/s[1]. However, the successes of hunts were characterized by relying on an ability to manoeuvre with accelerations up to 18 m/s$^2$. Also employing GPS collars and accelerometers, [30] determined that cheetahs match their acceleration according to the prey being pursued. The functional anatomy of the cheetah hind limb [31] and forelimb [32] has also been investigated. These studies revealed that the limbs appear to be more adapted to resist large ground reaction force (GRF) torques when

---

[1] Compared to the fastest recorded cheetah speed of 29 m/s [1].

compared to another sprinter, the greyhound. Evidently, no biological publications to date have specifically investigated the mechanics of the cheetah tail in the context of manoeuvrability.

The quadruped robotics community has also not explicitly investigated agility and manoeuvrability as stated by Bowling [33]. At present, steady state motions such as bounding, trotting, galloping and turning at low-speed have successfully been implemented by various researchers [34] [35] [36]. Indeed, a high speed quadruped robot has been developed by Boston Dynamics [37], capable of reaching over 12 m/s (and in so doing, breaking the legged robot speed record) as seen in Figure 1.6. But here again, the focus is on reaching a top speed and not explicitly on manoeuvrability performance.

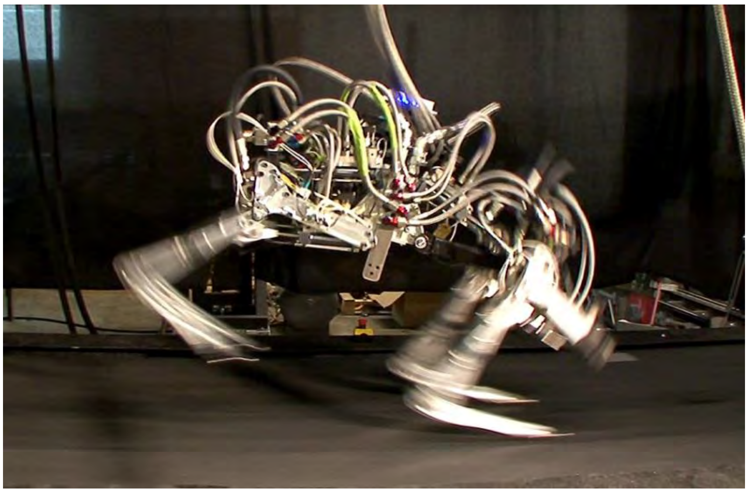

Figure 1.6: Boston Dynamics Cheetah: The fastest legged robot [37].

## 1.3 Tails in Biology and Robots

As mentioned previously, no literature (to this author's knowledge) exists on the biomechanics of the cheetah tail. However, studies have shown that actuated tails can enable air-righting reflexes in geckos [38] [39] (seen in Figure 1.7), balance in house cats [40] and aiding acrobatic manoeuvres in rodents [41] and primates [42]. These effects are attributed to inertial forces imparted by the tail on to the body.

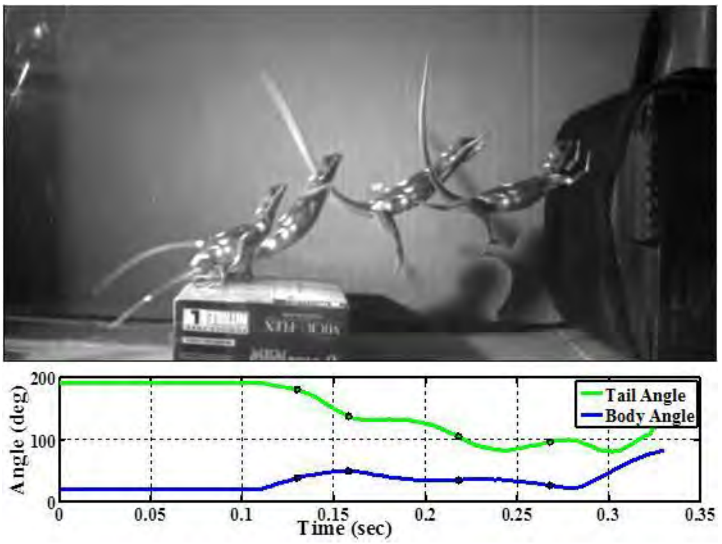

Figure 1.7: Image of lizard employing its tail for in air pitch control from Libby et al. [39].

The robotics community has in recent years seen a surge of research into the use inertial tails on robot platforms for aerial attitude control [43] [44] [12] [45]. Here, the active tails are employed during the aerial phase where the momentum is assumed to be conserved in the body-tail system.

Particularly, Chang-Siu et al. [43] demonstrated successful pitch control using a single degree-of-freedom tail has been demonstrated on Tailbot as seen in Figure 1.8. These authors have shown that for short time periods (less than 0.5s), an active tail is more optimal than a reaction wheel due to the greater moment of inertia (MOI) of the tail. This result has been further confirmed in a study by Briggs et al. [46], where despite the stroke limitations of tails, they can indeed impart greater angular impulse on the body than reaction wheels. These authors also experimentally demonstrate disturbance rejection (at stand still) by employing an active tail on their cheetah inspired robot as well as simulation of a tail based attitude controller. The same paper also hypothesises that the tail could be used to roll the cheetah body in air before a turn.

More recently, Chang et al. have further extended in-air attitude control to three dimensions by employing a two degree of freedom tail in conjunction with a nonlinear controller [47]. Also, in a monopedal hopping robot, De et al. [48] demonstrate that an actuated tail can successfully stabilize hopping by injecting energy into the leg spring by swinging the tail.

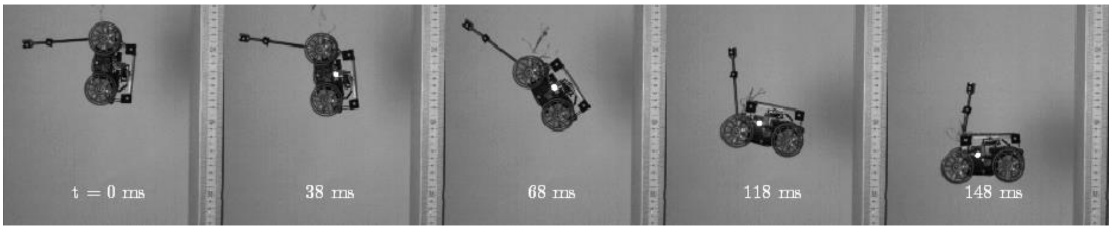

Figure 1.8: Berkley's Tailbot performing an aerial righting manoeuvre by means of swinging its tail [43].

Regarding tails for manoeuvrability (as defined in Section 1.2), Kohut et al. [13] have successfully employed an active inertial tail to initiate rapid turns on a sprawling hexapod robot, TAYLRoACH. Swinging the tail in the yaw axis has also been demonstrated on a miniature hexapod by Casarez et al. [49] for rapid turning. Continuing the research on TAYLRoACH, Kohut et al. have developed SailRoACH [50], which employs a purely aerodynamic tail, to change direction much like the rudder of a ship or aeroplane in the air. It should be noted that this is the only robot (to the Author's knowledge) to employ aerodynamic forces as opposed to inertial. Lastly, Patel and Braae [51] have demonstrated that an actuated tail can increase the acceleration capability of a simulated quadruped robot.

As is evident, the majority of research in active tails for robots has focused on in-air attitude control. Furthermore, most (except [50]) have employed the inertial forces imparted by a tail.

## 1.4 Research Approach

The manoeuvrability-stability dichotomy [52] [53] is well understood in the literature, where it is observed that for a system to be capable of fast changes in state (i.e. to be *manoeuvrable*), a certain amount of *destabilization* is required. What this implies is that for an animal to become more manoeuvrable, instability will naturally occur and without a mechanism to counteract this, stable manoeuvres will not be possible. It is the belief here that the cheetah could be using the tail to add capability and to stabilize these highly dynamic manoeuvres.

An essential tool for the mathematical modelling utilized in this thesis is the idea of Templates and Anchors, which was first proposed by Full and Koditschek [54]. Here, the notion is to capture the desired behaviour of the animal by employing the simplest mathematical model (*template),* while an *anchor* would be a more complex, representative model of the morphology of the animal or robot. The paradigm is that although animals consist of many degrees of freedom, there exists a collapse of dimensional space during locomotion tasks. This concept is illustrated in Figure 1.9. An example of an established template is the Spring Loaded Inverted Pendulum (SLIP) model [55], which although simple, effectively captures the centre of mass dynamics of many terrestrial animals and robots.

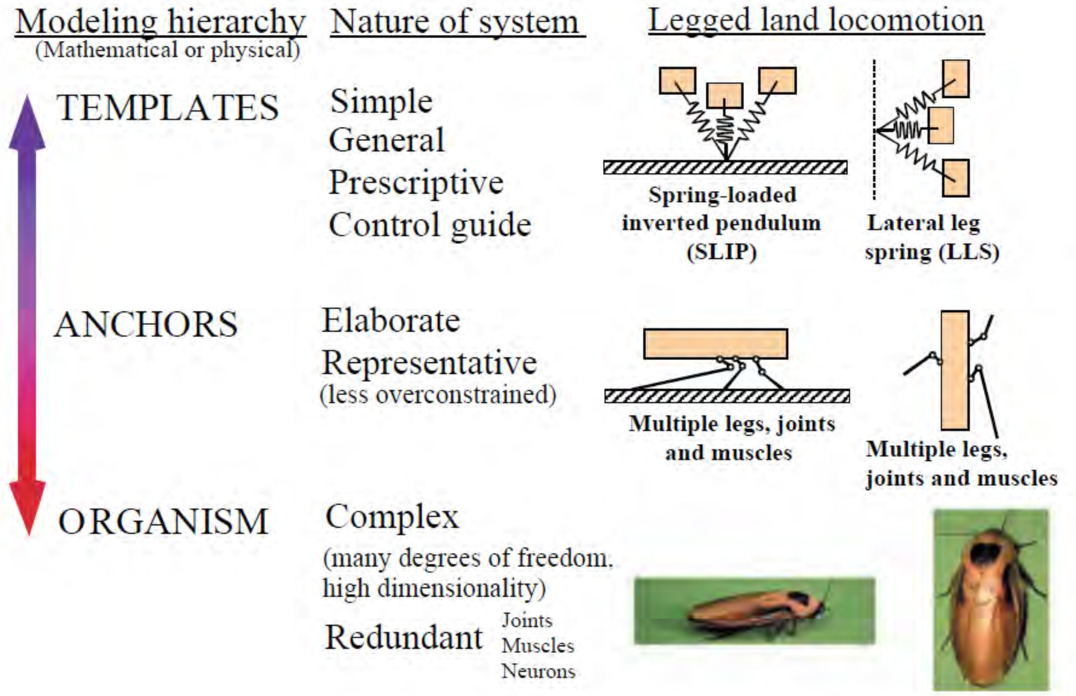

Figure 1.9: The idea Templates and Anchors for locomotion is depicted above. Templates are the models which describe the target (goal) behaviour of the system whereas anchors are closer to the morphology of the organism. Image from [54].

Although the templates offer a simpler representation of the animal, these dynamics can still consist of multibody systems. To mathematically model the multi-body system (Body-and-Tail) in the various manoeuvres, the Euler-Lagrange dynamics method [56] [57] can be employed. This is done by first writing the position and velocities of the tail in terms of the generalised coordinates. Then using these, the kinetic and potential energy for the i-th body can be expressed as:

$$T_i = \frac{1}{2} m_i (\boldsymbol{v}_i)^T \boldsymbol{v}_i + \frac{1}{2} (\boldsymbol{\omega}_i)^T \boldsymbol{I}_i \boldsymbol{\omega}_i \tag{1.1}$$

$$V_i = m_i (\boldsymbol{g})^T \boldsymbol{r}_i \tag{1.2}$$

where: $m_i$ is the mass of the body, $\boldsymbol{v}_i$ is the velocity of the centre mass with respect to the origin expressed in the inertial frame, $\boldsymbol{\omega}_i$ is the angular velocity vector of the centre of mass with respect to the origin, expressed in the body frame, $\boldsymbol{I}_i$ is the inertia tensor expressed in the body frame, $\boldsymbol{g}$ is the gravity vector expressed in the inertial frame and $\boldsymbol{r_i}$ is the position vector of the centre mass expressed in the inertial frame. These, along with the external forcing terms, can be utilized according to the method in [58] to derive the dynamic equations in the familiar form:

$$\boldsymbol{M\ddot{q}} + \boldsymbol{C\dot{q}} + \boldsymbol{G} = \boldsymbol{B\tau} + \boldsymbol{Q} + \boldsymbol{A^T\lambda} \tag{1.3}$$

where, $\boldsymbol{q}$ is the generalised coordinate vector, $\boldsymbol{M}$ is the Mass Matrix, $\boldsymbol{C}$ is the Centrifugal and Coriolis Matrix, $\boldsymbol{G}$ is the gravitational matrix, $\boldsymbol{B}$ is the input mapping matrix, $\boldsymbol{\tau}$ is the generalised input force vector, $\boldsymbol{Q}$ is the generalized force vector, $\boldsymbol{A}$ is the constraint Jacobian and $\boldsymbol{\lambda}$ is the constraint force vector. To obtain the constraint force, the following equation from [57] can be used:

$$\boldsymbol{\lambda} = -\left(\boldsymbol{AM^{-1}A^T}\right)^{-1}\left(\boldsymbol{AM^{-1}}(\boldsymbol{B\tau} - \boldsymbol{C\dot{q}} - \boldsymbol{G}) + \boldsymbol{\dot{A}\dot{q}}\right) \tag{1.4}$$

The generalized force vector $\boldsymbol{Q}$ encapsulates all the non-conservative forces which cannot be directly controlled. Examples of these are disturbances, aerodynamic drag or friction. To determine the generalized force $Q_j$ on the j-th generalized coordinate, the following equation can be used [56]:

$$Q_j = \sum_i^n \boldsymbol{f_i} \cdot \frac{\partial \boldsymbol{r_i}}{\partial q_j} \tag{1.5}$$

where, $\boldsymbol{f_i}$ is the force acting on the system at position $\boldsymbol{r_i}$. This is performed for each generalized coordinate.

These dynamics were then simulated in Matlab and Simulink and relevant analyses and feedback controller designs were performed. The templates, although simple will mostly be underactuated [59]. Thus, the method of partial feedback linearization (PFL) [60] (otherwise known as Input-Output Linearization [61]) will be employed to design the template's feedback controllers.

Furthermore, in Chapter 5, the method of trajectory optimization by use of Nonlinear Programming (NLP) techniques as described in Betts [62] and Srinivasan [63] will be utilized. The essential idea is to discretize the input trajectory as a piecewise linear function as illustrated in Figure 1.10. Then, the optimizer uses gradient methods to choose the control points for the torque profile by simulating the model repeatedly and evaluating the associated cost[2] [63]. This method can also factor in constraints in various forms

---

[2] Also, known as *Single Shooting* [63].

(nonlinear and linear) and has been successfully implemented in biomechanics [64] as well robotics applications [65] [66].

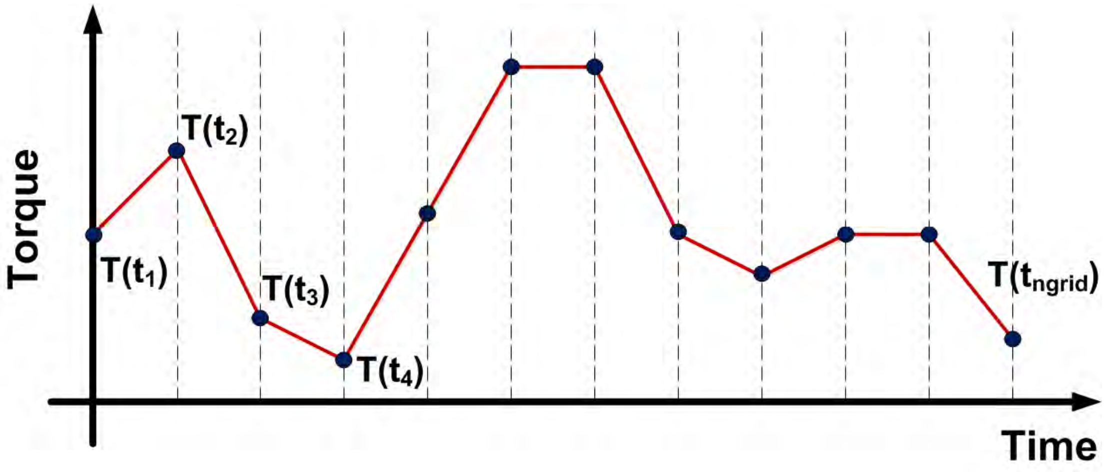

Figure 1.10: The problem of trajectory optimization is converted to a NLP, by discretizing the input (torque) trajectory. The control points ( $T(t_n)$ ) are then selected by the optimization algorithm. In this diagram the torque is defined by $n_{grid}$ number of variables to optimize.

To validate the simulated models, a physical robot (anchor) was built. This robot encapsulates the task level behaviour of manoeuvrability in the cheetah. This allows the results to be applicable to a broader range of application anchors. In essence, the aim is that the results will give insight to more complex anchors, despite the fact that a reduced order test platform was utilized. The platform was required to contain an actuated electro-mechanical tail, which was actuated as part of a feedback loop to test the hypotheses.

It was decided to employ a Traxxas Stampede high speed R/C truck as the base platform. This truck has been selected due to its high-speed (+50 km/h) and acceleration capability. Also, due to its high centre of gravity the R/C truck is prone to flipping over and roll-outs during aggressive manoeuvres, which is desirable for testing.

One may argue the relevance of testing the hypotheses on a wheeled platform but considering the discussion previously, template models essentially provide a “task encoder” [16]. For example, one can substitute the forces generated by a leg propelling the collected rigid body forwards for a wheel in contact with the ground. This is essentially the mechanism of moving from a template to an anchor. The task-level behaviour is thus fundamentally the same: a force is acting on a rigid body (cheetah or robot) to move it.

However, it should be noted that the models (mathematical and physical) developed in this thesis contain the following assumptions:

- ***The tail is rigid and thus any compliance in the cheetah tail is ignored.***
    - This is a plausible assumption, as during video observations at Cheetah Outreach and wildlife documentaries, the cheetah tail remains fairly straight while being actuated during a manoeuvre.
- ***The body geometry is rigid and fixed during the manoeuvre***
    - Clearly a cheetah is capable of flexing its spine which will shift the collective centre of mass (COM) around. However, the assumptions are considered to result in a conservative model which will still provide an understanding of the limitations in manoeuvrability and the positive effects a tail can provide.
- ***The body is always in contact with the substrate (the ground) during the manoeuvre***
    - Thus the templates will only be valid when the legs are in contact with the ground. This assumption holds during acceleration and rapid braking, but cheetahs gallop with low duty factors [67] and thus the assumption does not hold during the airborne phase of the gallop. However, considering that the tail becomes more effective while the body is airborne, as the moment of inertia decreases [43] [44], the models are deemed to be conservative. This concept is illustrated in Figure 1.11 and nevertheless the models will still provide valuable insight to the tail motions. This is a notable difference between the physical R/C truck model and the cheetah, as the templates can only be anchored during the stance phase; where at least one leg is on the ground.

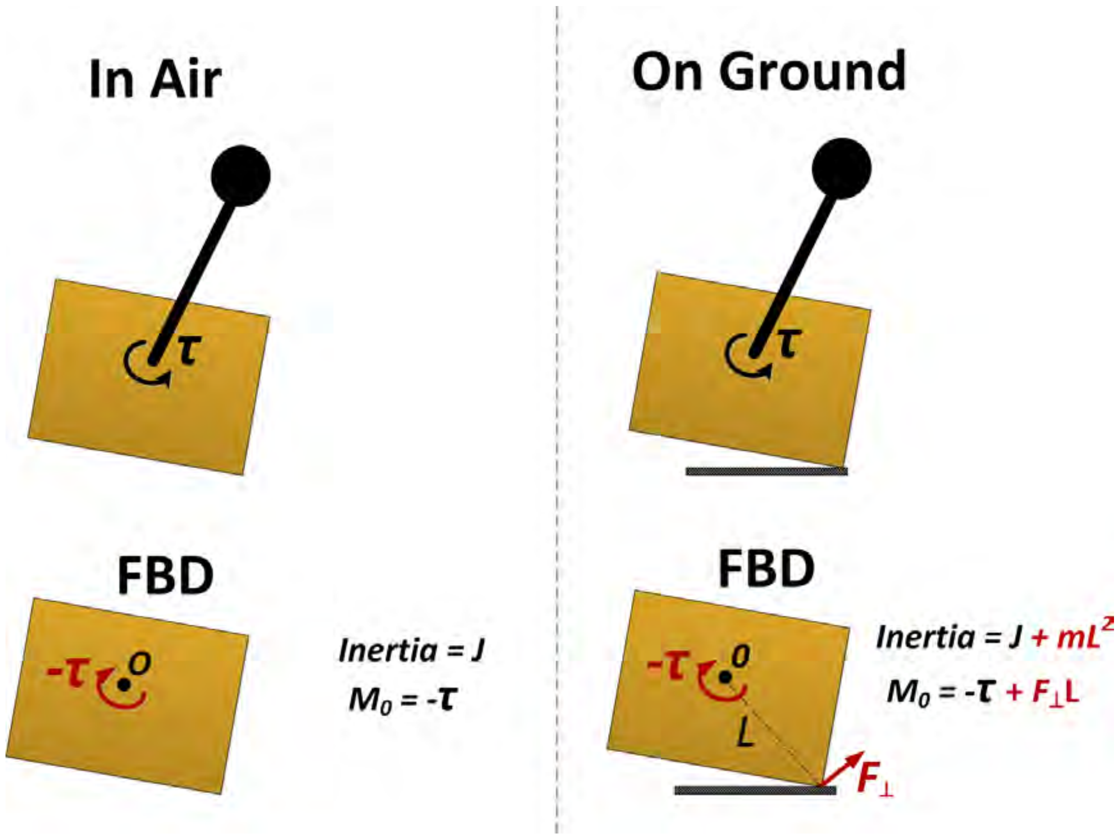

Figure 1.11: Tail effect in air and during stance. It is clear that during the aerial phase, the tail torque is the only moment on the body. However, during stance one can see that the there is an additional torque from the reaction force with the ground. The effective inertia of the body also increases during stance.

Lastly, to understand the dynamics of the cheetah tail, a measurement of its inertia and aerodynamics was made. With this, the aerodynamics of the cheetah tail fur was then investigated as well as a detailed measurement of the tail inertia. During the initial research presented in this dissertation, the Author was not aware of such measurements in the public literature. The thesis by Hudson [16], which measured the tail inertia, only became available to the Author at the end of this dissertation. The inertia measurements in this study occurred during a routine necropsy of a cheetah cadaver at the National Zoological Gardens in Pretoria, South Africa. This was done as an independent validation of the measurement by Hudson [16] via a different method.

## 1.5 Contributions and Outline

The primary goal of this thesis is to understand the motions of the cheetah tail in the context of manoeuvrability. Particularly, three specific motions were investigated: roll, pitch and cone tail motion. These were performed following an integrative approach by exploiting a combination of mathematical modelling, feedback control and physical modelling using robots. The novel contributions are as follows:

1. **An investigation of the motion of the cheetah tail in the roll axis for stability while turning at high speed**. Mathematical models for initiating a turn at high speed, feedback controllers and a novel bio-inspired robot platform were developed. This work has been published in [14].
2. **An investigation of the motion of the cheetah tail in the pitch axis for stability while rapid accelerating and braking.** Mathematical models for acceleration manoeuvres, feedback controllers and a novel robot platform were developed. This work has been published in [15].
3. **An investigation of the motion of the cheetah tail in a cone.** Mathematical model of a two degree of freedom (DOF) tail, trajectory optimization, feedback controllers and a novel two DOF tailed robot platform were developed. This work is being prepared for publication in a journal.
4. **An investigation of the aerodynamic properties of the cheetah tail.** The drag coefficient of the tail fur was determined and corresponding mathematical models were developed to determine its effects. This work has been submitted and is under review [68].

This dissertation progresses as shown in in Figure 1.12. **Chapter 1** provides the context and contextualisation of the entire work.

In **Chapter 2**, motions of the tail in the roll axis during turn initiation at high-speeds are investigated. The mathematical model for a high-speed turn is derived and the model with a tail is shown to be more successful at rapid turns in simulation. A high speed mobile platform with an actuated tail was then built to experimentally validate the control algorithms. Further controller development is performed based on results of the initial simulations. Finally, it is shown that by rapidly swinging the tail, the system is capable of turning at much higher speeds than a tail-less version.

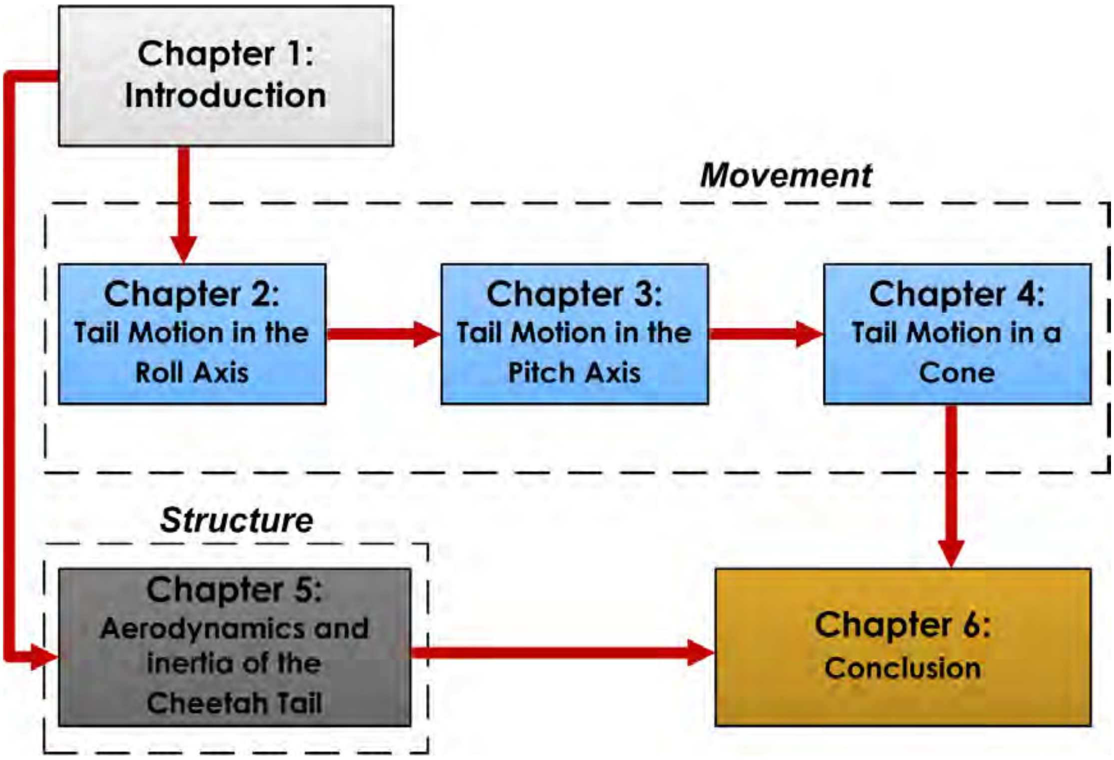

Figure 1.12: Thesis progression and outline is shown. Chapters 2, 3 and 4 concentrate on understanding the specific tail motions, whereas Chapter 5 is concerned with understanding the structure and biological principles of the cheetah tail itself.

In **Chapter 3**, motions of the tail in the pitch axis during rapid acceleration and braking manoeuvres are investigated. To understand the targeted behaviour of a cheetah performing a longitudinal manoeuvre and the effects an actuated tail has, a simple mathematical template was developed. Subsequently, feedback controllers are designed based on the hypothesis. Finally, the control system was experimentally tested on a reduced order robot model which increased its manoeuvrability considerably

In **Chapter 4**, motions of the tail by the combination of pitching and yawing in a cone shape are investigated. By using optimization methods, it is determined that the cone motion results in a continuous torque being imparted on the body, across multiple revolutions. A novel two degree of freedom robot tail actuator is then designed. Next, by use of the open loop torque trajectories produced by the optimization, a feedback controller for the robot system is designed. Finally, the robot platform is experimentally tested and it is determined that the two degree of freedom tail can impart a pure roll torque on the body during a high speed turn manoeuvre.

**Chapter 5** describes the biological measurements of the cheetah tail. As stated before, at the end of the research period, the Author was given the opportunity to measure the inertia of a cheetah tail. The inertia measurement is described and it was discovered that the tail is not as heavy (relative to the body mass) as commonly believed. The tail fur was then used to create an anatomical tail model and placed in a wind tunnel to determine its aerodynamic drag. Here, it was found to impart more drag force than a smooth cylinder of the same diameter. In fact the fur imparted a drag force of a much wider cylinder. Finally, the dynamic modelling of a rigid tail reveals that aerodynamic forces can provide significant angular impulse on the cheetah body during manoeuvres as well as loading of the hind legs.

**Chapter 6** completes the thesis by uniting all the information produced by the foregoing chapters. In this chapter avenues for future directions of research are discussed in detail.

# Chapter 2

## Tail Motion in the Roll Axis

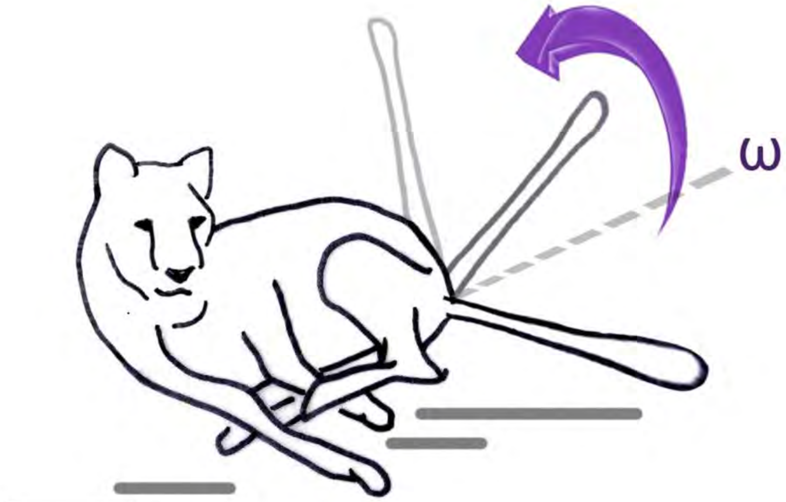

Briggs et al. [46] hypothesised that the cheetah tail was providing a reaction moment to help roll the body in mid-air and initiate the turn. In this thesis, the hypothesis is that by rolling the tail during the contact phase such as turn initiation, the cheetah tail can also counteract the torque produced from the centrifugal force. This torque would otherwise cause the body to topple over as discussed by Biewener [69].

In what follows, the mathematical model for the rapid turning manoeuvre is first derived. Here simple reduced-order models with and without a tail are compared. It is then shown that by actuating the tail with a simple controller, one can increase the capture region for stability, thus implying more aggressive manoeuvres are possible. Following this, a robot test platform, *Dima I*, is designed to validate experimentally the tail controller system. The mechanical design of the tail actuator is also presented. Subsequently, the tail controllers are designed for the robot platform and simulated. The experimental results comparing a robot with and without a tail are then produced. Finally, the chapter is concluded with a discussion of the results.

The reader should note that significant portions of this chapter also appear in [14].

## 2.1 Turning at High Speed

This chapter was inspired by various videos showing the cheetah during high-speed pursuit of prey. Here, the cheetah is often seen swinging the tail in the roll axis while performing a turn at high speed. An example of this motion is depicted in Figure 2.1.

Figure 2.1: Cheetah performing a turn at high-speed. The motion in the roll axis is evident. Image from [70].

### 2.1.1 *Equations of Motion*

To examine the benefits that an actuated tail can provide an animal (or robot) performing a high speed turn, the underlying mechanics need to be understood first. Accordingly, an adequate mathematical model is needed for this scenario which can be validated via simulation.

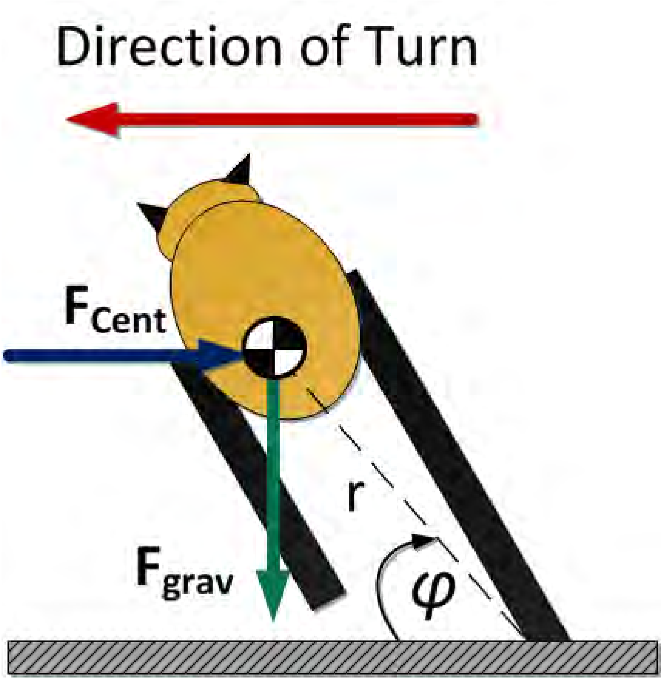

Figure 2.2: An animal (viewed from behind) initiating a turn at some velocity. If the centrifugal force ($F_{cent}$) is large enough, the body will indeed topple over. This model assumes sufficient friction. This model is based on the discussion in Section 3.5 of [69].

Consider a cheetah (viewed from behind) travelling at some forward velocity when it suddenly initiates a turn to the left. This scenario is depicted above in Figure 2.2. If the centrifugal force is large enough the body (animal or robot) will topple. The centrifugal force equation is given by the equation:

$$F_{cent} = m_b \frac{v^2}{R}, \tag{2.1}$$

with $m_b$ being the mass of the body, $v$ the forward velocity of the body and $R$ the turning radius. It is evident that with increased speed the centrifugal force will increase quadratically. The hypothesis in this study is that the tail can provide a torque to counteract this toppling moment, thus enabling the cheetah to be more manoeuvrable.

To understand how the tail could benefit the animal, the following simplified model (template) is proposed: The system is modelled as a lumped rigid body (consisting of the body, legs and head) with one contact point on the outside of the turn. This situation will arise just before toppling [69]. The tail is modelled as a point mass attached to an idealized massless rod of length $L_t$ as in [43] [44]. Furthermore, the tail is actuated by an ideal torque actuator ($\tau$) which is located at the centre of mass of the body much like that described in [46]. If no slipping is assumed, this model is depicted graphically in Figure 2.3.

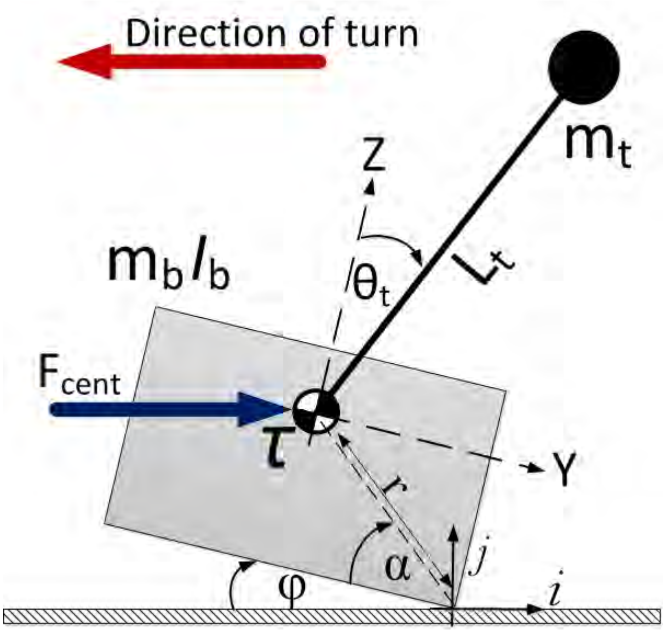

Figure 2.3: The mathematical model for a high speed turning manoeuvre is illustrated graphically (viewed from behind). The model consists of a 2D rigid body and a point mass tail with a single point of contact with the ground.

This system is then modelled using Euler-Lagrange mechanics [56] [57]. The generalized coordinate vector is:

$$\boldsymbol{q} = [\varphi \quad \theta_t]^T, \tag{2.2}$$

where, $\varphi$ is the roll angle of the body and $\theta_t$ is the relative angle between the tail and body. Additionally, $\alpha$ and $r$ are geometric properties of the lumped rigid body. The positions of the body and tail respectively are shown to be:

$$\boldsymbol{p_b} = \begin{bmatrix} -rcos(\alpha + \varphi) \\ rsin(\alpha + \varphi) \end{bmatrix} \tag{2.3}$$

$$\boldsymbol{p_t} = \boldsymbol{p_b} + \begin{bmatrix} L_t sin(\varphi + \theta_t) \\ L_t cos(\varphi + \theta_t) \end{bmatrix} \tag{2.4}$$

These can then be differentiated to obtain the velocities, which will be used to derive the kinetic energy.

The centrifugal force ($F_{cent}$) can be seen as a generalized force [56] and is derived to be:

$$Q_\varphi = F_{cent}(\, r \sin(\varphi + \alpha)\,), \tag{2.5}$$

which acts on the generalized coordinate $\varphi$ only. Using all the information provided, the dynamics can be derived using the methods described in Section 1.3.

Now that the system dynamics for the template have been defined, a tail feedback control system can effectively be designed to determine if the tail can indeed benefit this scenario.

### 2.1.2 *Tail Control System*

If the dynamics of the high speed turn are reflected on, one can consider the centrifugal force to be a disturbance. In fact, this disturbance (if sufficiently large) will directly cause a net rolling moment, which will subsequently result in a roll rate and ultimately the animal toppling over. Hence, the hypothesis is that the tail can counteract this effect. In a sense, the tail can be a mechanism for *disturbance rejection*.

It is decided to employ the tail as an actuator for a roll rate controller. This implies that the roll angle will not be regulated, which indicates that banked turns will be possible. This is different to the attitude controllers presented previously by [43] [44] [46]

Unfortunately, the template described in Section 2.1.1, is still an under-actuated system, which means Full State Feedback Linearization methods [59] cannot be applied. However, one can partially linearize one coordinate by using Partial Feedback Linearization (PFL) [60] on the body roll angle $\varphi$. The architecture for the control system is shown in Figure 2.4.

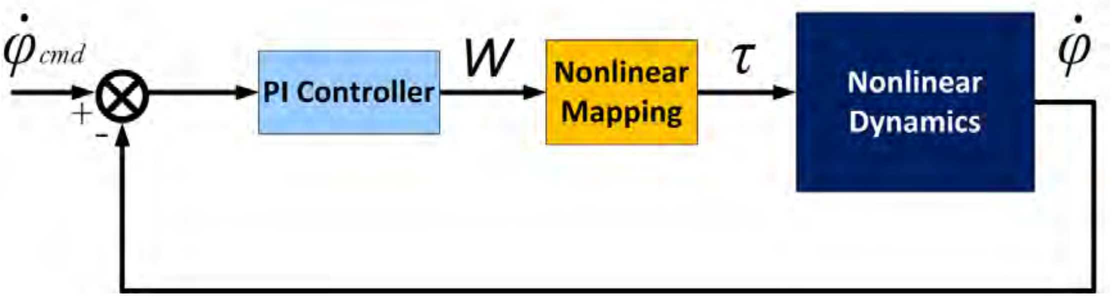

Figure 2.4: Roll Rate Controller architecture

Following the method described in [60], the roll angle can be linearized by setting its second derivative to some variable, $W$. This results in the relationship:

$$\dot{\varphi} = \frac{W}{s}, \tag{2.6}$$

which is now a linear system and '$s$' is the Laplace variable.

This variable $W$ is mapped to the tail actuator torque by the following equation:

$$\tau = L_t^2 m_t W - W(L_t^2 m_t + I_B) \tag{2.7}$$

The reader will note that the linearized dynamics are now simply that of an integrator with gain $W$. A PI controller can readily be designed and the two closed-loop poles can be placed anywhere desired. This is done by equating coefficients of the characteristic function of CL poles to the desired characteristic function as defined by the damping and bandwidth.

### 2.1.3 *Simulation*

The tail feedback control system was then tested in simulation and compared to that of the system without a tail. The systems were initialised at various positive roll rates. The motive for this is that the centrifugal force will indeed induce a body roll rate and this will provide a measurement of comparative stability. Four scenarios are simulated:

- Model without tail
- Model with tail fixed $\theta_t$ = -90°: Facing into the turn
- Model with tail and controller with initial $\theta_t$ = 0 : Straight up
- Model with tail and controller with initial $\theta_t$ = -90° : Facing into the turn

The simulation was terminated once the body came to rest, flipped over or the tail has reached the end of its swing – which has been specified to be ±90°.

The dynamic equations were modelled in Simulink using the model parameters given below in Table 1. Furthermore, the roll rate controller dynamics are set to 4.5 rad/s with a damping factor of 0.8 by pole placement.

Table 1: *Dima I* Roll Model Parameters

| **Parameter** | **Value** |
|---|---|
| Body Mass ( $\boldsymbol{m_b}$) | 5 (kg) |
| Body Roll Inertia ($\boldsymbol{I_B}$) | 0.093 (kgm$^2$) |
| Tail Mass ($\boldsymbol{m_t}$) | 0.4 (kg) |
| Tail Length ($\boldsymbol{L_t}$) | 0.5 (m) |
| Distance to centre of mass ($\boldsymbol{r}$) | 0.257 (m) |
| Angle to centre of mass ($\boldsymbol{\alpha}$) | 0.897 (rad) |

The models without the tail and with the tail held fixed were not able to recover from the initial roll rate disturbance. The phase portraits are shown in Figure 2.5 and it is clear that the aforementioned configurations have a limited basin of stability and do not return to zero for rates greater than 4.63 rad/s.

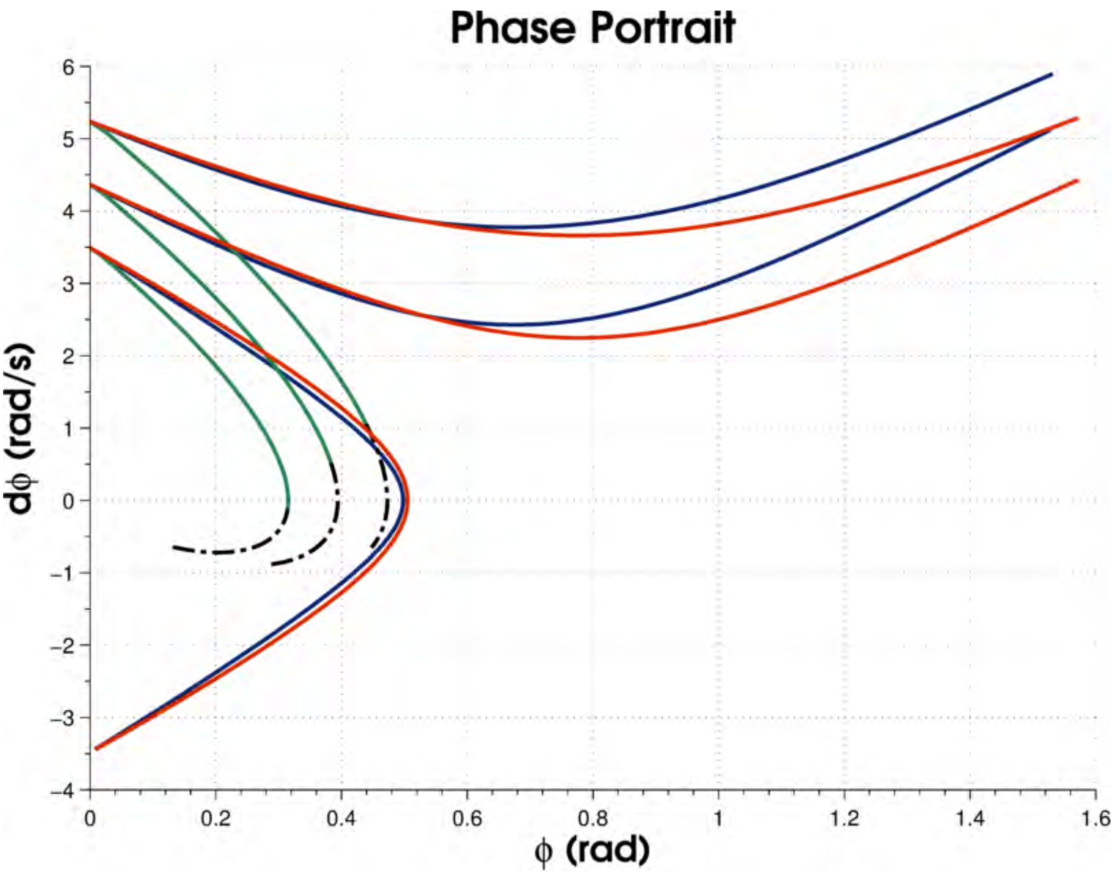

Figure 2.5: Phase portrait comparing the system without tail (blue plot), with tail fixed -90° initial angle (red plot), with tail plus controller at initial tail angle of zero (green plot) and with the tail plus the controller at -90° initial angle (dotted black)

With the tail at zero initial angle (and its respective controller engaged), the roll rate is driven towards zero. Though, it is observed that this configuration does not fully bring the body to rest.

With the tail at -90° initial value (facing into the turn), an improved disturbance rejection is shown. This is a very interesting result, as it is the same behaviour observed in the cheetah footage, i.e. the cheetah first puts its tail into the direction of the turn before swinging it over. However, the roll rate controller suffers from two issues:

- The controller is too slow to catch the disturbance in time. This implies that a feedforward torque is possibly required.
- At the end of the tail swing, the tail has a very high rotational velocity and as such would negate the effects of the roll stabilization when the tail reaches its limits.

These two issues will need to be resolved when the system is implemented on a physical system as discussed in the Section 2.3.

## 2.2 Robot Design

*Dima I* (seen in Figure 1.3) was designed as the test platform for the actuated tail control system. The main design ideals were that a high speed platform was desired. A platform with a high enough centre of gravity was also required, so that it would indeed topple when performing rapid turns at high speed. This would ensure the results are applicable to not only wheeled robots but also to legged animals such as the cheetah.

### *2.2.1 Tail Design*

Naturally, the tail design was of critical importance. The robot tail needed to match the performance (within reason) of the cheetah tail. Thus, a tail actuator with a high power as well as considerable length was required.

The motor selected to actuate the tail was the Maxon DCX-35L as it had a maximum continuous power rating of 120W and a relatively low mass. However, in order to select the optimal gear box ratio ($N$), the optimal tail mass was required as well, as detailed in [44]. The motor characteristics are provided in Table 2.

Table 2: Maxon DCX-35 characteristics

| **Parameter** | **Value** |
|---|---|
| Motor Nominal Voltage ($\boldsymbol{V}$) | 12 (V) |
| Motor torque constant ($\boldsymbol{K_{\varphi}}$) | 13.7 (mNm/A) |
| Motor Gear Ratio ( $\boldsymbol{N}$) | 26 |
| Motor terminal resistance ($\boldsymbol{R_T}$) | 0.0792 (Ω) |
| No load speed ($\boldsymbol{\omega_0}$) | 8140 (rpm) |

Numerical simulations were then performed similar to those described in [43] [46]. Essentially, the model described in Section 2.2.1, was used as a baseline with the tail in the

90° position and the body at 0°. The torque input (T) to the tail was adapted from [46] to include the gear ratio (N) and is expressed as:

$$T = T_0 N\eta\left(1 - \frac{T_0 N\eta\omega}{4P^*}\right), \tag{2.8}$$

Where, $T_0$ is the motor's stall torque, $\eta$ is the gearbox efficiency, $\omega$ is the shaft speed, and $P^*$ is the maximum motor power. All these parameters were obtained from the manufacturer of the Maxon motor.

The simulation, with the torque model described, was run several times varying tail mass and gear ratio. The maximum body angular deflection was then captured and utilized as a performance metric[3]. A tail length of 0.5 m (1 body length) and body mass of 5 kg were used in all simulation runs. The resulting plot is shown below in Figure 2.6.

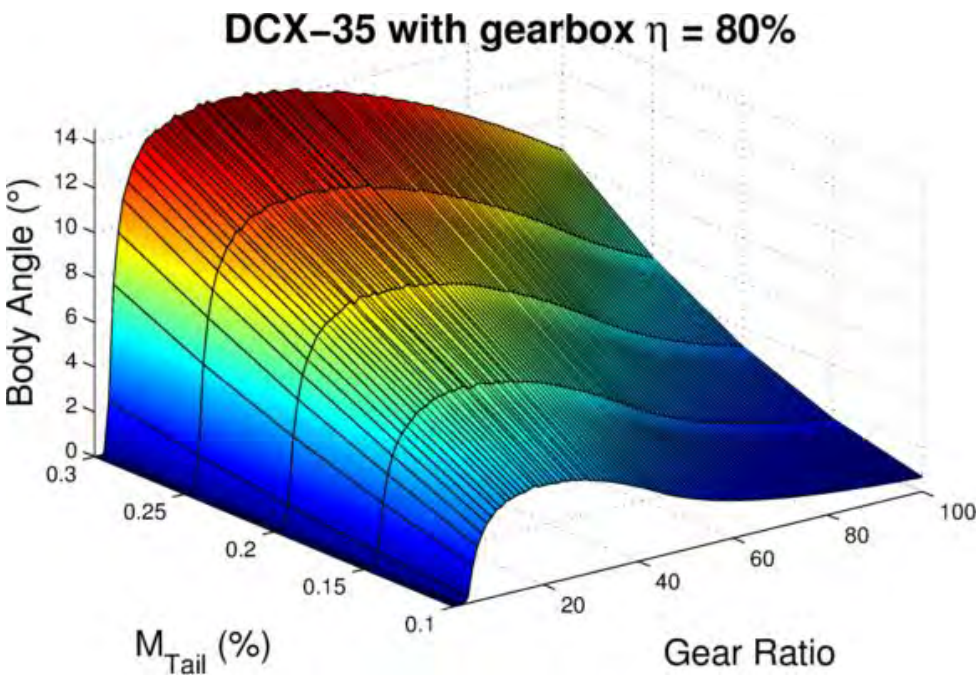

Figure 2.6: The Maxon gearbox and tail mass selection plot is seen above. The body angle deflection was chosen as the performance metric which needed to be maximised. It is clear that the tail becomes more effective as its mass increases.

The results are intuitive as one would expect that as the mass increases, the tail becomes more effective. However, a heavy tail would shift the centre of mass of the vehicle considerably. Thus, it was decided to select a mass of 0.08% of the body (400g). Using this

---

[3] In a sense, this is an indirect measurement of the angular impulse on the body.

value, the corresponding gear ratio of 28 would be the optimal choice. Thus, the closest Maxon gear box ratio of 26 was selected.

### 2.2.2 *Mechanical Design*

The Traxxas Stampede R/C car was selected as the base for the mechanical design. This car was chosen as it had a sufficiently high speed (+50 km/h) and also a high centre of gravity aligning with the model described Section 2.1.1.

Figure 2.7: Solidworks model of *Dima I.*

The car was modelled in Solidworks as depicted in Figure 2.7 and was adapted with major modifications by the addition of the following:

- Two aluminium platforms for mounting of the on-board electronics
- Stiffer springs to accommodate the increased weight
- A roll cage to protect the electronics from impacts at high speed

The tail rod was selected to be an aluminium rod of 10mm (mass of 99g) and the tail mass was chosen to be brass for its high density. This configuration would align closely with the massless rod assumption in in Section 2.1.1. This was then connected to a coupler which was attached to the motor shaft and supported by a bearing as seen in Figure 2.8.

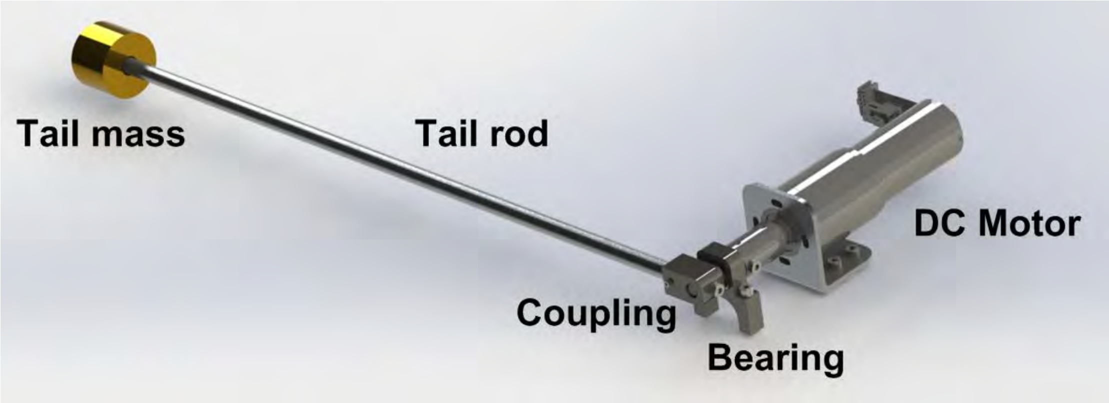

Figure 2.8: *Dima I* tail mechanism. The DC motor was coupled to the tail, via a coupling which allowed motion in the roll axis of the robot.

### 2.2.3 *Hardware and Software Design*

The on-board processor was the STM32F4 Discovery with an ARM Cortex M4 running at 168 MHz. Logging was implemented on a micro-SD card. For telemetry an XBee Pro was selected and was used for communication between a host PC and the robot.

To drive the tail motor a Pololu 18V15 PWM motor controller was employed. In order to sense all the states (velocity, angular rates) as well as receive estimated attitude angles, the Tellumat SP1000GA was selected. Via its Extended Kalman Filter, the sensor provided state information updates at 50 Hz.

The software consisted of a FreeRTOS kernel [71], which allowed multi-tasking capability with the added benefit of real time operation. Lastly, Second Order Butterworth filters were implemented on the raw data provided by the IMU.

## 2.3 Feedback Control Design

The task was then to design the tail controller algorithms for the *Dima I* robot platform to be tested experimentally. With insights gained in Section 2.1.3, a revised controller architecture was proposed and is illustrated in Figure 2.9

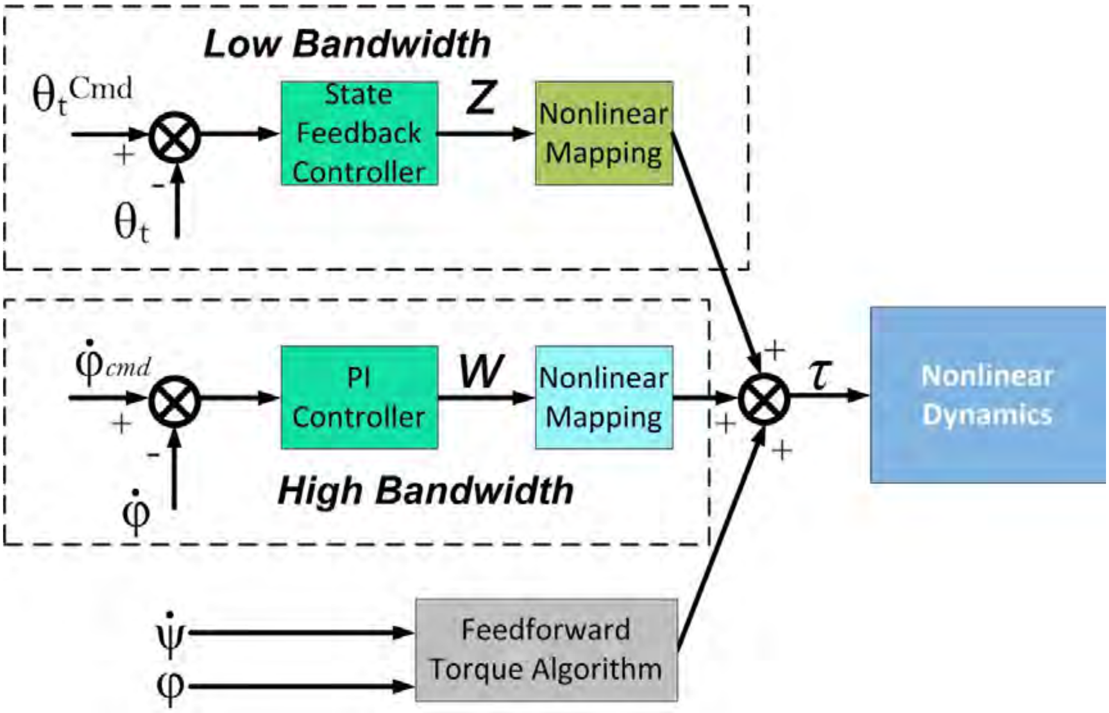

Figure 2.9: Revised tail controller architecture.

The first addition to the architecture is a low bandwidth tail position controller which will serve a dual purpose. Firstly, it will slow down the tail appropriately once the turn is complete and the roll rate has been damped. Secondly, this controller will allow the tail to be placed in the correct initial position before a turn.

The Feedforward Torque Algorithm (FTA) will allow the tail system to automatically swing the tail by the net torque induced by the turn. This will allow the tail to damp out the disturbance of the turn, leaving the roll rate controller to diminish any residual errors due to modelling inaccuracy.

### 2.3.1 *Dima I Robot Model*

To design the controllers effectively, the model described in Section 2.1.1 was employed and modified it for this particular robot. The parameters for *Dima I* are shown in Table 1 for the high speed turning model. Now, if one re-examines equation (2.1), it can be seen that the centrifugal force is dependent on the turning radius (R). The robot's steering mechanism is a True Ackermann Mechanism [72], thus the turning radius is given by:

$$R = \frac{L}{\tan(\delta)}, \tag{2.9}$$

where δ is the steering angle and $L$ is the length between the front and rear axles. For this specific robot $L$ is 0.28 m.

Furthermore, the steering angle is not produced instantly and also has dynamics (due to the servo motor). Thus, these dynamics need to be factored in and induce a lag in the centrifugal force. For simplicity, this can be modelled as a first order dynamic system. After simple steering step tests on the car, the time constant was determined to be 0.8 s for the steering transfer function.

With the exception of the servo model, the mathematical model employed will be the same as that of Section 2.1.1. The reader should note that the model ignores the effect of the springs on the car and this could affect the experimental data. However, considering that the focus of the research is on the tail algorithms, this was deemed a feasible assumption.

### 2.3.2 Tail Position Controller

As discussed previously the tail position controller, will slow down the tail at the end of its swing and also allow command of the tail to the correct initial value.

Once more, PFL is utilized to linearize one coordinate. In this case, the tail angle acceleration is set to some variable $z$, which is then a linear system. The mapping from $z$ to actual torque is provided by employing the method described in [60]:

$$\tau_{pos} = m_t z L_t^2 - g m_t L_t \sin\theta_t \tag{2.10}$$

Now that the dynamics are linearized, a full state feedback controller (with an additional integrator state) is designed to place the poles much slower than that of the rate controller. As such, the fasted pole is placed at 1 rad/s.

### 2.3.3 Feedforward Torque Controller (FTA)

The FTA will allow the tail to dampen out the disturbance much faster. This is achieved by first calculating the torque produced by the centrifugal force and then determining if this is greater than that of the gravitational torque. If this condition is true, it will directly command this ‘delta torque’ to the tail motor.

After some algebraic manipulation, the centrifugal force can be written as:

$$F_c = m_b v\dot{\psi} \tag{2.11}$$

Note, $\dot{\psi}$ is the yaw rate and $v$ is the forward velocity. The corresponding torque can be calculated as:

$$\tau_{cent} = F_{cent} r \sin(\alpha + \varphi). \tag{2.12}$$

Now, if this magnitude is greater than the torque induced by the gravity vector passing through the body's centre of mass, the difference is directly commanded to the tail.

### 2.3.4 Simulation

The model and aforementioned controllers were then numerically simulated in Simulink. The system is given an initial steering angle of zero, and then stepped to 30°. After 0.5 s, to keep the tail angle within its range, the steering is again stepped back to zero, thereby ending the turn. This is done at varying initial forward velocity values.

The maximum initial velocity possible with the tail controller algorithms before toppling occurred was 4.5 m/s. The results are shown in Figure 2.10. It is clear that the body angle is brought back to zero and furthermore that the tail velocity is sufficiently diminished. The effect of the tail position controller can be seen after 0.5s. The turn initiated at this velocity resulted in 16.8 m/s2 radial (lateral) acceleration being experienced.

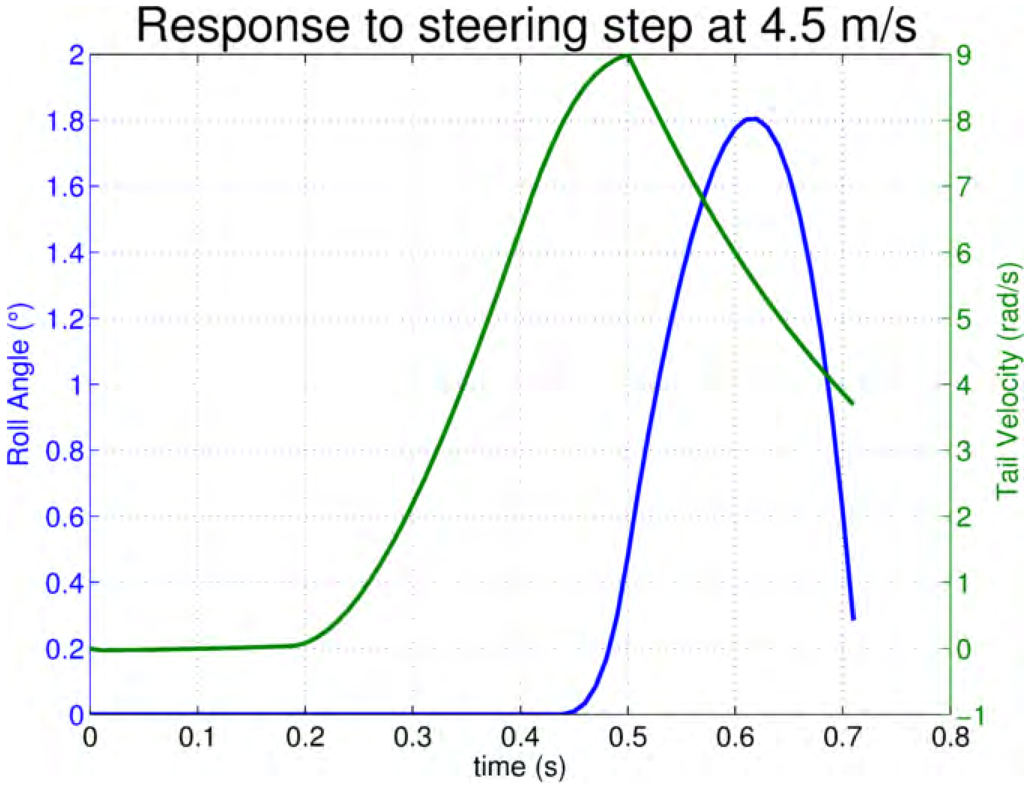

Figure 2.10: Body angle and tail velocity responses to a 30° steering step (length 0.5 s) initiated at 4.5m/s.

A model without a tail was also subjected to the centrifugal force and the maximum velocity a successful turn occurred at was 2m/s.

## 2.4 Experiments

The effectiveness of the tail controller algorithms was then evaluated on *Dima I*. The test results would indeed validate the motive for employing an actuated tail on a high speed robot and provide insight as to the effect of the cheetah's tail on its manoeuvrability. The controller algorithms were coded to the embedded processor and the output torque commanded by them was converted to a voltage command by the following equation:

$$V_{cmd} = K_{\varphi} N \omega + \frac{R_T}{K_{\varphi} N} \tau_{cmd}, \tag{2.13}$$

where, $K_{\varphi}$ is the torque constant of the motor, $V_{cmd}$ is the commanded voltage, $N$ is the motor gear ratio, $R_T$ is the motor terminal resistance and $\omega$ is the motor shaft speed. These parameters are provided in Table 2.

The test procedure for the experiments was as follows:

- The robot would drive straight until attaining steady state velocity
- The steering controller would engage a 30° steering angle for 0.5 s in the right direction
- After 0.5 s, the steering would return to zero

The performance metric was the lateral acceleration rotated into the inertial frame which was derived from the IMU.

### 2.4.1 *Results*

The tail-less robot attained a greater velocity (approximately 3.1 m/s) before toppling over during the turning step than the model in Section 2.3.4 predicted. The maximum lateral acceleration obtained was on average 8.3 m/s$^2$ and is depicted in Fig. 10. The robot with the tail also performed better than the model predicted, and was capable of turning at 7.5 m/s and achieved on average 11.8 m/s$^2$ lateral acceleration. The reader is encouraged to view the attached videos (See Supplementary Material on DVD).

Figure 2.11: *Dima I* performing a turn at 7 m/s. Note the use of the tail.

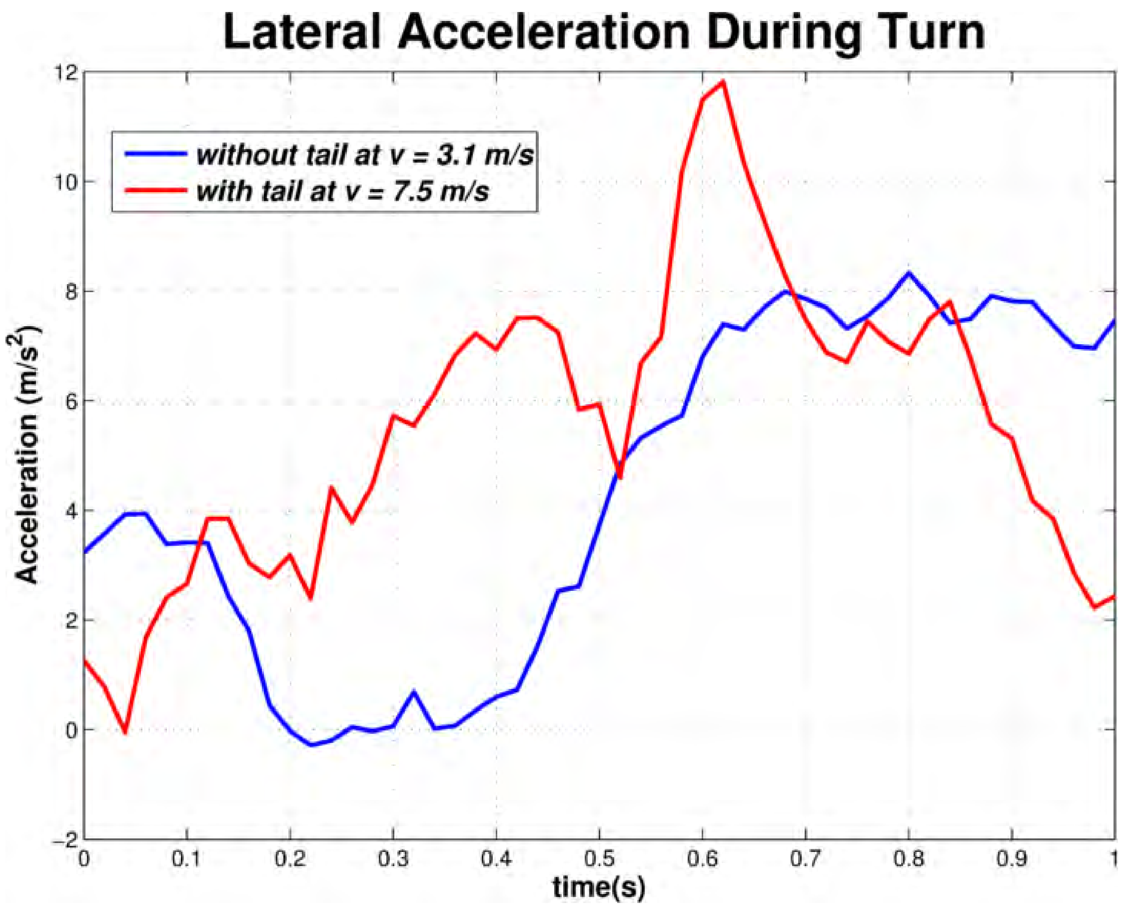

Figure 2.12: Lateral acceleration logged by the robot. With the tail controller, the robot was able to turn at a velocity of 7.5 m/s and achieve a maximum acceleration of on average of 11.8 m/$s^2$.

## 2.5 Discussion

The system surpassed predicted velocity performance for both tailed and tail-less models. This can be attributed to the robot's springs which were not modelled. These allow the robot to perform a banked turn, which increases stability.

The lateral acceleration achieved with the tail was approximately 30% less than predicted and can be attributed to the tail not being fully aligned with the COM which would reduce the turning yaw rate. As seen in Figure 2.13, the reaction force causes a torque on the body due to the moment arm (c) from the tail point of attachment to the COM. From the CAD model this distance was 166 mm. Nevertheless, the addition of the tail enabled the robot to still achieve an approximate 40% increase in lateral acceleration compared to the tail-less version.

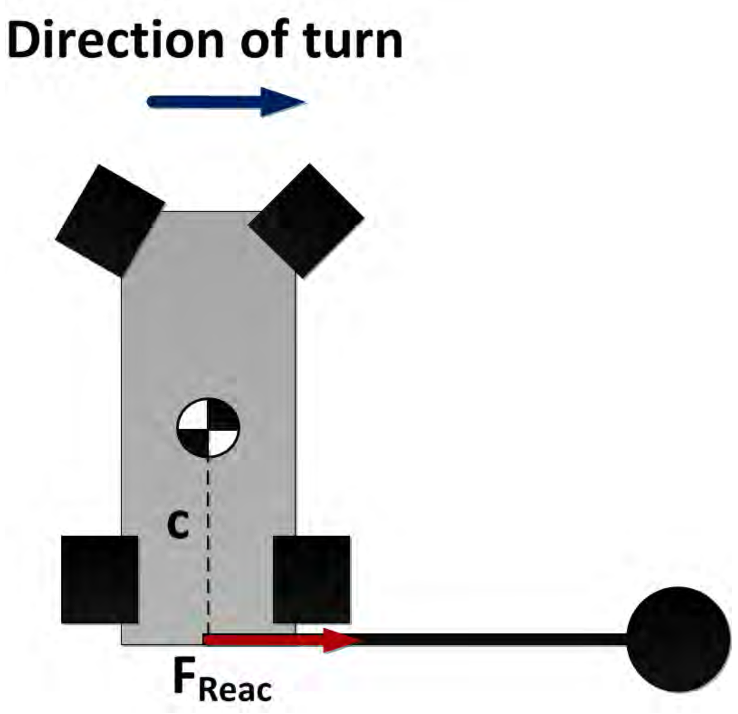

Figure 2.13: Top view of the robot. The reaction force of the tail on the body will cause a yawing torque due to moment arm (C) from the COM.

These experiments and simulations have shown that is indeed possible for the cheetah to initiate turns at high velocities and use the tail to stabilize its body roll. This would ensure that it could adequately react to its prey during evasive manoeuvres. Furthermore, the results also illustrate that an actuated tail could benefit a high-speed wheeled robot to perform turns at high speed.

It should be noted that longer duration turns were attempted, but this often resulted in the tail striking the end stops or the ground, which caused the robot to flip over. This illuminates two issues: Firstly, this confirms the view in the literature that tails are more suited to short time manoeuvres [43] [46]. Secondly, for the tail to be applied optimally, some constraints handling mechanism will need to be implemented. The reader will recall that the turning manoeuvre here was performed in open-loop. It is natural to reason that the cheetah could be implementing some optimal trajectory planner to ensure that manoeuvres will not result in the tail angle becoming saturated. Alternatively, the cheetah could be performing another motion for the tail which would allow longer duration turns. The latter thought is the subject matter for further exploration in Chapter 4 of this thesis.

# Chapter 3

## Tail Motion in the Pitch Axis

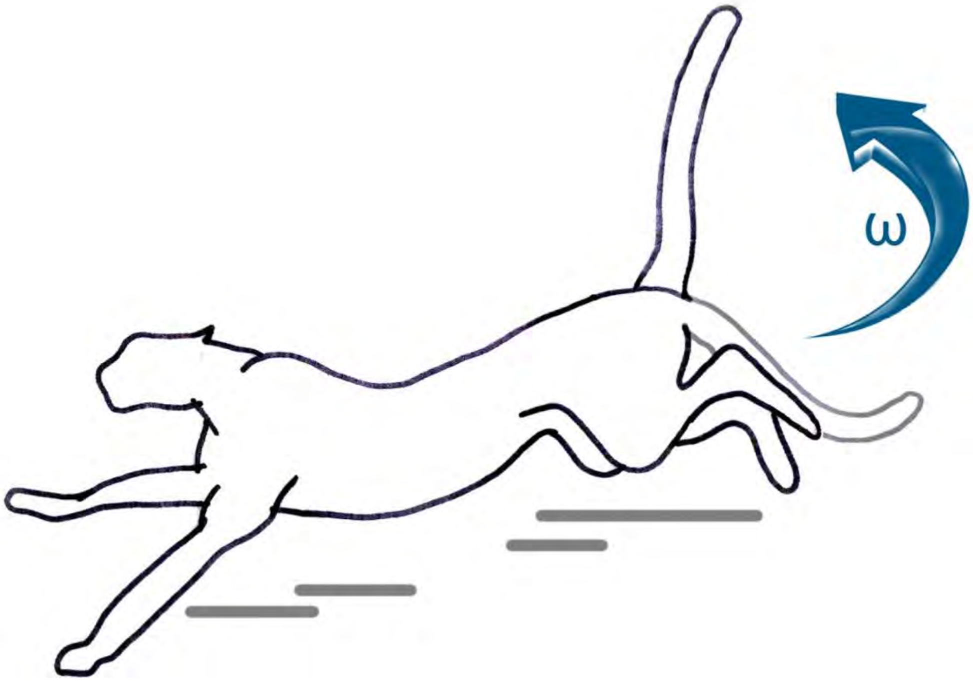

In a recent publication in Nature, Wilson et al [2] have shown that the true success in cheetah hunts, is due to the animal's ability to manoeuvre and particularly to accelerate rapidly. However, as mentioned previously quadrupeds are limited in this regard by the Pitch then Power Model [21]. The hypothesis here is that the cheetah is capable of stabilizing these manoeuvres by actuating its tail in the pitch axis.

In what follows, employing the paradigm of biomechanical templates [54], a reduced-order dynamic model is developed to describe the targeted behaviour of an animal (a cheetah in this case) performing an acceleration (or braking) manoeuvre. Here, simple models with and without a tail are compared and it is shown that with a tail actuator, more aggressive acceleration manoeuvres are possible. In subsequent sections, the model that was developed was refined for the specific robotic test platform. This chapter also includes the design of novel tail controller algorithms as well as simulation of rapid acceleration and braking manoeuvres. In Section 3.5, the experimental results are provided for the robotic platform. Finally, Section 3.6 discusses the experimental results from which conclusions are drawn.

The reader should note that significant portions of this chapter also appear in [15].

## 3.1 The Longitudinal Manoeuvre Template

The hypothesis is motivated by various wildlife videos of the cheetah in pursuit of prey where it can be seen actuating its tail while manoeuvring. Additionally, this particular study is enthused by video observations (see Figure 3.1) of cheetahs at *Cheetah Outreach*.

As in Chapter 2, the paradigm of Templates and Anchors [54] will be followed. As described previously, animals elegantly employ a synergy of muscles to perform high-level (task) behaviour. In this thesis an understanding of this task-level behaviour is sought. Thus, though they are simplistic models, templates offer a powerful mechanism to provide insight into neuromechanical control.

Figure 3.1: A cheetah is shown rapidly braking while chasing a lure during a weekly exercise run. Note the motion of the tail in the sagittal plane. The frame rate in these is 120 fps and every 4th frame is shown. (Filmed by the Author while visiting Cheetah Outreach in Cape Town, South Africa).

### 3.1.1 *Equations of Motion*

Inspired by the Pitch then Power Model [21], a template is proposed to capture the task-level behaviour of a cheetah during a rapid acceleration[4] manoeuvre. This model although conservative and simple, provides valuable insight into the limitations of manoeuvrability as well as the dynamic effect a tail would have in these scenarios.

It is stated that during a rapid acceleration or braking manoeuvre, the hind and forelegs respectively are the primary forces acting on the body [21] [23]. Where, by contact with the substrate and by use of hip torque, (or shoulder torque in the case for braking) the animal is propelled. If one further considers the abdomen, legs and head as one collective rigid body the complexity of the mathematical model can be reduced significantly.

With the addition of an actuated tail, the proposed *Longitudinal Manoeuvre Template (LMT)* is depicted in Figure 3.2.

---

[4] The template for the acceleration and braking manoeuvres are essentially the same except that the external force is applied at different points on the body.

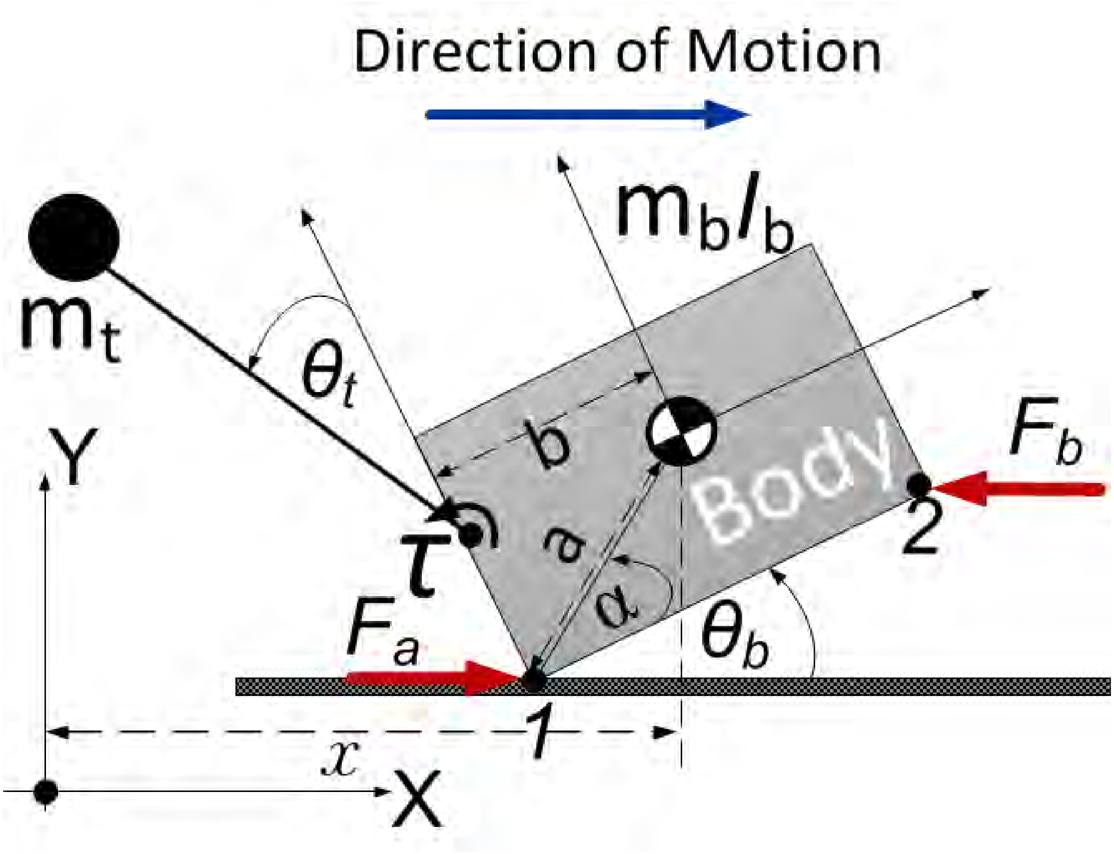

Figure 3.2: The Longitudinal Manoeuvre Template (LMT) model is depicted. The model consists of a collective rigid body and a point mass tail. The model experiences either force $F_a$when undergoing an accelerating manoeuvre or $F_b$ when braking.

The propulsive force ($F_a$) can be envisioned as a force input acting at the rear contact point of the collective rigid body with the ground. Similarly, for deceleration the force ($F_b$) input can be considered to be acting at the front contact point. These forces will be generated by some combination of leg actuation.

As mentioned previously, the tail is modelled as a point mass attached to an idealized massless rod of length $L_t$. Furthermore, the tail is actuated by an ideal torque actuator which is located some distance, $b$, away from the centre of mass (COM) of the collective body.

A number of assumptions were made in deriving the mathematical model. Firstly, it is assumed that during acceleration or braking only one force acts on the body. This is biomechanically accurate as for example during acceleration initiation, propulsion occurs primarily from the hind leg [23]. Secondly, a fixed geometry was considered even though a cheetah is capable of flexing its spine to shift the collective COM around. However, it is believed that the assumptions result in a conservative model which will still provide an understanding of the limitations in manoeuvrability and the positive effects a tail can provide.

Unlike the *Pitch then Power Model* [21], a dynamic model is presented. The system dynamics are modelled using the Euler-Lagrange method [56] [57] with the generalized coordinate vector as:

$$\boldsymbol{q} = [x \quad \theta_b \quad \theta_t]^T, \tag{3.1}$$

where $x$ is the COM longitudinal position of the rigid body with respect to the inertial frame, $\theta_b$is its pitch angle with respect to the horizon and $\theta_t$ is the relative angle between the tail and body. Additionally, $\alpha$, $a$ and $b$ are geometric properties of the collective body. The positions vectors for the body and tail respectively are:

$$\boldsymbol{p_b} = \begin{bmatrix} x \\ asin(\alpha + \theta_b) \end{bmatrix} \tag{3.2}$$

$$\boldsymbol{p_t} = \boldsymbol{p_b} + \begin{bmatrix} -bcos(\theta_b) - L_t \sin(\theta_b + \theta_t) \\ -bsin(\theta_b) + L_t \cos(\theta_b + \theta_t) \end{bmatrix} \tag{3.3}$$

Using these equations, the kinetic and potential energy can be derived and the Euler Lagrange Equations as described in Section 1.4 can be employed. For ease of reference these are repeated here:

$$\boldsymbol{M\ddot{q}} + \boldsymbol{C\dot{q}} + \boldsymbol{G} = \boldsymbol{B\tau} + \boldsymbol{A^T\lambda} \tag{3.4}$$

The acceleration and braking forces can be seen as generalized forces acting on the body [20] and can be derived as:

$$\boldsymbol{B} = \begin{bmatrix} 1 & 0 \\ \sigma_i & 0 \\ 0 & 1 \end{bmatrix}, \tag{3.5}$$

with $\sigma_i$ equating to $a\sin(\alpha + \theta_b)$ when accelerating and $a\sin(\alpha - \theta_b)$ when braking.

Also, note that the system contains hybrid dynamics and when the pitch angle $\theta_b$ falls to zero the constraint force (the $\boldsymbol{A\lambda}$ term), is activated[5]. This constrains the angle and prevents the model from falling through the ground.

Now that the system dynamics have been defined, the two manoeuvres can be simulated to determine the effectiveness of the tail actuator.

---

[5] For the braking model, the pitch angle is constrained to be negative.

### *3.1.2 Simulation*

In order to examine the benefits of an actuated tail for manoeuvrability tasks, models with and without the tail were simulated experiencing various force magnitudes (for braking and accelerating). It is predicted from the *Pitch then Power model* that there will be a point when the respective forces will be too excessive and will result in the body toppling over.

The cheetah parameters of the model are derived from geometric measurements provided by [2] [67] with the centre of mass assumed to be midpoint of the back length. The cheetah tail length is provided by [73], however at the time of conducting this research no measurements exist for the tail mass. This was stated in Section 1.1. As such, the tail mass is assumed to be 10% of the total body mass. The parameters are summarised in Table 3.

Table 3: Estimated Cheetah Parameters for LMT.

| **Parameter** | **Value** |
|---|---|
| Body Mass ( $\boldsymbol{m_b}$) | 45 (kg) |
| Body Roll Inertia ($\boldsymbol{I_B}$) | 7.344 (kgm$^2$) |
| Tail Mass ($\boldsymbol{m_t}$) | 4.5 (kg) |
| Tail Length ($\boldsymbol{L_t}$) | 0.75 (m) |
| Distance to COM ($\boldsymbol{a}$) | 0.7 (m) |
| Angle to COM ($\boldsymbol{\alpha}$) | 1.03 (rad) |
| Tail distance to COM ($\boldsymbol{b}$) | 0.36 (m) |

As indicated previously, the hypothesis is that the tail is being employed as an actuator in a pitch rate control loop. So, as a first attempt at a controller, the tail will be driven with a simple proportional controller (with a gain of 50).

The mathematical models were implemented in Simulink and numerically simulated. Each of the models (tailed and tailless) was subjected to various constant propulsive and braking forces. Similarly as in Section 2.1.3, the simulations terminated when the body flipped over, or the tail reached its full swing of 90 degrees. The resulting pitch angles as a function of acceleration force is depicted in Figure 3.3.

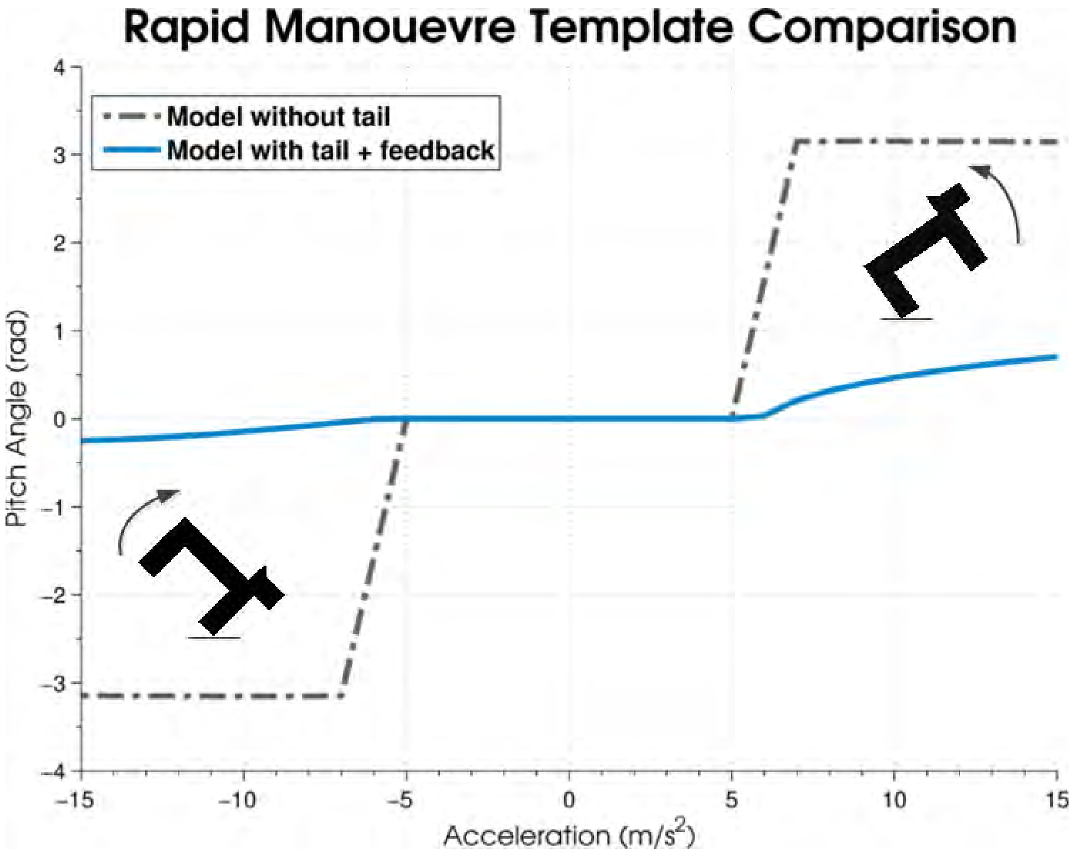

Figure 3.3: Acceleration force and resultant pitch angle plot. It is evident that the tailless model topples over when accelerating aggressively. Comparatively, the model with the tail can experience greater accelerations as the resultant pitch angle is decreased.

The results for this simple simulation study indicate that it is indeed possible for the cheetah to benefit from actuating its tail to negate the pitch rate incurred by manoeuvring. However, the results also demonstrate that a simple proportional controller is inadequate as a steady state error in the final pitch angle is incurred for larger magnitudes of acceleration.

With these preliminary results, the next step was to validate the hypothesis experimentally on a physical platform.

## 3.2 Mechanical Design

*Dima I* [14] was selected as the platform to test the rapid acceleration and braking hypothesis discussed previously. The robot is a high-speed platform previously designed to test a novel tail control system for turning at high-speed and its electrical, software and mechanical design is described in Section 2.2.

The robot's tail was modified for these tests to allow motions in the pitch axis. This was achieved by the addition of a set of bevel gears coupled to the Maxon DC motor of the tail as illustrated in Figure 3.4.

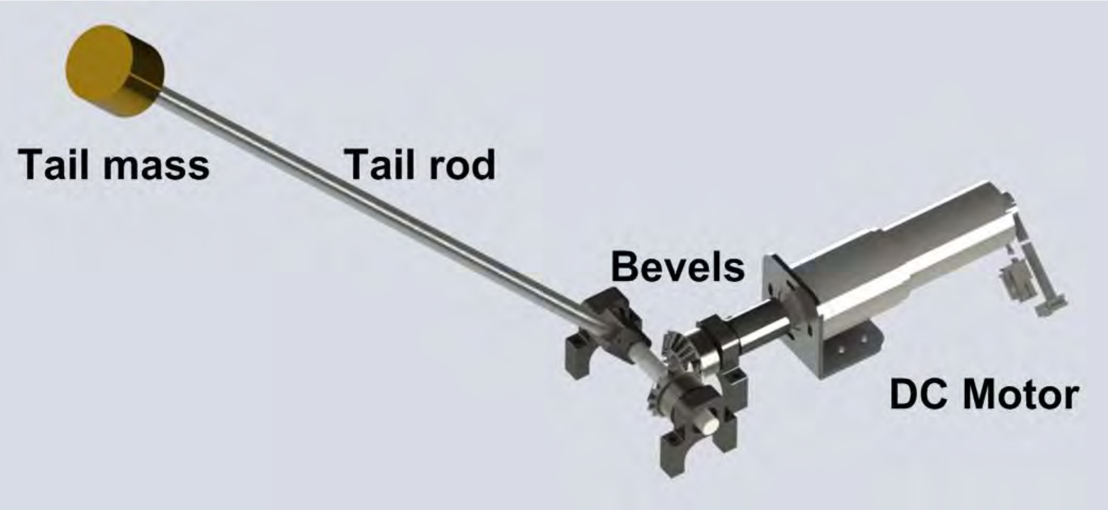

Figure 3.4: The original tail design of Dima I was modified by the addition of a set of bevel gears. This allowed the tail to be actuated in the pitch axis.

One may argue the relevance of testing the hypothesis on a wheeled platform but considering the discussion in Section 1.3, the LMT model provides a common "task encoder" [16]. For example, one can substitute the forces generated by a leg propelling the collected rigid body forwards for a wheel in contact with the ground. This is essentially the mechanism of moving from a template to an anchor. The task-level behaviour is fundamentally the same: a force is acting on a rigid body (cheetah or robot) to accelerate it. The reader should note however that the cheetah does leave the ground during the airborne phase of running. This could possibly result in differences between the results obtained, as the robot can only capture the dynamics during the stance phase.

To implement the braking force on the body various options were considered. A pneumatic disc brake system was considered, but due to weight and space constraints this was not feasible. Ultimately, it was decided to implement an arrestor system based on a fishing reel (*Okuma Convector CS45*) and 1mm nylon fishing line. The line was tied in between the two front wheels and the fishing reel bolted to the ground. The reel was engaged to simulate a large deceleration force.

Now that the platform has clearly been defined an in depth controller design will be presented for the two manoeuvrability tasks. These will then be simulated in order to validate them before field testing.

## 3.3 Rapid Deceleration

### 3.3.1 *Force Model Identification*

As decided previously, to implement a large deceleration force an arrestor system was developed comprising of nylon line and a fishing reel. However, to adequately design the tail controllers, an accurate model of this braking force was required. It was assumed that the line behaves visco-elastically and can be modelled as a second order system [74]. Thus the force is described as:

$$F_b = E\varepsilon + \eta\dot{\varepsilon} \tag{3.6}$$

where, *E* is the elastic modulus, $\varepsilon$ is the strain and $\eta$ is the viscosity of the material. In order to estimate these parameters for this linear model, data was logged on board *Dima I* and rapid braking tests were performed without the tail.

The parameters were then estimated using Matlab's ***lsqnonlin*** function for nonlinear curve fitting. This was done by matching the linear models coefficients to the nonlinear braking model simulation for *Dima I*. The LMT model parameters for *Dima I* are provided in Table 4. The parameter fit and experimental data are also graphically compared in Figure 3.5.

Table 4: *Dima I* Pitch Model parameters

| **Parameter** | **Acceleration** | **Braking** |
|---|---|---|
| Body Mass ( $\boldsymbol{m_b}$) | 5 (kg) | |
| Body Pitch Inertia ($\boldsymbol{I_B}$) | 0.122 | 0.179 (kgm$^2$) |
| Tail Mass ($\boldsymbol{m_t}$) | 0.4 (kg) | |
| Tail Length ($\boldsymbol{L_t}$) | 0.5 (m) | |
| Distance to COM (***a***) | 0.242 | 0.266 (m) |
| Angle to COM ($\boldsymbol{\alpha}$) | 1.144 | 0.972 (rad) |
| Tail distance to COM (***b***) | 0.1 (m) | |

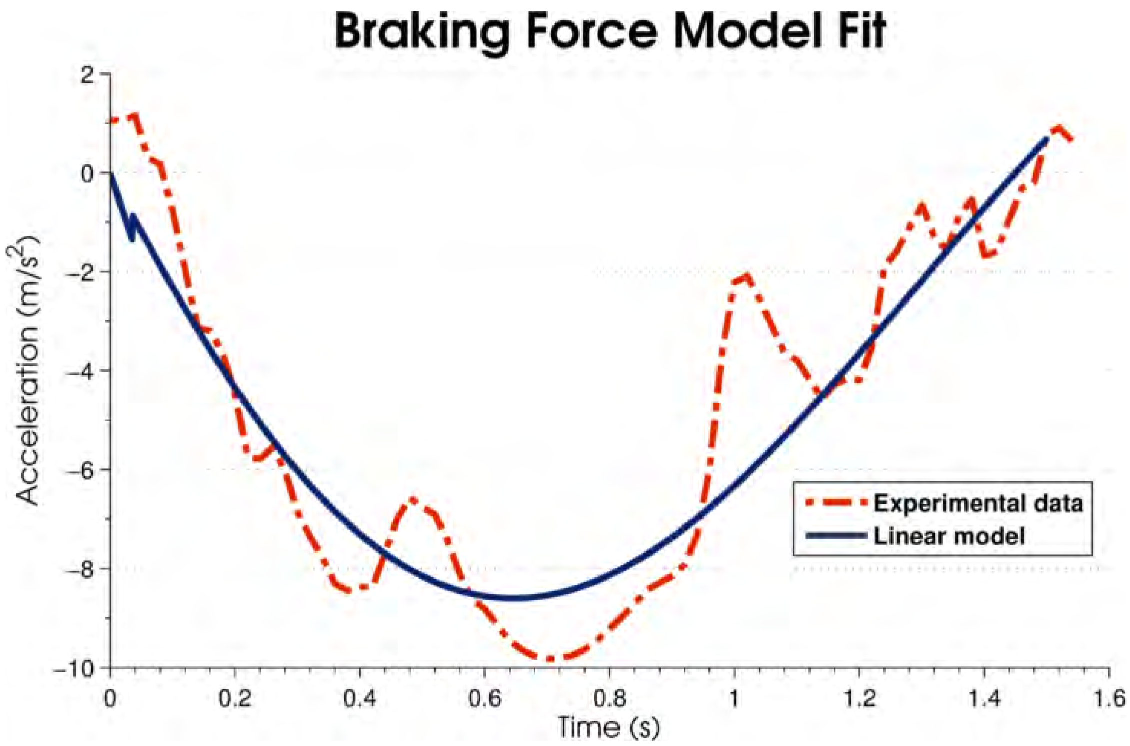

Figure 3.5: Second order force model fit for the braking force induced by the nylon line is shown with $E$ = 24.7 and $\eta$ = 2.82. The simulation model was initialised at a velocity of 4.5 m/s to match the experiment conditions.

Now that the model has been satisfactorily defined, the feedback control algorithms for the tail can be designed.

### *3.3.2 Tail Controller Design*

As shown in Section 3.1, when the LMT model experiences aggressive accelerations, it topples over. Hence, the motivation here is that if the tail is employed as an actuator for a pitch rate controller, this induced (disturbance) torque can be countered, and the robot can accelerate more aggressively.

The Longitudinal Manoeuvre Model (LMT) is nonlinear and under actuated [59]. Based on previous work done in Chapter 2 for high-speed turning, the following controller architecture is proposed and is illustrated in Figure 3.6.

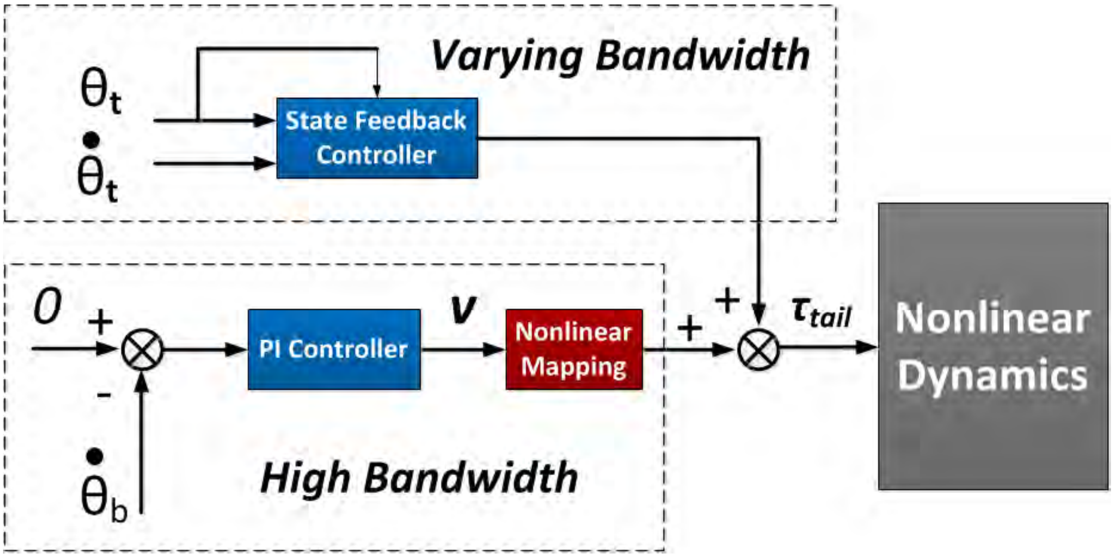

Figure 3.6: Tail controller architecture implemented.

The primary goal for the controller architecture is to regulate the pitch rate of the body. As illustrated in the initial simulations of Section 3.1 however, a steady state error occurred. Thus, a high-bandwidth PI (proportional + integral) controller was implemented to drive the pitch rate to zero and also to diminish any modelling inaccuracy. The gains selected are $k_I$= 25 and $k_P$= 8.

Now, to map the controller's output as a torque command to the tail, a Partial Feedback Linearization (PFL) [60] was considered. However, the framework is augmented with the addition of a disturbance term, $\boldsymbol{D}$, which is:

$$\boldsymbol{D} = \begin{bmatrix} 1 \\ \sigma_i \\ 0 \end{bmatrix} F_i, \tag{3.7}$$

where $F_i$ is either the acceleration force or the braking force acting on the contact point of the collective rigid body and $\sigma_i$ has been previously defined. This will encapsulate the disturbance force that the body experiences due to acceleration/braking.

Furthermore this implies that if the actuated joint ($\theta_t$) is commanded such that:

$$\ddot{\theta}_t = \bar{\boldsymbol{J}}^{+}[v + \boldsymbol{J_1} \boldsymbol{M_{11}^{-1}}(\boldsymbol{h_1} + \boldsymbol{\varphi_1} - \boldsymbol{D})], \tag{3.8}$$

where, the matrices $\bar{\boldsymbol{J}}^{+}$, $\boldsymbol{J_1} \boldsymbol{M_{11}^{-1}}$, $\boldsymbol{h_1}$ and $\boldsymbol{\varphi}_1$ are defined in [60], we then have:

$$\ddot{\theta}_b = v, \tag{3.9}$$

which is a now a linear system.

As observed in Chapter 2, when the tail reaches its angular limits, it has significant velocity, which can negate the stabilization that it just performed when it strikes the end stops or ground. This constraint is especially important in this study as the robot only has 90° of actuation.

In a similar manner to Chapter 2, another controller is employed, to decrease the velocity of the tail when reaching the end stops. Whereas the previous study employed a fixed gain controller relying on timescale separation, the bandwidth of this “tail spring damper” was varied as a function of the tail angle. Thus, the natural frequency scale factor of this tail damper was governed by:

$$w_{fac} = \gamma e^{(-\delta \theta_t)} \tag{3.10}$$

where $\gamma$ are $\delta$ are parameters to be chosen. The scale factor was then multiplied by the pitch rate controller’s bandwidth (5 rad/s). By pole placement, the appropriate tail angle and velocity gains can be set.

To select $\gamma$ and $\delta$ for the system, numerical optimization is employed to minimize the cost function:

$$J = \int_{\mathbf{0}}^{\boldsymbol{t_f}} 100\dot{\theta}_b^2(t)\, dt + 0.5\dot{\theta}_t(t_f) \tag{3.11}$$

Note that $t_f$ is the simulation end time and that the weights were selected such that pitch rate damping was deemed more critical than end tail velocity. Matlab’s constrained optimization ***fmincon*** was subsequently utilized to determine the optimal parameters for $\gamma$ and $\delta$ by simulating the full control architecture at the maximum velocity of the car (approximately 9m/s).

There was a clear compromise between the tail’s velocity at the end of its travel and its ability to stabilize the pitch rate. After several iterations of initial solution seeds, the values of $\gamma = 2.56$ and $\delta = 9.35$ were chosen. This reduced the final tail velocity from 25 to 10 rad/s, while still providing sufficient pitch stabilization. A comparison illustrating the effects of the tail damper is shown in Figure 3.7.

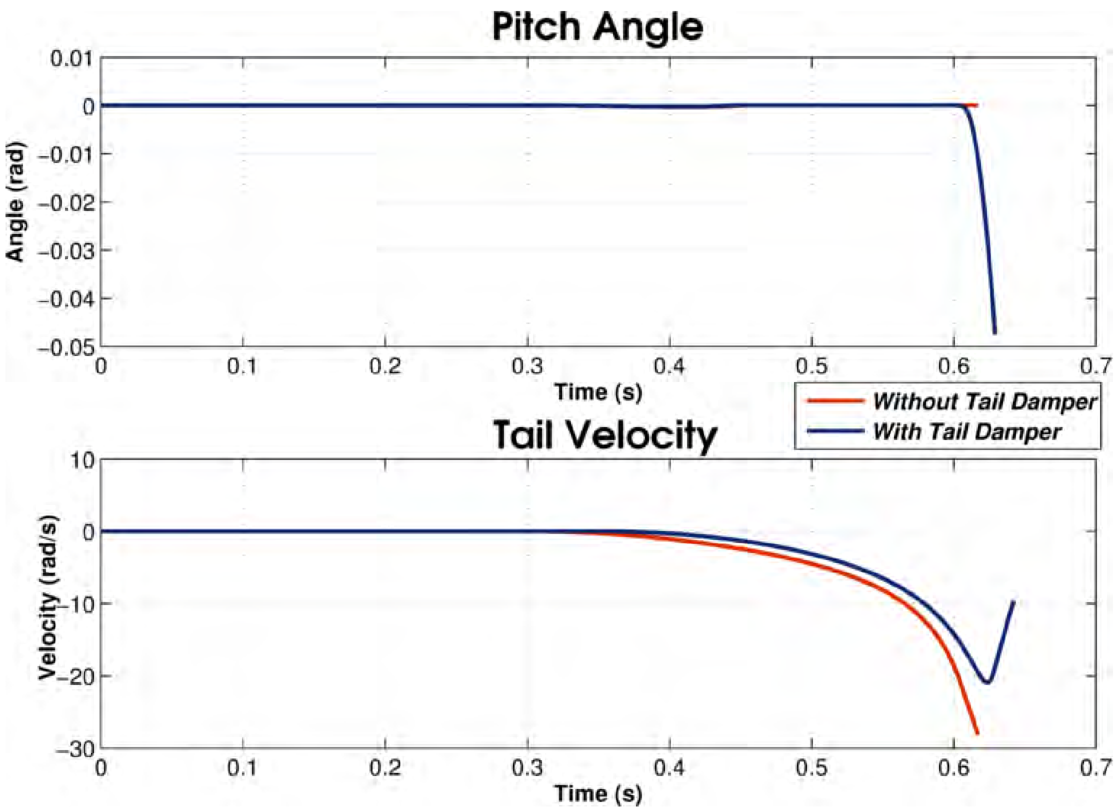

Figure 3.7: Plot of the body pitch angle and tail velocity. It is evident that the tail damper reduces the tails end velocity, but pitch rate control is diminished slightly.

### *3.3.3 Simulation*

The controllers were then simulated at various initial velocities to determine the maximum deceleration (peak value) which could be obtained. The conditions for the simulation terminating were the same as discussed in Section 3.1.2.

For the tailless version a maximum deceleration of 9 m/s$^2$ was obtained at a velocity of 5 m/s. When attempting initial velocities greater than this, the robot would topple over.

The model with the actuated tail achieved a peak deceleration of 23 m/s$^2$ at a maximum velocity of 8 m/s. This did however result in an end tail velocity of approximately 8 rad/s, which could be detrimental during the experimental testing. Screenshots of the animation produced by the simulation are also shown in Figure 3.8 and it can be seen that the tail is only actuated when the braking force is sufficiently large.

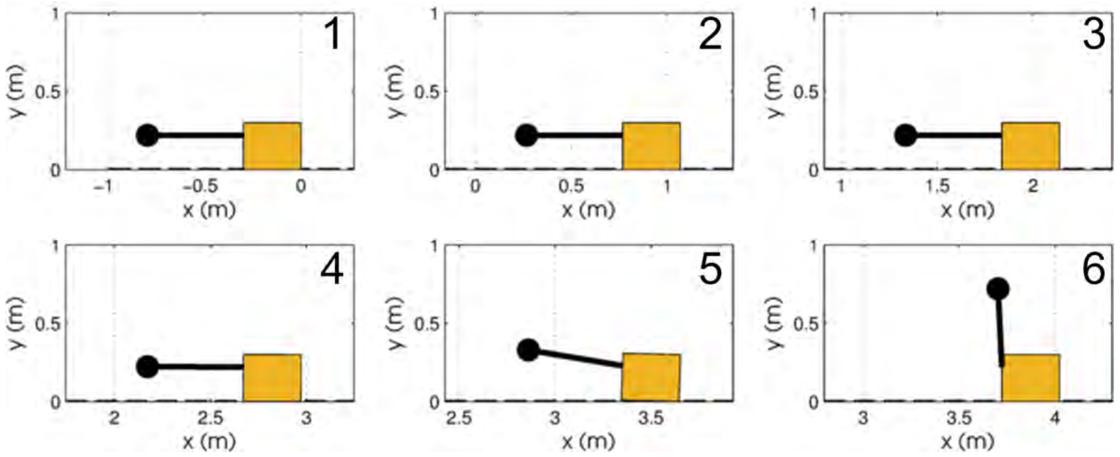

Figure 3.8: Simulation of the tailed robot performing a rapid deceleration at an initial velocity of 8 m/s

## 3.4 Rapid Acceleration

### 3.4.1 *Force Model Identification*

The acceleration force was provided by a brushless DC motor (*Traxxas Velineon*) controlled by PWM. As with the braking, this system is modelled as a force input disturbance. It is noted that control of this as an input to the system is possible, but to keep uniformity of the control architecture, it is assumed to be an input disturbance.

Simple step tests were performed on *Dima I* to determine the model parameters. The force equation in the Laplace domain is given by:

$$F_a = k_v \frac{\omega_{mech}}{s + \omega_{mech}} (V_{in} - k_\omega s x) \tag{3.12}$$

where $k_v$, $\omega_{mech}$and $k_\omega$ are model parameters and $V_{in}$ is the voltage input produced by PWM.

Data from a 40% throttle step was used and in a similar method, Matlab's ***lsqnonlin*** was employed to fit the parameter values. A comparison between the fit and the experimental data is depicted in Figure 3.9.

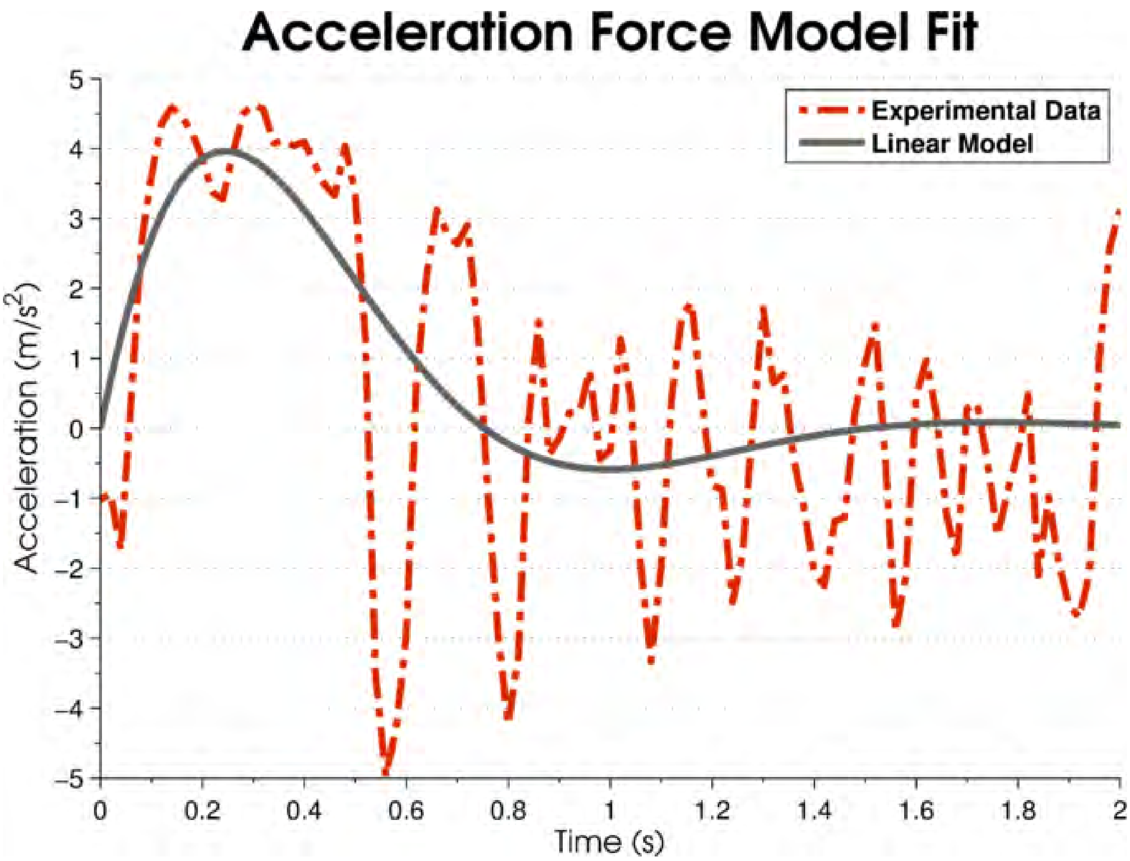

Figure 3.9: Linear model fit for the acceleration produced by the brushless DC motor. The data was taken from a 40% throttle step. The oscillations are attributed to the uneven grass where the test occurred.

### *3.4.2 Tail Controller Design*

If the acceleration force is considered to be a disturbance, then the same controller architecture can be employed for the acceleration manoeuvres as described in Section 3.3.2.

### *3.4.3 Simulation*

The models were then simulated by stepping the throttle to various values. The performance metric used was the peak acceleration experienced.

The tail-less model obtained a maximum acceleration of 4 $m/s^2$ at a throttle input of 40%. Any greater steps caused it to pitch over.

The model with an actuated tail obtained an acceleration of 10.8 $m/s^2$ at throttle input of 90%. However, even with the tail damper discussed, the tail still had an end velocity of 8 rad/s which could be detrimental during experimentation.

## 3.5 Experiments

The tail controller algorithms were then field tested on the robot performing the braking and acceleration manoeuvres. The performance metric for both was the peak accelerations experienced. The test procedure for braking was as follows:

- The robot would drive straight until attaining the predefined initial velocity
- Then, simultaneously the arrestor system would engage and the robot's motor would stop
- The initial velocity was increased till toppling occurred

For the rapid acceleration tests, the procedure was:

- The throttle would be stepped to a constant value
- Once the tail had reached the end stop, the throttle would be set to zero and the test ended.

### *3.5.1 Results*

The results for the rapid deceleration are depicted in Figure 3.10. The peak deceleration for the tailless model was 9.9 ± 0.81 $m/s^2$ at an initial velocity of 4.5 m/s. The peak deceleration for the model with the tail was 15.2 ± 0.89 $m/s^2$ at a velocity of 6.5 m/s.

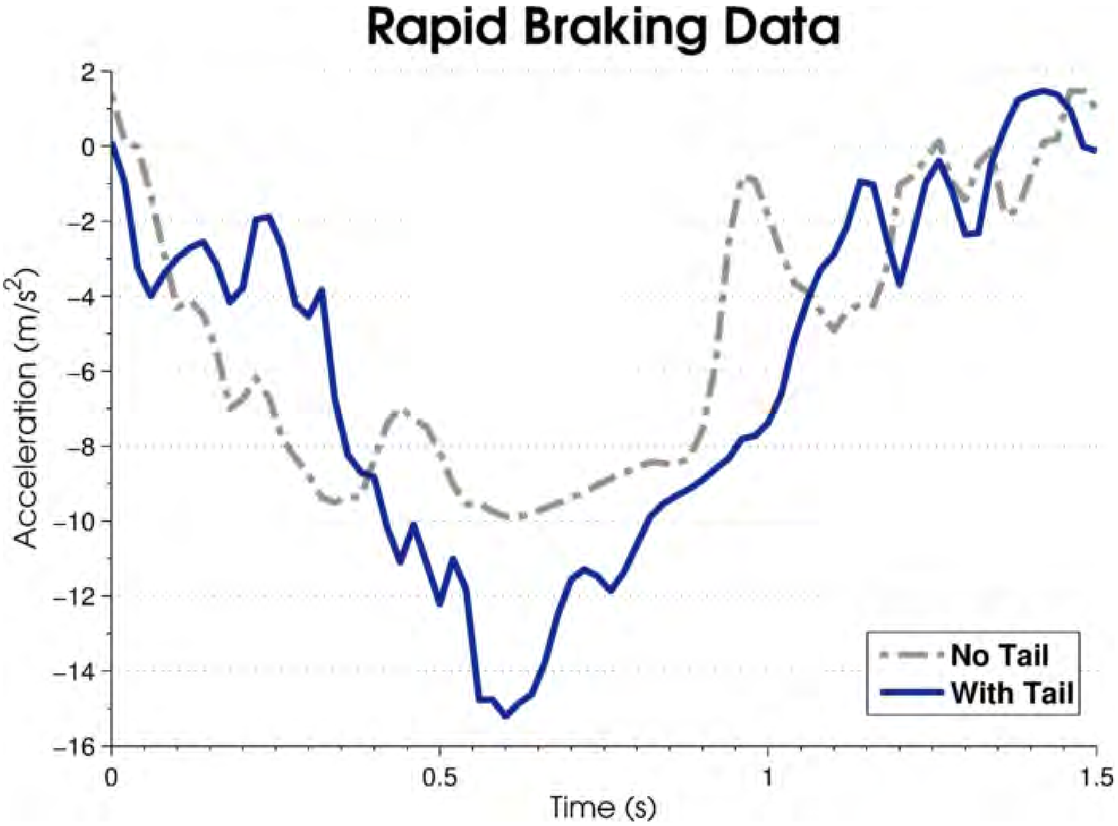

Figure 3.10: Comparative rapid deceleration data for the robot with and without the tail.

The results for the rapid acceleration are depicted in Figure 3.11 and Figure 3.12. The peak acceleration for the tailless robot was 4.1 ± 0.231 m/s$^2$.The peak acceleration for the robot with the tail was 6.1 ± 0.298 m/s$^2$. The reader is also encouraged to view the attached video comparison (see supplementary video material on DVD).

Figure 3.11: A rapid acceleration test (90% throttle step) with the tail controller is depicted. Images at 30 fps.

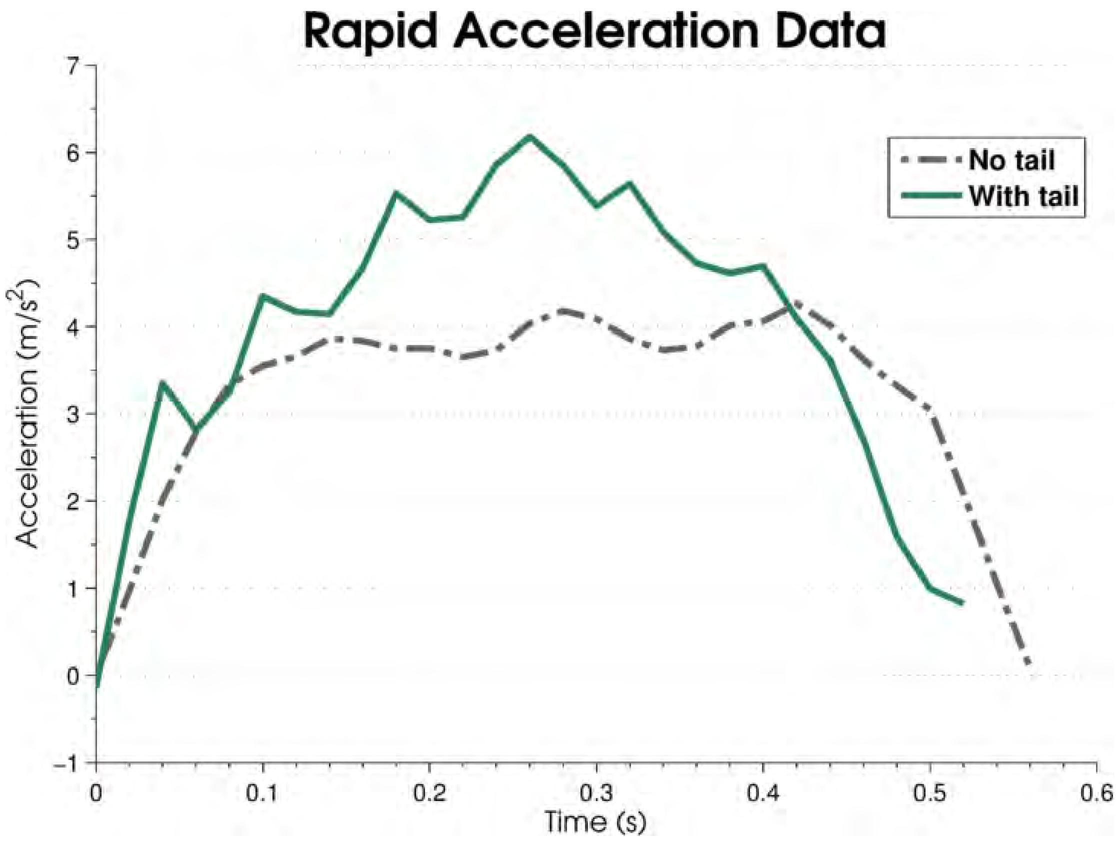

Figure 3.12: Comparative experimental data for the acceleration manoeuvre for the tailed and the tailless robot.

## 3.6 Discussion

The tailed robot produced approximately 50% more acceleration in both test scenarios than the tailless version. In absolute terms these were both less than those predicted by the simulations.

For the acceleration tests, this is attributed to the current limiter on the car's motor controller as the step tests from 70 to 100% throttle all produced the same accelerations.

However, the chief reason for the difference in both manoeuvres is the tail's end velocity. When attempting more aggressive manoeuvres (braking or accelerating), the tail often struck the end stops with enough velocity to induce a flipping motion. The reason is that the interaction between the grass and the vehicle was not modelled, and such the controller attempted to compensate by commanding more motor torque. Here, the tail often struck the roll cage or end stops with velocities greater than 15 rad/s. This collision was not accounted for in simulation as it would make the model significantly more complex.

Nevertheless, this study has provided valuable insights to understanding the motion. What is evident is that for the cheetah (or a future robot) to optimally use a tail for these tasks, it would need to coordinate the force and the tail trajectories. This would ensure that the tail actuation limits are adhered to, while simultaneously maximising acceleration. A similar problem was observed in Chapter 2 and presents an intrinsic difficulty with employing the tail in this manner. The cheetah body would also be airborne for certain phases of the gallop which would mean that the tail would be more effective at pitch stabilization as discussed in Section 1.4.

Additionally, the cheetah's tail is compliant which means it will absorb any impacts with the body or ground during manoeuvres.  Moreover, the cheetah tail is capable of a much larger stroke than the robot as seen Figure 3.1. This would allow it to provide more actuation during manoeuvres.

# Chapter 4

## Tail Motion in a Cone

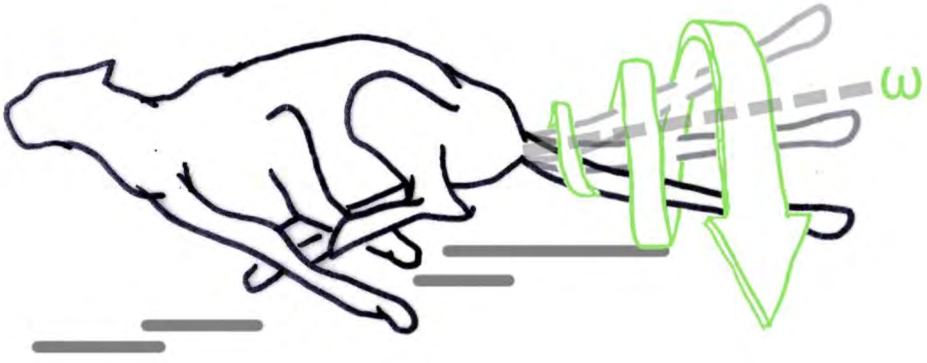

In Chapter 2, use of the tail during short, rapid turning manoeuvres was demonstrated. During these, the tail was capable of imparting a large angular impulse despite the short time duration. The limitation to extending to longer manoeuvres was that the tail angular limits were reached by the end of the manoeuvre. However, it was observed in several videos that when the cheetah is in a constant turn, it moves the tail in a cone [11] [70]. This constitutes a combination of pitching and yawing.

In this chapter, the hypothesis is that this cone motion imparts a roll torque on the body over the duration of a complete stride. Firstly, a mathematical model of a simplified two degree of freedom tail, which is capable of pitching and rolling, is presented. Using this model, trajectory optimization is performed to determine if the cone motion is indeed the optimal trajectory for a high speed gallop turn. Subsequently, a novel robot platform, *Dima II*, is developed which comprises a two degree of freedom tail actuator. Then, with insights gained from the optimized open loop trajectories, a feedback controller is designed for the tail which commands it to swing in a cone. Next, via experiments it is demonstrated that the two degree of freedom tail can impart a roll torque on the robot during high-speed turns. Finally, the results as well as the biological implications of this motion in the cheetah are discussed.

## 4.1 Tail motion in a Cone

### *4.1.1 Inspiration*

During various wildlife documentaries the cheetah is often seen swinging its tail in the shape of a cone. After frame by frame analysis, it can be seen that this motion occurs during longer duration turns, i.e. over multiple stance phases. This is shown in Figure 4.1. The reader will recall that Chapter 2 discussed initiating turns at high speed, but the model only factored in initiation of the turn during one stance.

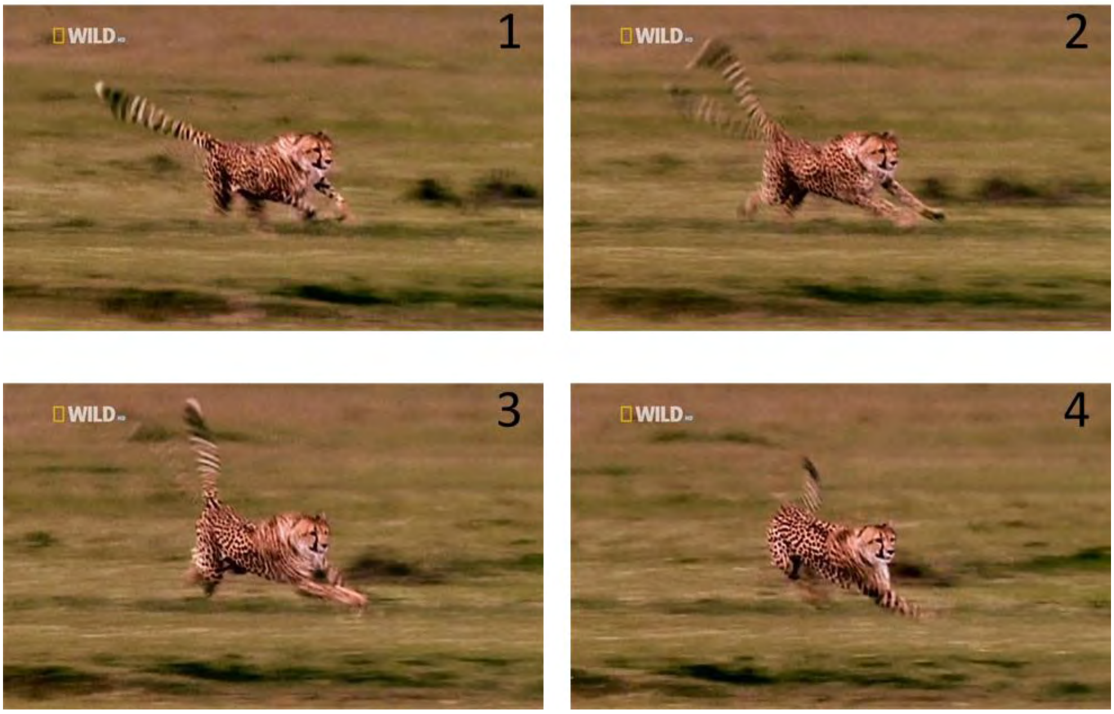

Figure 4.1: Cheetah performing the cone motion during a constant turn. This motion is created by a combination of pitching and yawing of the tail. Images seen at 25 fps captured from footage in *I, Predator* [70].

In this chapter, the hypothesis is that during a stride (or multiples thereof) the cheetah is capable of providing the reaction torque required to counteract the centrifugal toppling moment previously discussed. It does this by swinging the tail in a cone shape, which provides a roll torque on the body during the stance phase of the stride. Additionally, this tail motion provides two advantages:

- During the aerial phase the tail can either roll the body (as discussed in Section 1.4 and in [46] and [16]), or swing at a constant velocity to impart zero torque on the body.
- During the next phase of stance (after the aerial phase), the tail is in the correct position to provide more roll torque.

This concept is illustrated in Figure 4.2.

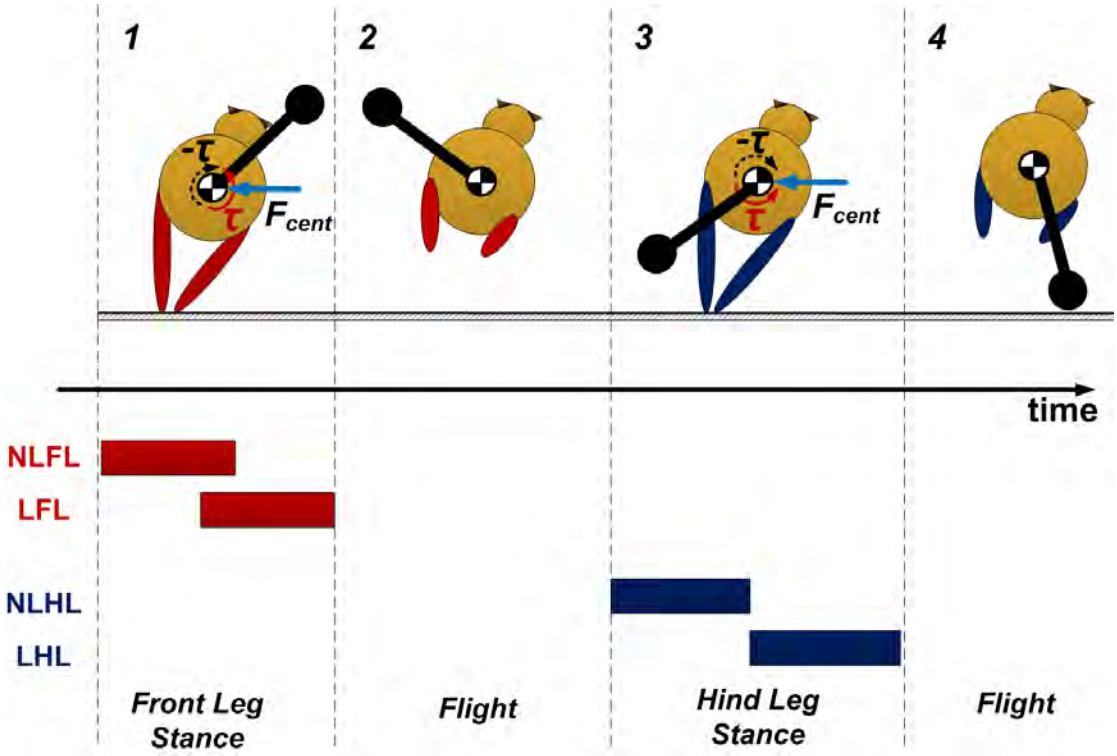

Figure 4.2: Timing diagram representing a cheetah turning while galloping. During the stance phases (1, 3), the body will be acted on by a centrifugal force. However during the aerial phase there are no external torques which could cause body roll. During phases 1 and 3, the tail can thus impart the necessary reaction torque. NLFL and LFL represent the footfall timings for the Non-Lead Forelimb and Lead Forelimb respectively. NLHL and LHL represent the footfall timings for the Non-Lead Hind limb and Lead Hind limb respectively. This represents the timing of a rotary gallop discussed in Hudson et al. [67]

It is worth noting the difference between the concepts in Chapter 2 and the current work. Consider a tail moving in pure roll as discussed in Chapter 2 during Phase 1: if the tail reaches its angular limits but more roll torque is required for subsequent phases, the only way the tail can actuate more is to move the tail in the opposite direction. Consequently, this will naturally cause a roll in the opposite direction which will exacerbate the toppling torque or roll the body in the opposite direction during the aerial phases.

In the subsequent subsections, the dynamics are derived for a two degree of freedom tail. Then, Trajectory Optimization is employed to determine if the cone motion is indeed the optimal trajectory during turning while galloping.

### 4.1.2 *Mathematical Modelling*

The first task is to model a two degree of freedom tail. Once more, Euler Lagrange Mechanics, as described in Section 1.4, is utilized. For simplicity, it is assumed that the tail can be considered a mass attached to a massless rod. This is an assumption for the cheetah tail (as was discovered in Chapter 5), however it will still provide insight into the motion. The proposed model is illustrated in Figure 4.3.

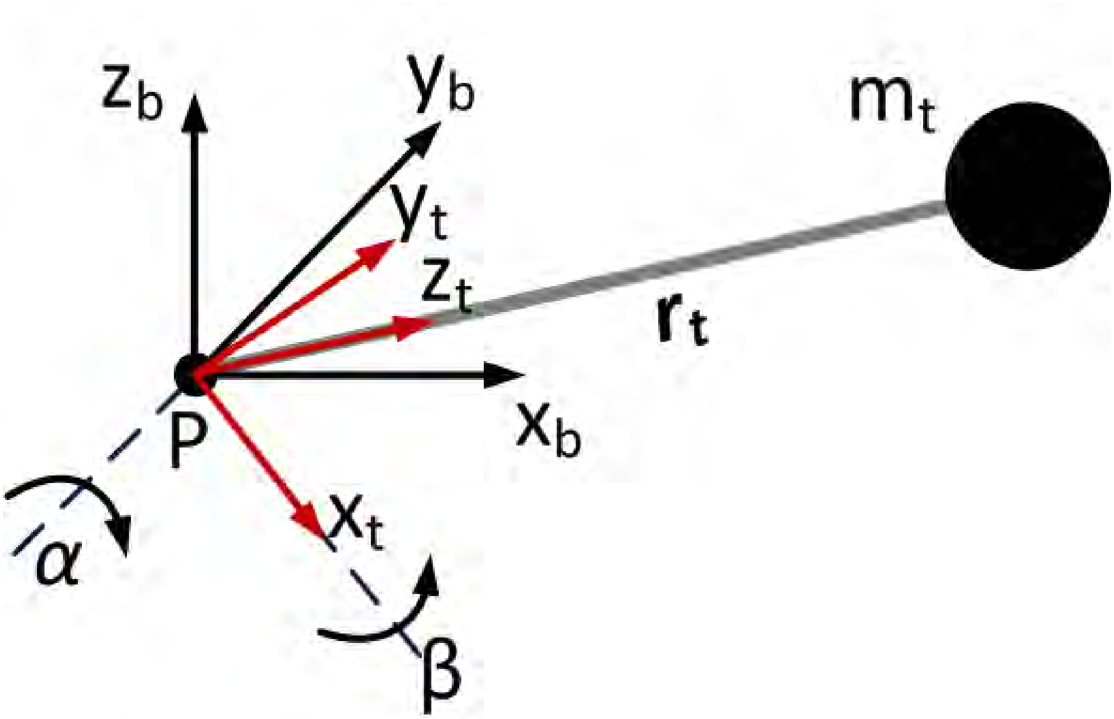

Figure 4.3: Diagram of the Two DOF Tail Model. The tail can rotate by first pitching by an angle ($\alpha$) about the body Y-axis ($y_b$) and then by rolling by an angle ($\beta$) about the X-axis of the tail frame ($x_t$).

The position of the tail mass in the tail frame $\boldsymbol{r_t^t}$ is given by:

$$\boldsymbol{r_t^t} = \begin{bmatrix} 0 \\ 0 \\ L_t \end{bmatrix}, \tag{4.1}$$

where as in previous chapters, $L_t$ is the tail length.

To define the position of the tail mass in the body frame, use of a rotation matrix ($\boldsymbol{R_t^b}$) must be made which rotates vectors in the tail frame to the body frame, such that:

$$\boldsymbol{r_t^b} = \boldsymbol{R_t^b r_t^t} \tag{4.2}$$

An Euler angle set defines this rotation matrix. This is expressed given as:

$$\boldsymbol{R_t^b} = \begin{bmatrix} \cos(\alpha) & \sin(\alpha)\sin(\beta) & \cos(\beta)\sin(\alpha) \\ 0 & \cos(\beta) & -\sin(\beta) \\ -\sin(\alpha) & \cos(\alpha)\,sin(\beta) & \cos(\alpha)\cos(\beta) \end{bmatrix}, \tag{4.3}$$

and is derived by first rotating about the Y-axis in the body frame by an angle $\alpha$, then taking this new axis and rotating it about its X-axis by an angle $\beta$.

The Euler-Lagrange method does not provide the reaction forces or torques between bodies. However, it desired to determine the roll torque effect the tail cone motion has on the body during turning. Thus, an additional redundant coordinate is introduced and then constrained as per the method described in Section 1.3.

To implement the constraint, the body roll angle ($\varphi$) can be introduced as a redundant coordinate. The generalised coordinate vector is then given by:

$$\boldsymbol{q} = [\varphi \quad \alpha \quad \beta]^T \tag{4.4}$$

Now, if the roll angle is constrained to be zero, the constraint torque provided will be a measure of the reaction torque of the tail on the body. To determine the constraint force equation (1.4) from Section 1.3 is used.

The rotation matrix relating the body frame to the inertial frame is given by:

$$\boldsymbol{R_b^I} = \begin{bmatrix} 1 & 0 & 0 \\ 0 & \cos(\varphi) & -\sin(\varphi) \\ 0 & sin(\varphi) & \cos(\varphi) \end{bmatrix}. \tag{4.5}$$

It follows that the tail position in the inertial frame is given by:

$$\boldsymbol{r_t^I} = \boldsymbol{R_b^I R_t^b r_t^t} \tag{4.6}$$

The Euler-Lagrange equations require the kinetic energy for the system, and as such the velocities of the tail are to be derived. With respect to the inertial frame, tail velocity is given by:

$$\boldsymbol{\dot{r}_t^I} = \boldsymbol{\omega_t^I} \times \boldsymbol{r_t^I} \tag{4.7}$$

where $\boldsymbol{\omega_t^I}$ represents the angular velocity of the body. Now, noting that Euler angles do not represent an absolute rotation but a rotation relative to subsequent axes [56], the respective Euler angular velocity vectors first need to be rotated before they can be added. Thus,

$$\boldsymbol{\omega_t^I} = \dot{\varphi} \begin{bmatrix} 1 \\ 0 \\ 0 \end{bmatrix} + \dot{\alpha} \boldsymbol{R_b^I} \begin{bmatrix} 0 \\ 1 \\ 0 \end{bmatrix} + \dot{\beta} \boldsymbol{R_b^I R_1^{-1}} \begin{bmatrix} 1 \\ 0 \\ 0 \end{bmatrix} \tag{4.8}$$

Note that $\boldsymbol{R_1}$ represents the first rotation matrix defining the rotation from the body by the tail pitch angle ($\alpha$).

Finally, the total kinetic energy can be expressed as:

$$T_{tot} = \frac{1}{2}\left(I_b \dot{\varphi}^2 + m_t \boldsymbol{\dot{r}_t^I}^{\boldsymbol{T}} \boldsymbol{\dot{r}_t^I}\right) \tag{4.9}$$

Using this, the equations of motion can be derived and place in the form of equation (1.1). Note that the input torque mapping is given by:

$$\boldsymbol{B} = \begin{bmatrix} 0 & 0 \\ 1 & 0 \\ 0 & 1 \end{bmatrix} \tag{4.10}$$

### 4.1.3 Numerical Optimization

Based on the discussion in Section 4.1.1, it is desired to understand if the tail cone motion is indeed the optimal motion to perform during the manoeuvre illustrated in Figure 4.2. Thus, it is proposed that if the cheetah is indeed in a sharp galloping turn, it will require torque on the body during the stance phases and zero[6] torque during the flight phase. This would require a careful coordination of the tail movement with stances phases which is observed in [70].This is illustrated in Figure 4.4.

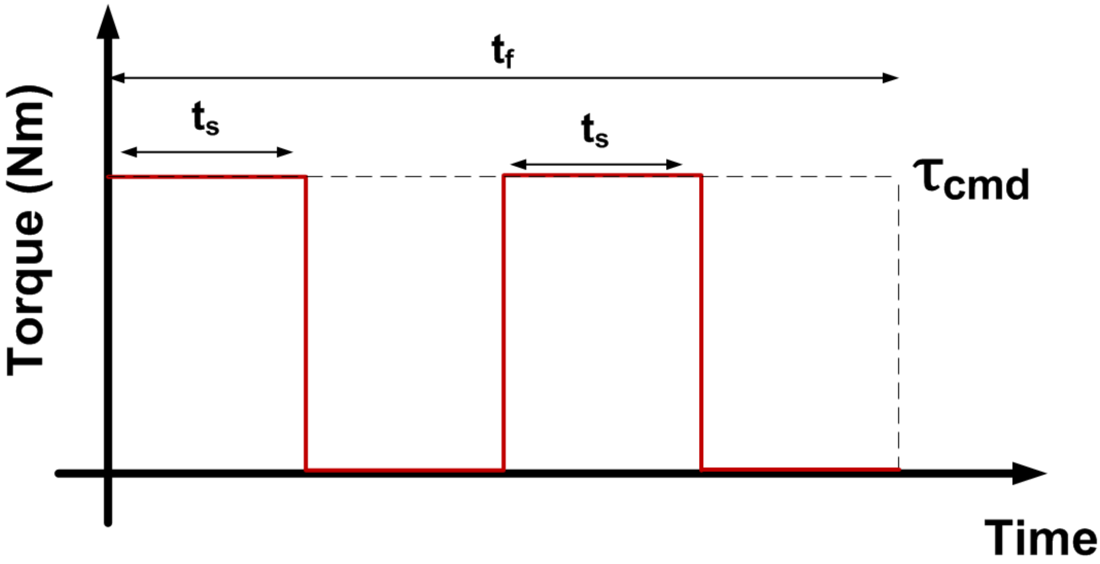

Figure 4.4: Desired torque profile across a single stride during a turn at high speed. It is assumed that torque will be required from the tail on the body during the stance phases and zero torque will be desired during aerial phases. Note that the duration $t_s$ represents the time in both hind leg stance and foreleg stance, and $t_f$ represents the time for the complete stride.

To perform the optimization, an adequate cost function is required. It was decided to implement a tracking cost function [75] where the cost is:

$$J = \int_0^{t_f} (\tau_{desired} - \lambda)^2 \, dt \tag{4.11}$$

where, $\lambda$ is the torque imparted by the tail on the body (the reaction torque) in the roll axis.

---

[6] Assuming that the body is already banked to the correct roll angle.

For the torque profile, a $t_s$ of 0.1s and a $t_f$ of 0.4s will be used. This is based on discussions on high speed galloping of the cheetah described in Hudson et al. [67] where it was shown that the cheetah gallops at a duty cycle of around 50% at frequencies of approximately 3 to 4 Hz.

As discussed in Section 1.3, the two DOF tail model will be utilized as part of a single shooting optimization. Matlab's ***fmincon*** will be employed with the built-in Active-Set Algorithm. The finite difference step value was set to 1e-6 and all tolerance parameters were set to 1e-5 as advised in previous studies [63] [46].

Each of the two input torque trajectories was discretised with a grid size ($n_{grid}$) of 19 and was linearly interpolated. The only constraints were those imposed on the tail pitch and roll angles. Where:

$$0 \leq \alpha \leq 150° \tag{4.12}$$

$$-60° \leq \beta \leq 60° \tag{4.13}$$

These were derived from the various video observations described previously. The model was then simulated in Simulink using the ***ode45*** solver with all the tolerances set to 1e-9. The parameters for the tail model were those of *Dima I* detailed in Chapter 2 and 3.

Finally, it should be stated that the trajectory optimization methods employed by ***fmincon*** can only produce a locally optimal solution. To determine a global solution, Matlab's ***globalSearch*** function is utilized which employs a scatter-search algorithm [76] to generate a large number of random sample of points. For this optimization a value of 2000 random samples was selected, which took approximately 48 hours to execute. It should be noted, the optimizer often did not converge to a solution.

For a torque of 8 Nm during the stance phases, the following 100 input torque trajectories discovered by the optimizer are shown below in Figure 4.5.

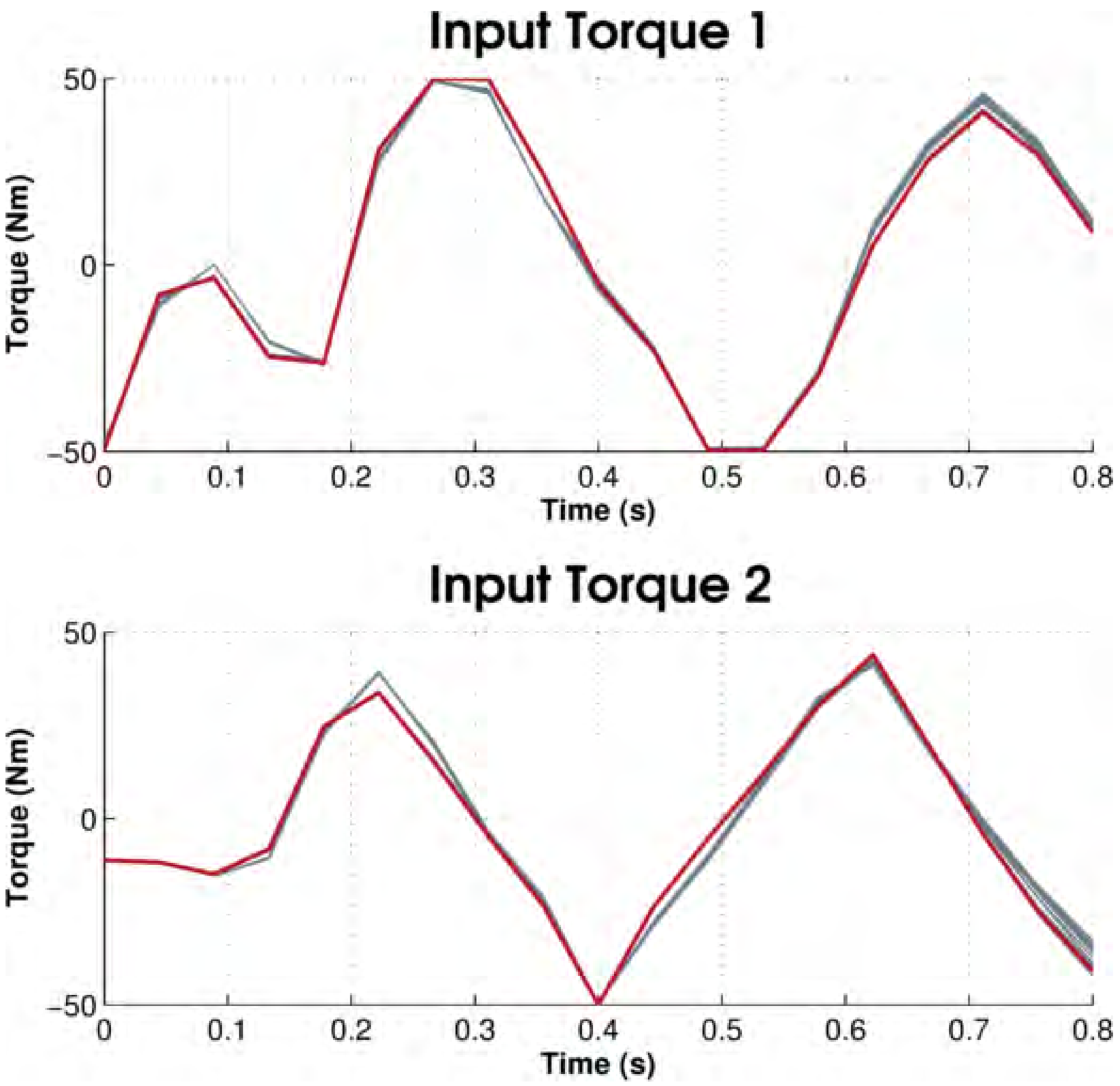

Figure 4.5: Optimal input torque trajectories for the torque profile of 8 Nm specified. The plot in red represents the global minimum and the grey plots represent local minima.

For this optimal input trajectory, the corresponding torque on the body as well as the tail Euler angles is shown in Figure 4.6. This plot presents interesting points. Firstly, it can be seen that the resulting torque experienced by the body accurately tracks that desired. Secondly, the corresponding tail motion which creates this torque profile on the body is a cyclic motion due to an approximately periodic trajectory of the Euler Angle plots shown.

The global cost obtained by the optimizer was 0.255. This could be improved, which would result in a more accurate tracking of the desired torque, but it would require an increase in the number of grid points. However, this result was deemed adequate to gain insight and increasing the number of optimized variables from the current 38 (two torque trajectories discretised at 19 points) would increase the optimization time substantially.

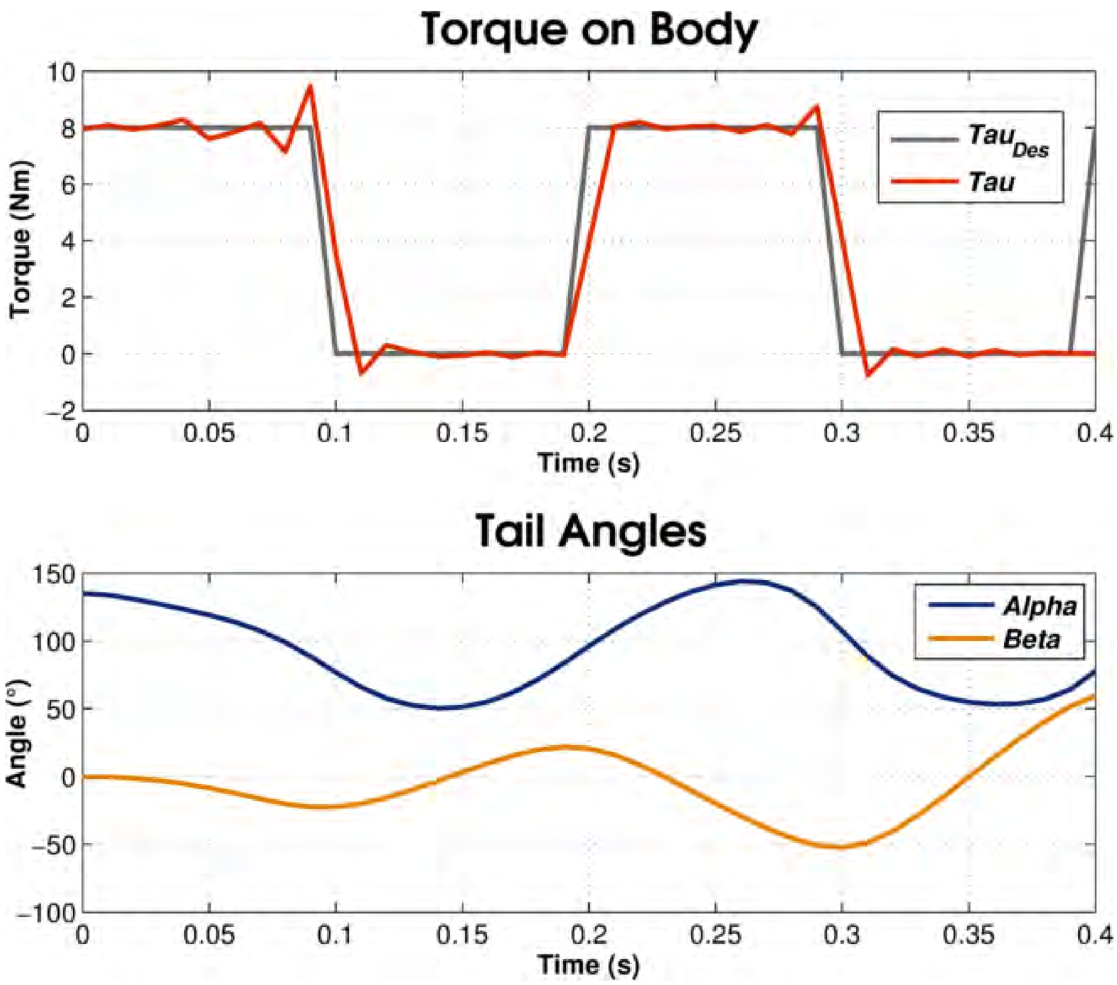

Figure 4.6: Upper figure - Roll torque imparted on the body is shown with corresponding desired torque. It can be seen that the profile is being tracked adequately. Lower figure – The corresponding Euler Angles produces by the optimal torque trajectory as shown. It is evident that a periodic motion is presenting itself.

With insights gained from this optimization exercise, feedback controllers can be designed to be tested on a physical robot platform. This will be the subject of Section 4.3 where a PFL controller design is presented. The next section explains the design of a two degree of freedom tailed robot which the aforementioned controllers were tested on.

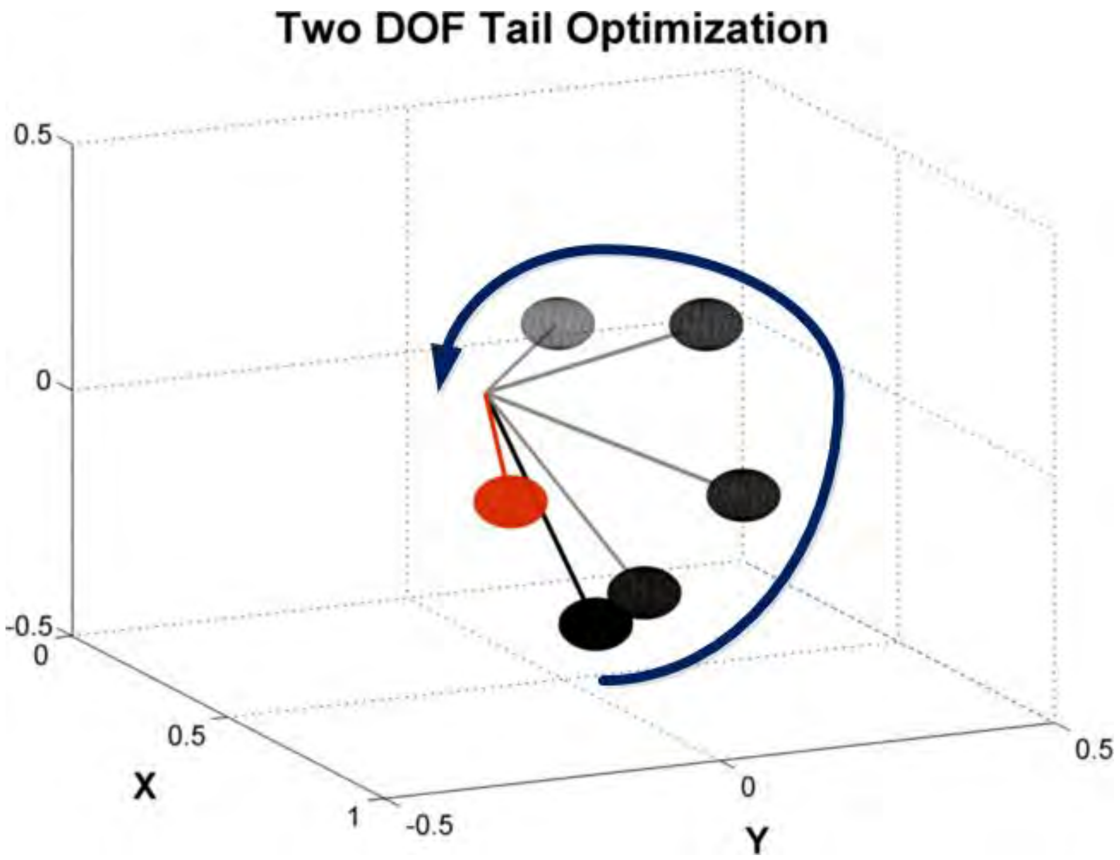

Figure 4.7: Animation screenshots of the optimal tail trajectories for the first 0.2s. It is evident that the tail is moving in a cone shape. The black plot is the initial position and the red plot is the terminal position.

## 4.2 Robot Design

### 4.2.1 *Tail Design*

In the previous section it was demonstrated that the motion of the tail in a cone can be generated by two actuators. Thus, the experimental testing of this motion will require a tail actuator with two motors.

The only other two degree of freedom tailed robot (to the Author's knowledge) is the Two DOF Tailbot developed by Chang-Siu et al. [47]. However, this design suffers from the disadvantage that one motor will need to actuate the inertia of the tail plus the second motor. This is undesirable for this application, as it would require a larger motor which would considerably increase the weight of the system.

An alternative design was proposed; inspired by a differential gear of the motorcar. However, instead of axels to the wheels being driven by the central bevel, these shafts are connected to the two motors and the middle bevel is driven. This means that neither motor will need to carry the weight of the other and the only inertia will be that of the tail. The concept is depicted in Figure 4.8. Also, the bevel gears ($G_1$,$G_2$,$G_3$) are mounted on a plate which is allowed to pivot on bearings with respect to the main platform (the robot chassis).

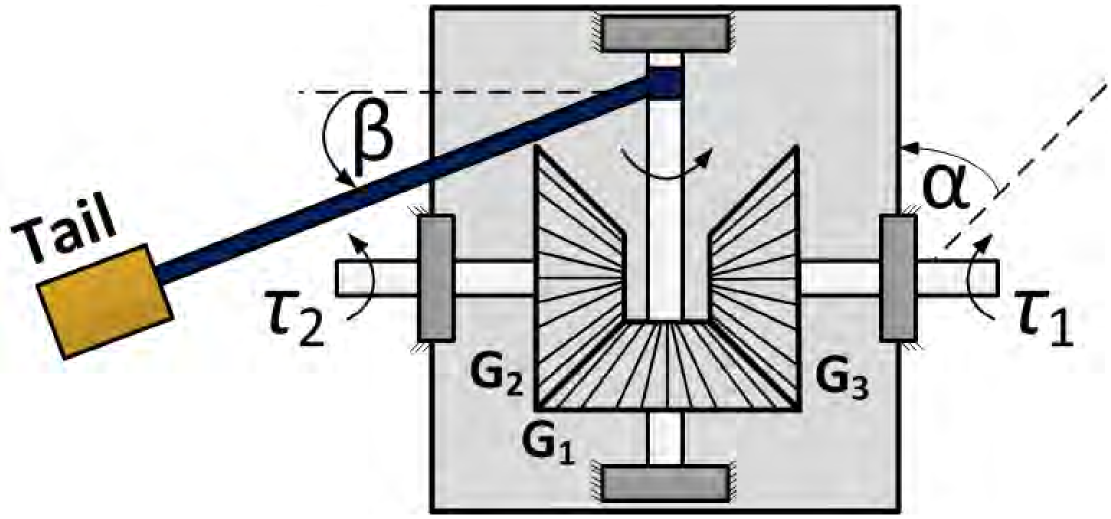

Figure 4.8: Schematic for the two degree of freedom tail. The design was inspired by the differential gear mechanism in a motorcar.

This novel mechanism results in an interesting mixing from input motor torques to the Euler Angles of the tail as the two motors are coupled by the kinematic relationship:

$$\begin{bmatrix}\dot{\alpha}\\ \dot{\beta}\end{bmatrix} = \begin{bmatrix}0.5 & -0.5\\ -0.5 & -0.5\end{bmatrix}\begin{bmatrix}\omega_1\\ \omega_2\end{bmatrix}, \tag{4.14}$$

where, $\omega_1$, $\omega_2$ represent the motor velocities and $\dot{\alpha}$ and $\dot{\beta}$ respectively are the pitch rate of the plate and the roll rate of the tail with respect to the plate. It should be noted that relationship above is for a tail connected at the centre of rotation but as seen in Figure 4.8, there is an offset in the practical system to allow the tail to clear gears. This length (0.05 m) was negligible compared to the tail length (0.5 m) and as such was ignored.

For the tail motors themselves, two Maxon EC-40 70W brushless motors were selected and the corresponding motor parameters are presented in Table 5. A gear ratio of 51:1 was selected to provide maximum angular impulse over 0.5 s. The system was modelled in Solidworks and a graphic rendering is depicted in Figure 4.9.

Table 5: Maxon EC-40 70W Motor parameters.

| Parameter | Value |
|---|---|
| Motor Nominal Voltage ($\boldsymbol{V}$) | 18 (V) |
| Motor torque constant ($\boldsymbol{K_{\varphi}}$) | 16.7 (mNm/A) |
| Motor Gear Ratio ( $\boldsymbol{N}$) | 51 |
| Motor terminal resistance ($\boldsymbol{R_T}$) | 0.367 (Ω) |
| No load speed ($\boldsymbol{\omega_0}$) | 10100 (rpm) |

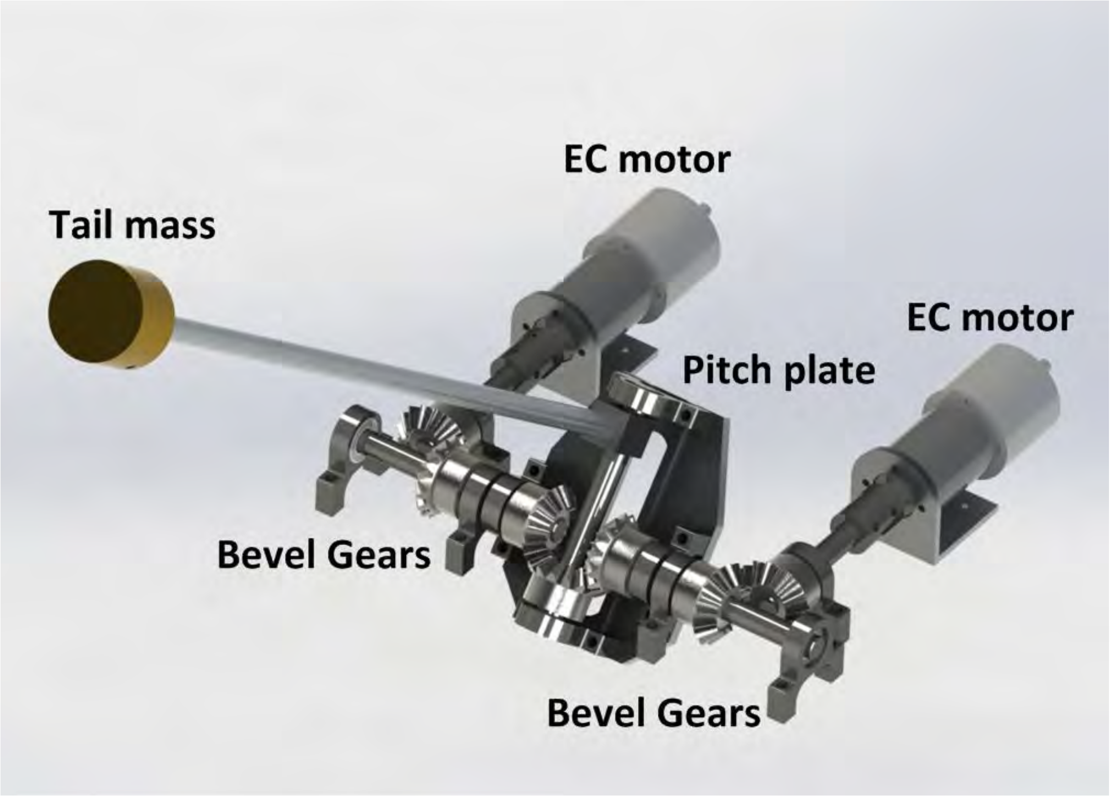

Figure 4.9: Mechanism for the two DOF tail modelled in Solidworks. The tail is capable of rolling relative to the pitch plate, and the pitch plate can rotate relative to the base.

### *4.2.2 Robot design*

The original *Dima I* robot described in Chapters 2 and 3 was modified to accommodate the new tail design. This system became known as *Dima II*.

An entirely new base plate was designed and manufactured to make provision for the new tail mechanism. Furthermore, a Novak 550 Brushless motor replaced the previous car motor, to accommodate the additional weight introduced. Once more, the system in its entirety was modelled in Solidworks and the render is shown in Figure 4.10.

Figure 4.10: A render of *Dima II*. Note the two degree of freedom tail and associated motor actuation.

It should be noted that the tail pitch angle was limited to be within:

$$45° \leq \alpha \leq 115° \tag{4.15}$$

The upper limit was due to the tail colliding with the ground and the lower limit was a result of the roll cage placement.

With regards to the hardware design, the Maxon EC-40 motors were controlled by two Maxon ESCON 50/5 controllers via a PWM interface. A new circuit board was then designed to accommodate these, which contained the same processor (STM32F4) as in *Dima I*.

Additionally, the Tellumat SP1000GA had to be returned as it was on loan. Consequently, an Inertial Navigation System (INS) was implemented based on an Invensense MPU-9150 and UBlox Lea -6 GPS. These sensors were fused by an Extended Kalman Filter for position and attitude estimates at 50Hz. For more details on the INS design the reader is encouraged to view the corresponding report [77].

## 4.3 Feedback Controller Design

Inspection of the trajectories produced by the optimization, illustrate that the tail moves in a cone. In fact, when the tail is being actuated in this manner, the body perceives it as being a point mass rotating in a circle of projected radius, ρ. Where:

$$\rho = L_t sin(\gamma) \tag{4.16}$$

This concept is depicted in Figure 4.11. It is inferred that the acceleration of this mass along this circle produces is the roll torque on the body.

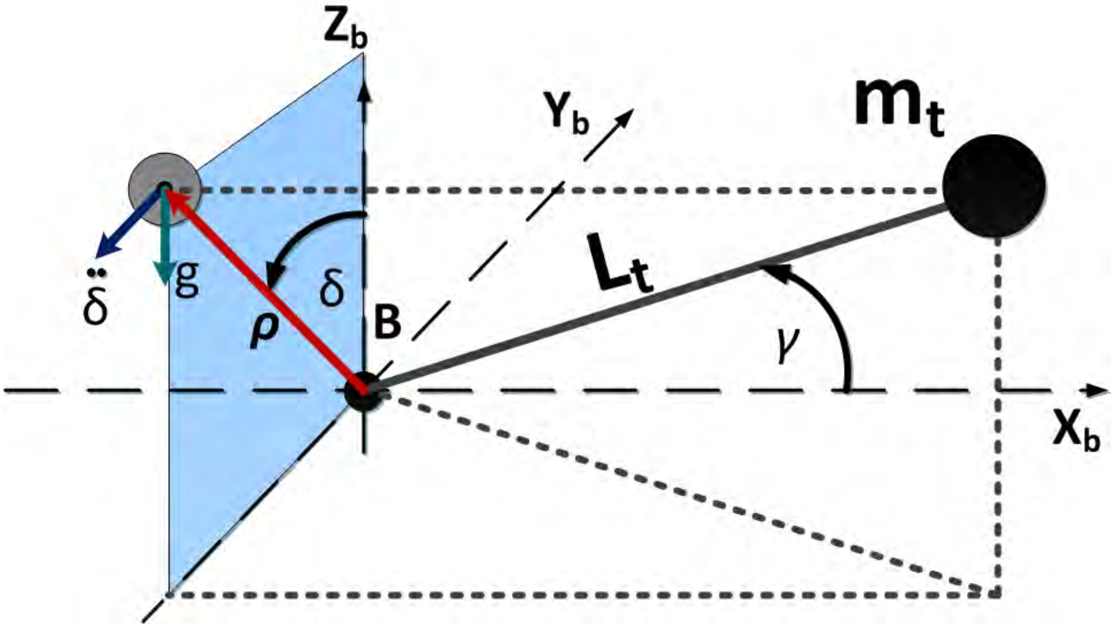

Figure 4.11: The concept of the cone motion to produce torque. The tail length $L_t$ is perceived by the body roll axis to be projected into the Y-Z plane and rotating along a circle.

Figure 4.11 also depicts the cone angles which are essentially spherical coordinates defining the rotation around the cone, $\delta$ and the width of the cone, $\gamma$.

Now that the comprehension has been established, the following control architecture for the two DOF tail is proposed:

- **Motor Angle Position controllers**: These will capture any unmodelled effects and attenuate disturbances at a high bandwidth.

- **Cone Torque Algorithm**: This algorithm will generate motor position trajectories based on the required torque on the body. This will also ensure the tail will move along a cone.

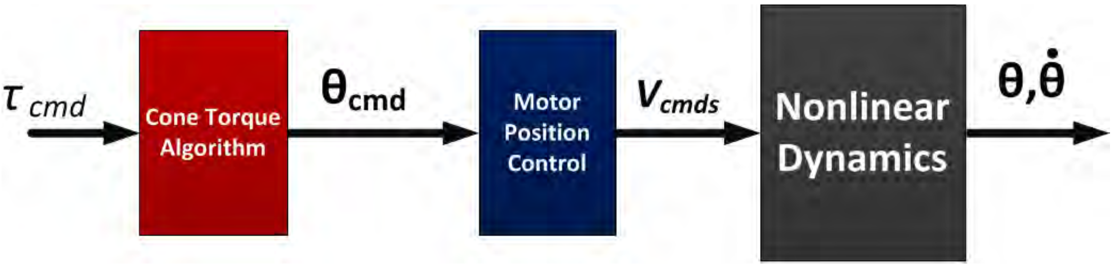

Figure 4.12: Proposed tail controller architecture.

### 4.3.1 *Motor Angle Position Controller*

To design the high bandwidth motor controllers, the standard servo motor control method was followed, where the controller consists of an inner loop speed controller which is commanded by a position controller. Moreover, to account for the nonlinear dynamics of the tail a feedback linearization was also performed. This concept is illustrated in the Figure 4.13.

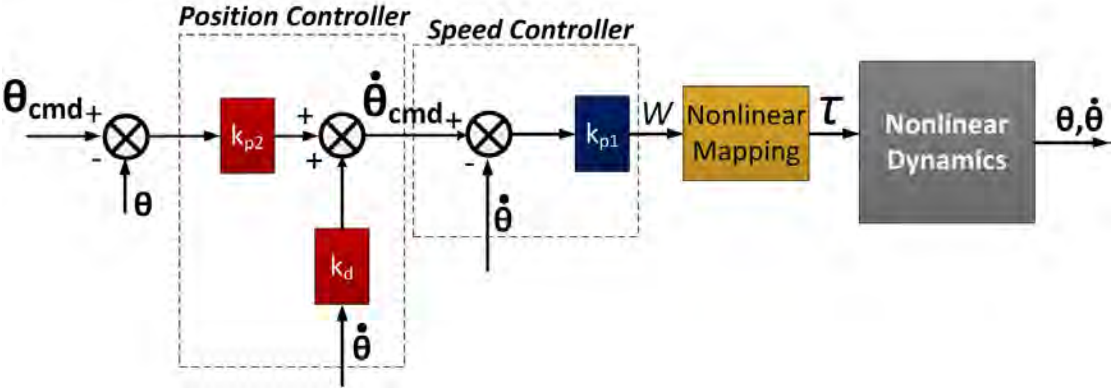

Figure 4.13: Servo control loop for the motor angles. The motor position controller is a PD controller which commands a speed controller. The speed controller then commands a pseudo input variable ‘w’ representing the motor accelerations. This variable is then mapped to individual motor torques.

To adequately design these controllers the first task was to modify the model developed in Section 4.1. In order to control the motor angles directly, the new generalised coordinates were:

$$\boldsymbol{q} = [\theta_1 \quad \theta_2]^T \tag{4.17}$$

In order to derive the new dynamics, the relationship mapping the motor velocities (and consequently the angles) shown in equation (4.14) was substituted into the position and velocity equations used to derive the model in Section 4.1. Note that the body roll angle has been removed from the dynamics.

Using this model, a full state feedback linearization [61] could be performed as the model was now fully actuated. Thus, a mapping was generated from a pseudo input $\boldsymbol{w}$ (representing the motor accelerations, $\ddot{\boldsymbol{q}}$) to the motor torques by:

$$\boldsymbol{\tau} = \boldsymbol{B}^{-1}(\boldsymbol{M}\ddot{\boldsymbol{q}} + \boldsymbol{C}\dot{\boldsymbol{q}} + \boldsymbol{G}) \tag{4.18}$$

where, all matrices are defined in Section 1.3. The input mapping $\boldsymbol{B}$ is simply the Identity Matrix now that the generalized coordinates have been changed. This torque command is then mapped to motor voltages by the relationship defined in equation (2.13). Subsequently, the speed controller could then be designed fairly trivially. A proportional controller was designed with a gain ($k_{p1}$) of 100.

Lastly, the motor position controller was designed as a PD controller. The proportional gain $k_{p2}$ and velocity gain $k_d$ were designed as 200 and -1.2 respectively. Additionally, the mapping from motor angles to Euler Angles for the tail is given by:

$$\begin{bmatrix} \theta_1 \\ \theta_2 \end{bmatrix} = \begin{bmatrix} 1 & -1 \\ -1 & -1 \end{bmatrix} \begin{bmatrix} \alpha \\ \beta \end{bmatrix} \tag{4.19}$$

Using this relationship, Euler angles can now be commanded. The model and controllers were implemented in Simulink and simulated. An example step response for is shown in Figure 4.14.

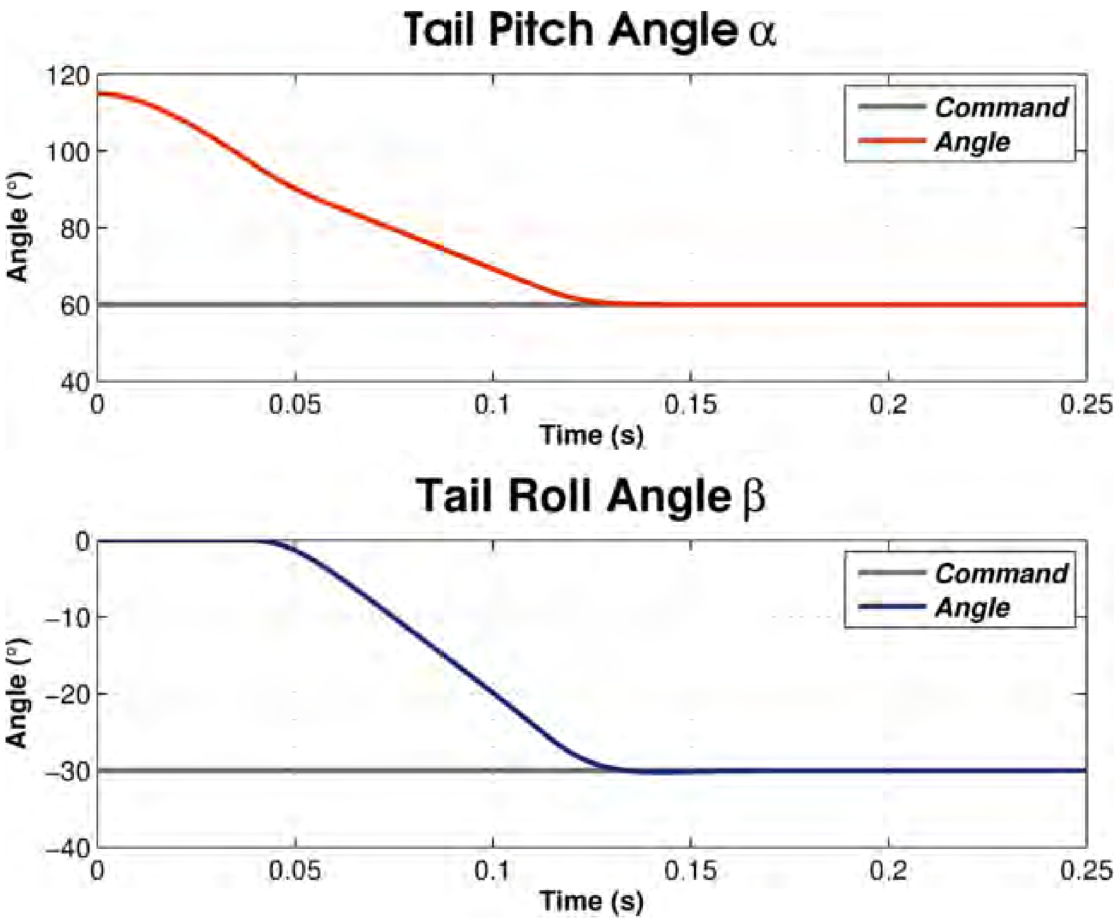

Figure 4.14: Euler Angle step responses for the motor angle controllers.

Now that the motor angle controllers have been effectively designed the next phase was to design the Cone Torque Algorithm.

### *4.3.2 Cone Torque Algorithm*

The next task was to develop an algorithm to map the required torque on the body to corresponding motor angle commands. The idea is to first map the torque command to a corresponding cone rotation angle $\delta_{cmd}$. Using this angle in conjunction with a required cone width angle $\gamma_{cmd}$, another mapping can convert the angles to corresponding motor angles commands. The proposed scheme is depicted in Figure 4.15.

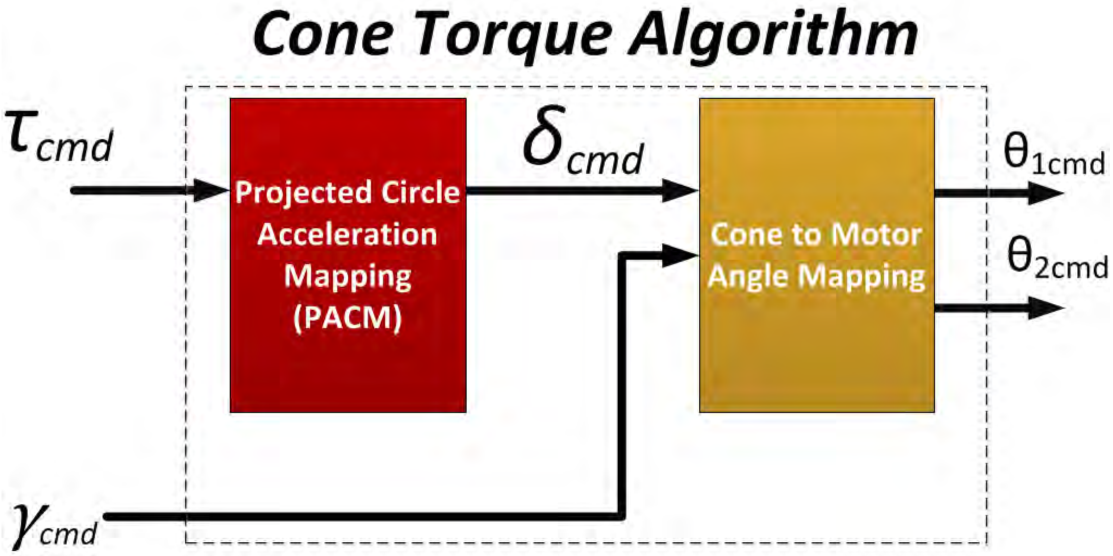

Figure 4.15: The Cone Torque Algorithm is depicted above. The algorithm consists of two parts. The first part maps the required torque to cone angle commands. The second part, maps these cone angle commands to motor angle commands to be sent to the position controllers.

To determine the required cone rotation angle, the rotation angle acceleration must first be determined. The reader should recall in Section 4.3.1 (Figure 4.11) the body roll axis was proposed to experience the tail cone motion as if the tail was rotating in a project circle in the Y-Z plane of the body. This projection is more clearly shown in the Figure 4.16.

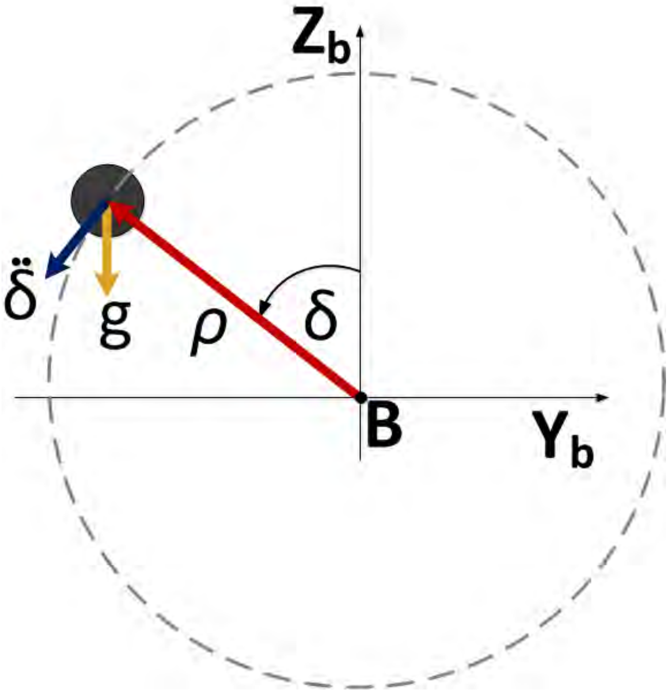

Figure 4.16: Projection of the cone motion in the body Y-Z plane. The body will perceive the tail mass to be moving in a circle if the cone width angle is kept constant.

Using Newton II, and assuming that the projected tail length $\rho$ remains constant, the acceleration required on the body will be provided by the following equation:

$$\ddot{\delta}_{cmd} = \frac{\tau_{cmd}}{m_t \rho^2} + \frac{g sin(\delta)}{\rho} \tag{4.20}$$

To translate this to a cone angle command, the acceleration can then simply be integrated twice. This equation requires the cone angles to be calculated. This can be done by using the geometry of Figure 4.11 and is shown to be:

$$\begin{bmatrix} \delta \\ \gamma \end{bmatrix} = \begin{bmatrix} \operatorname{atan}(\frac{0.5\left(cos(\theta_1) - cos(\theta_2)\right)}{\cos(\frac{\theta_1}{2} - \frac{\theta_2}{2})}) \\ \operatorname{acos}(0.5\left(cos(\theta_1) - cos(\theta_2)\right)) \end{bmatrix} \tag{4.21}$$

For the second part of the algorithm, the cone angle commands will need to be mapped to the corresponding motor angles. This is done by first converting these commanded cone angles to Euler Angles, which are then mapped to motor angles. This is provided by the following relationship:

$$\begin{bmatrix} \theta_1 \\ \theta_2 \end{bmatrix} = \begin{bmatrix} \operatorname{acos}(\cos(\frac{\gamma}{\sqrt{1 - \cos^2(\delta)\sin^2(\gamma)}})) \\ \operatorname{acos}(\cos(\delta)\sin(\gamma)) \end{bmatrix} \tag{4.22}$$

These angle commands will then be sent to the position controllers as setpoints.

### *4.3.3 Simulation Results*

The controller algorithms and the revised dynamic model were then implemented in Simulink and simulated using Matlab's ***ode45*** solver.

As discussed in Section 1.3, the templates of the robot and cheetah can only be compared in the stance phase. Hence the model will only be simulated where it needs to produce a non-zero torque on the body (unlike the flight phases which required zero torque).

Moreover, the design of the robot only allowed the tail to a maximum pitch angle of 115°. This translates to a cone width angle of 25°. Additionally, the manoeuvre time will be 0.5 s long and the reader may recall that this is longer than the 0.1 s performed during the optimization. But, with the anticipation of practical testing, the steering servo lag discussed in Section 2.3 limits the minimum duration of the turn.

The tail was initialized at a pitch angle of 115° and roll angle of 0°. The results for a 1Nm torque step are shown in Figure 4.17. It is evident that the controller tracks the commanded value adequately as the torque on the body is approximately within 80% of the commanded value even at the end.

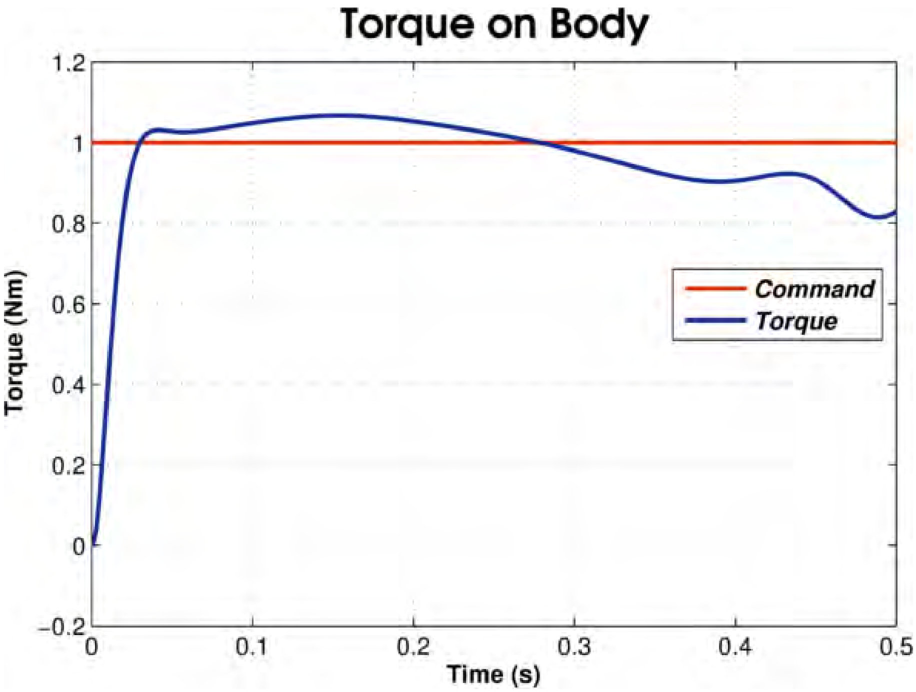

Figure 4.17: Simulation of 1Nm Step Command. It is evident that the controller stays within 80% of the commanded value.

The corresponding acceleration commands and measurements are shown at the top of Figure 4.18. Here it can be seen that the acceleration is being accurately tracked. At the bottom of the plot the resulting Euler Angles are seen, which align with the profile generated by the optimization in Section 4.1.3.

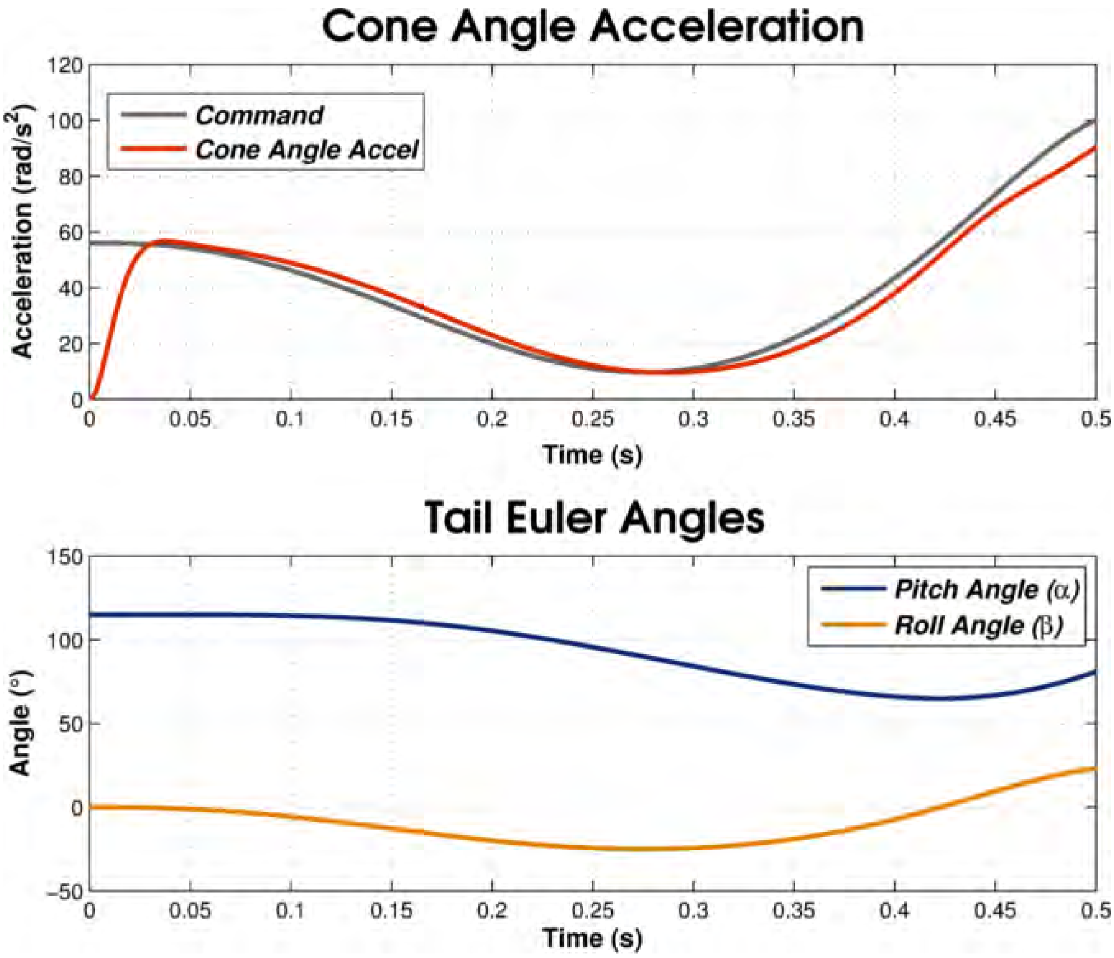

Figure 4.18: Top - Cone angle acceleration commanded by the Cone Torque Algorithm. It is evident that the controller is tracking adequately. Bottom - The resulting Euler Angles from the 1Nm Torque Step.

Greater torque commands were attempted; however these were not successful due to saturation of the voltage command. The issue is that when the tail moves with gravity, the acceleration command increases dramatically to generate a torque on the body. This can be seen after approximately 0.4s in Figure 4.18. This reason also explains why the torque on the body starts to drift from the command: As the controller commands more cone acceleration, the position controllers simply cannot react fast enough and the cone width angle starts becoming smaller.

## 4.4 Experiments

To determine experimentally if the cone motion of the tail could indeed produce a roll torque on the body testing was performed on *Dima II*. The controllers were coded in C and targeted to the microcontroller. The system was then tested on a field in a similar manner as Chapter 2. However, here the tail was used in an open loop manner with respect to the body roll (This was different to Chapter 2 where there was feedback from the body roll to the torque command). The inner loop position controllers were active to achieve the commanded tail movement.

The test procedure was thus as follows:

- The system was set to a certain throttle value and allowed to reach the steady state velocity.
- The steering was then stepped 30° and the tail was sent a command of 1Nm torque and a cone angle of 25°
- After 0.5s, the steering was commanded back to centre and the system was shutdown

This process was repeated until the system rolled over due to the centrifugal force. As in Chapter 2, the performance metric was the peak lateral acceleration rotated into the inertial frame which was derived from the IMU.

### 4.4.1 *Results*

The system without a tail achieved a maximum acceleration in all test runs of 6.7 ± 0.31 $m/s^2$ and this occurred at a velocity of approximately 6 m/s. Any turns initiated at velocities greater than this resulted in the robot toppling over.

The system with the tail achieved a maximum acceleration in all test runs of 11.3 ± 1.127 $m/s^2$ and this occurred at a velocity of approximately 7 m/s. The maximum lateral accelerations for both systems are depicted in the Figure 4.19. An example of the tail robot actuating the tail in cone can be seen in Figure 4.20. The reader is also encouraged to view the supplementary video material on the attached DVD.

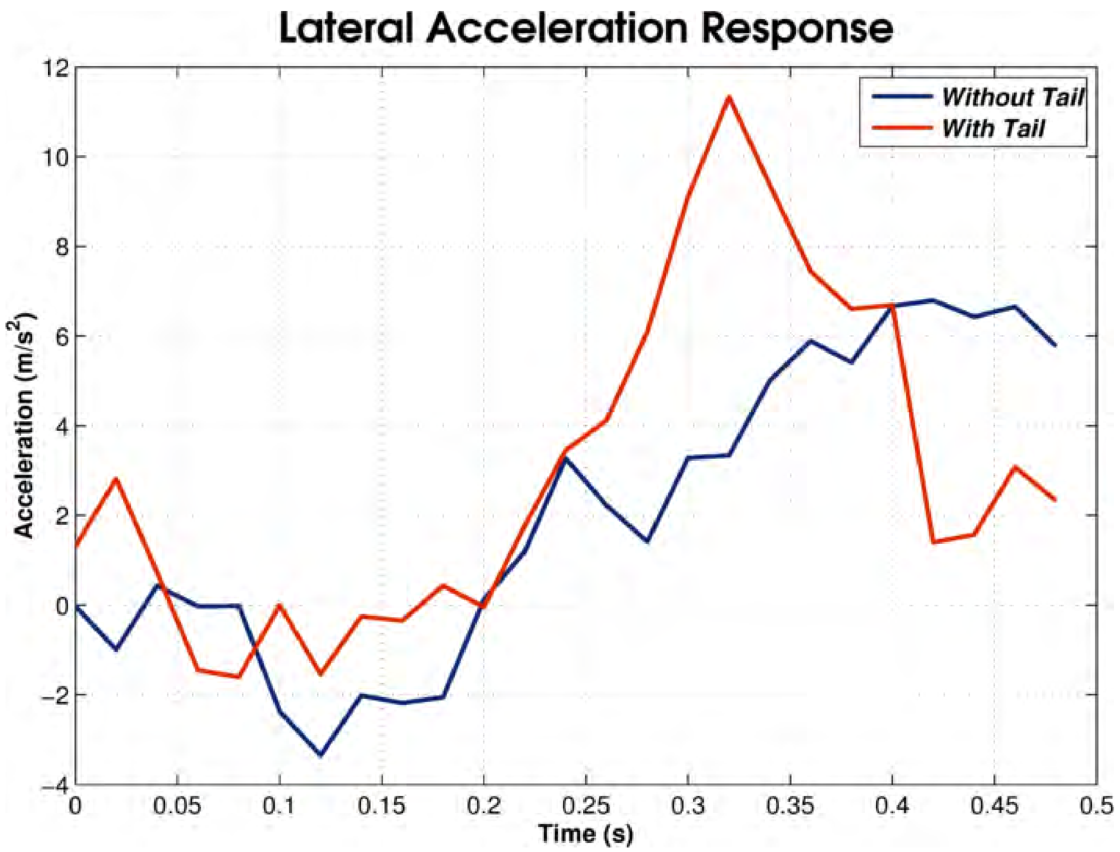

Figure 4.19: Lateral acceleration obtained for both systems. On average the tail-less system could only perform the turn at 6 m/s whereas the tailed system could initiate turns at 7 m/s.

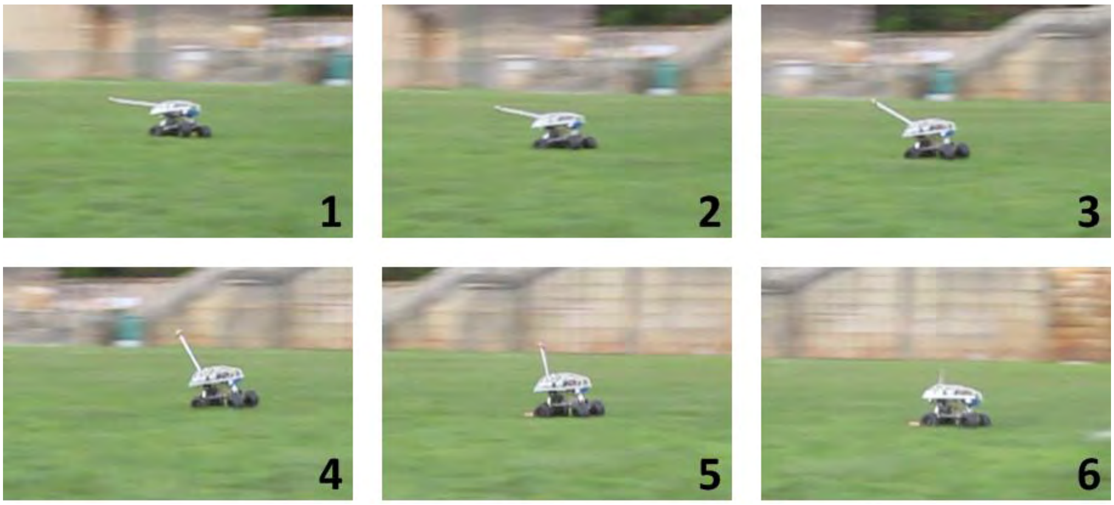

Figure 4.20: Snapshots of *Dima II* performing a turn at 7 m/s. Note that the tail is being actuated in a cone shape. Images are depicted at 100 ms intervals.

## 4.5 Discussion

The tailed robot was able to withstand approximately 70% more lateral acceleration than the tail-less robot. This demonstrates that the cone motion can indeed impart a roll torque on the body as expected.

Comparatively *Dima II* did not dramatically outperform *Dima I* with both systems producing approximately the same lateral accelerations. In fact, *Dima I* was able to initiate turns at velocities of 7.5 m/s, 0.5 m/s faster than *Dima II.* The difference can be attributed to the fact *Dima II* being commanded open loop torque trajectories, where as previously in Chapter 2 the tail formed part of a body roll rate controller.

However, the leading reason is the shallow cone width angle possible with the robot. If the trajectories produced by the optimizer in Section 4.1.3 are reflected on, it can be seen that in order to generate an 8 Nm torque on the body, the input torques to the tail reached peak values of 20 Nm. Thus, a significant portion of the available torque is used in accelerating the tail in directions that do not produce useful torque. This can be further understood from the projected circle argument presented in Section 4.3.1, where it was demonstrated that the body perceives the tail moving in a cone as a mass moving along a circle of radius, $\rho = Lsin(\gamma)$. It is evident that as the cone width decreases, the projected radius and as such the torque on the body gets smaller. Thus, the *Dima II* tail being constrained to have a 25° cone only results in a 0.21 m circle radius and as such reduced the body torque significantly. This is signified by the fact that to generate the 1 Nm torque for the experiments, the motors were applying inputs close to their maximum torque capability.

This however would not be a problem for the cheetah for two reasons. Firstly, in the videos of the cheetah performing the cone, it can be seen with cone widths of approximately 70° because of the tail position relative to the ground. Secondly, even when executing larger cone angles and striking the ground, the cheetah tail is compliant and as such could absorb any impacts efficiently.

The cheetah is also capable of a flight phase during its gallop and these dynamics the robot cannot capture.

Longer duration turns (greater than 0.5 s) were attempted with robot but were not successful as when the tail reaches the section of the cone where it needs to accelerate faster than gravity; the torque limits of the motors were reached. This was discussed in Section 4.3.3. It is natural to assume that the cheetah muscles would be capable of producing larger torques than that of an EC motor but in the next chapter another source of angular impulse will be investigated which the cheetah tail possesses: that of aerodynamic drag.

# Chapter 5

## Aerodynamics of the Cheetah Tail

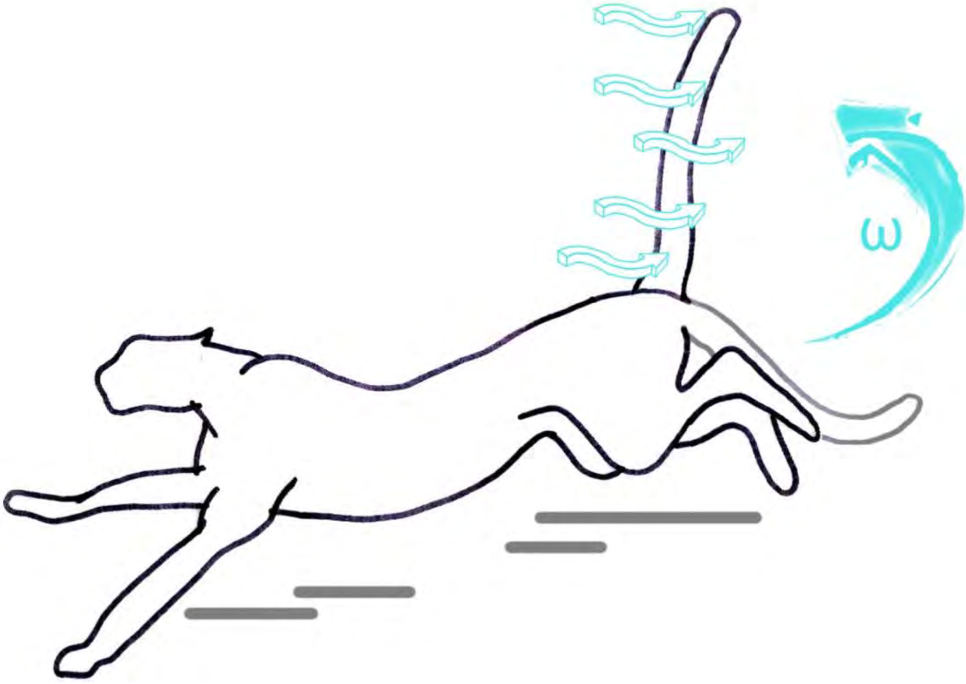

As highlighted in Chapter 1, the cheetah tail has often been described and thought of as “heavy”, “high inertia” and “muscular” in the public domain [4] [5] [6] as well as in the biological literature [7] [8]. It is under this assumption that the Author developed and tested various hypotheses i.e. that the cheetah tail motions only exert inertial torques on the body.

At the end of the research period, the Author was given the opportunity to measure the tail mass (and estimate inertia) during a routine cheetah necropsy. Here it was found that the tail was not as heavy as expected or assumed and its centre of mass is close to the base of the tail. This means that the inertia is also lower than expected. In fact, the apparent tail volume (see Figure 1.1) was not comprised of muscle, but was substantially furry. This observation leads to the hypothesis that the aerodynamic drag could possibly impart torque on the body during rapid manoeuvres as well. The tail fur was subsequently tested in a wind tunnel to determine its drag characteristics. Finally, mathematical models were developed to expand the understanding of the aerodynamics of the tail and its effect on the body where it was shown that these effects are indeed significant.

The Author would like to acknowledge the work of Ms. Leeann Louis, Dr. Emily Lane, Mr. Callen Fisher and Prof. Ed Boje, co-authors of the publication [68] which forms significant parts of this chapter. Although much of the work was done collaboratively, where possible their particular contributions will specifically be stated in the proceeding sections.

## 5.1 Tail Inertia Estimation

At the time of starting this research, to the Author’s knowledge, no measurement for the cheetah inertia had been performed. However, near the culmination of this work, the thesis by Hudson [16] became available to the Author through private correspondence. This thesis contained inertia measurements but no consideration of aerodynamic effects of the cheetah tail as tabulated in Table 7.

### *5.1.1 Background*

The cheetah tail is a complex organ that is approximately 76.7 cm (±5.17 cm) long from the base to the tip of the tail [73]. It consists of lumbar vertebra number 7 (L7), the caudal most vertebrae which is attached to the pelvis, three fused sacral vertebrae (S1, S2 and S3) and the caudal vertebrae [78] as depicted in Figure 5.1. Generally these are 26 in number, but can vary between felines of the same species [79]. The tail is actuated by six major muscles as shown in the Figure 5.2 and described in Table 6. While the lumbar vertebrae and sacrum (S1-S3) are all relevant in actuation of the tail, only the caudal vertebrae are able to produce a torque outside of the cheetah body: therefore the focus will be on measuring these.

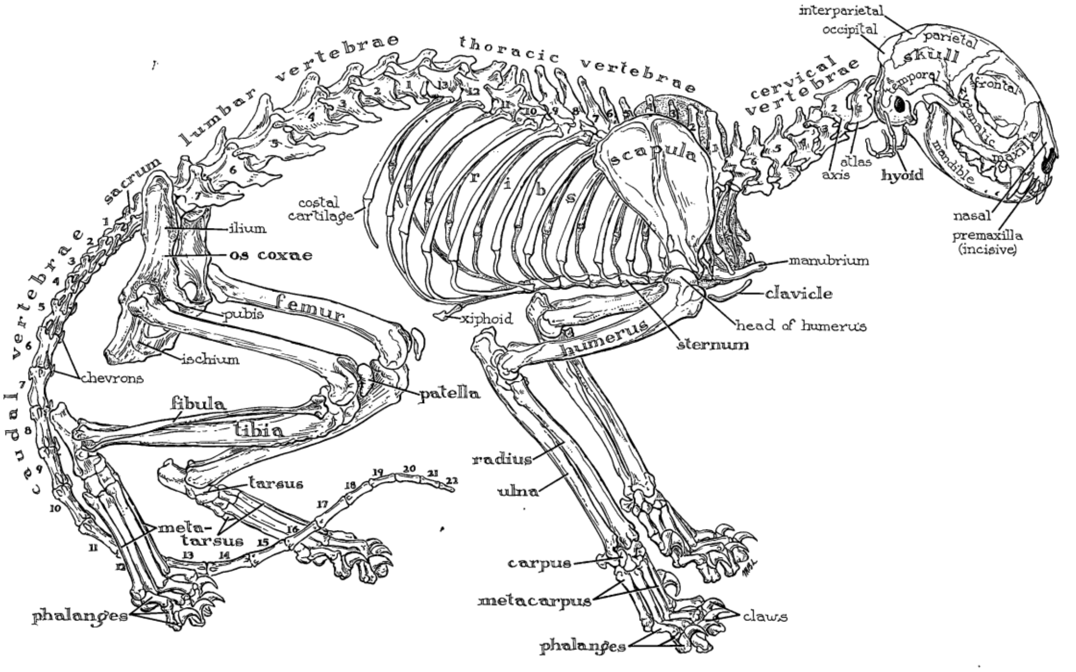

Figure 5.1: Skeletal system of the cat [79]

Table 6: List of six major muscles that actuate the cheetah tail and their functions

| Muscle | Function |
|---|---|
| M. sarcocaudalis dorsalis medialis | Extend or raise tail |
| M. sarcocaudalis dorsalis lateralis | Extend or raise tail |
| M. coccygeus lateralis | Bends the tail sideways |
| M. coccygeus medialis | Bends the tail sideways |
| M. sarcocaudalis ventralis medialis | Flexes tail |
| M. sarcocaudalis ventralis lateralis | Flexes tail |

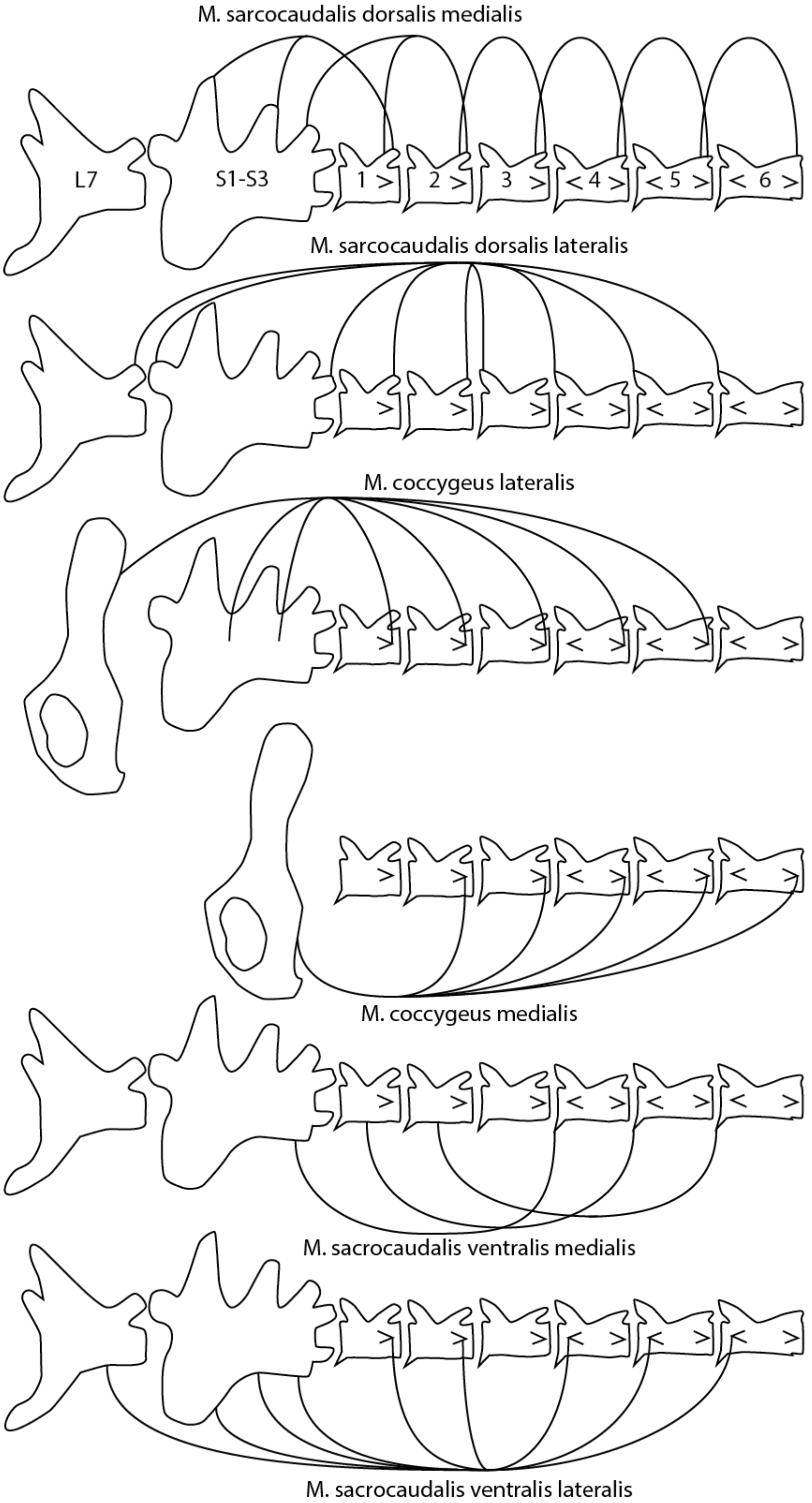

Figure 5.2: Simplified image showing 6 major muscles that actuate the tail with their origins and insertion points. Image by Leeann Louis via private correspondence.

### 5.1.2 *Moment of Inertia Modelling*

A routine cheetah necropsy was performed by Dr. Emily Lane (BVSc, Mhil, MRCVS) and measurements were done by the Author at the National Zoological Gardens (Pretoria, South Africa). The cheetah was a 12 year old male, who had been euthanized due to renal disease and was otherwise regarded as anatomically normal by the expert vet. The total body mass of the cheetah was 27 kg which was typical when compared to the data of Hudson [16] where the mass was 33.1 kg (± 7.14 kg).

The experimental protocol for dissection was developed by Leeann Louis specifically to determine the tail moment of inertia (see supplementary material on DVD). As per the protocol, the cheetah tail was removed from the body at the base of the tail. The base of the tail is defined as the intervertebral (IV) disc between S3 and C1. It was also skinned to remove the fur. This is depicted Figure 5.3 below:

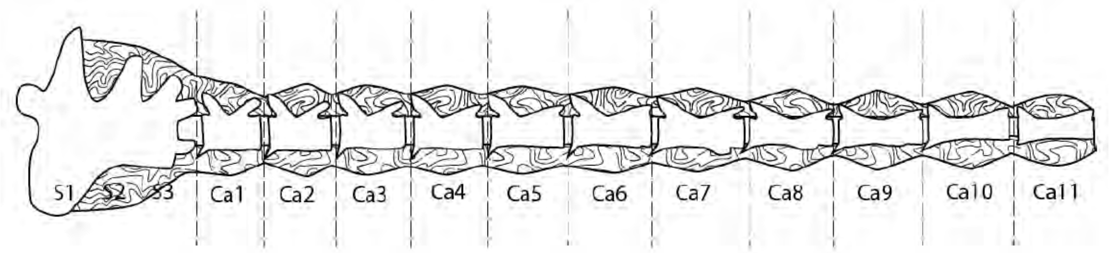

Figure 5.3: Lateral view of the sacrum and first 11 caudal vertebrae showing surrounding muscle and intervertebral (IV) discs between vertebrae. Image by Leeann Louis via private correspondence.

The cheetah tail length was 74 cm and the body length (base of shoulders to base of tail) was measured to be 77.5 cm. The tail mass (without the fur) was measured to be 519.5 g and the fur with skin weighed 162 g. The particular cheetah tail consisted of 21 caudal vertebrae.

It was noted once the cheetah tail was skinned that its effective diameter had significantly reduced. It was also found that the tail itself did not contain a substantial muscle mass and mostly comprised of tendons and vertebrae. Most of the muscle mass was at the base of the tail. This is evident in Figure 5.4.

Figure 5.4: The tail with the fur is seen on the left. Once the tail was skinned (right), it is clear that the diameter was reduced significantly. It is also noted that the tail consists mostly of thick tendons.

To determine the tail inertia and centre of mass, the caudal vertebrae were individually measured. This method has been employed for dinosaur appendage inertia estimation [80]. Each caudal vertebra was modelled as a cylinder, with moment of inertia about the centre of mass of the n-th vertebrae provided by:

$$I_{n,COM} = \frac{m_n L_n^2}{12} \tag{5.1}$$

where, $m_n$ is the vertebra mass and $L_n$ is its length. It was assumed that each vertebra is of uniform density.

To determine the moment of inertia about the tail base, Steiner's Theorem (Parallel Axis) can be used. This can be computed by:

$$I_{Tail} = \sum_{n=1}^{p} I_{n,COM} + m_n d_n^2 \tag{5.2}$$

where, $p$ is the number of caudal vertebra and $d_n$ is the distance from the n-th vertebra centre of mass.

A Matlab script was written to perform the calculation and the MOI about the base of the tail was 0.0292 kg.m$^2$ and the COM position from the base of the tail was 0.1861m. The COM position was calculated using the standard MOI equation. Based on the measurements, the tail fur contributes to approximately 25% of the total tail mass. Thus, its inertial effect cannot be ignored. If it is assumed that the fur is uniform across the length of the tail, it can be approximated as a hollow cylinder of mass 162 g. The outer diameter of which is 0.03 m and inner diameter of 0.023 m. These were derived from the fact that the mean diameter of the tail was 0.03 m with the tail skin and fur being approximately 7 mm thick. By accounting for this inertia, the total tail inertia for the cheetah measured by the Author then becomes 0.0588 kgm$^2$.

As discussed previously, after the cheetah tail had been measured, the thesis by Hudson [16] became available to the Author. Hudson had measured the tails of 5 cheetah tails with Dr. Sandra Corr (collaborator on [68]). This was done by freezing the tails (with fur), and then using a pendulum method of MOI estimation [81]. Hudson's results are shown in Table 7 and align with those obtained in this thesis.

Table 7: Table of Hudson's Cheetah Tail Data [16]

| **Subject** | **Tail Mass (kg)** | **Tail Mass (%Body mass)** | **Tail Length (m)** | **COM distance from base (m)** | **MOI about base of tail (kg.m$^2$)** |
|---|---|---|---|---|---|
| **1** | 0.745 | 2.4 | 0.73 | 0.23 | 0.0634 |
| **2** | 0.736 | 2.49 | 0.72 | 0.16 | 0.0358 |
| **3** | 0.625 | 2.27 | 0.77 | 0.2 | 0.0420 |
| **4** | 0.622 | 1.94 | 0.77 | 0.22 | 0.0491 |
| **5** | 0.57 | 1.25 | 0.77 | 0.19 | 0.0346 |
| **Mean** | **0.66** | **2.07** | **0.75** | **0.2** | **0.0450** |
| **Standard Deviation** | ***0.08*** | ***0.5*** | ***0.02*** | ***0.03*** | ***0.012*** |

### *5.1.3 Discussion*

The cheetah tail generally appears to only be about 2% of the total body mass. This is an interesting result: as mentioned in previous chapters, the tail is often considered as being heavy in the literature and the public domain. Moreover, both these results and those of Hudson [16] have shown that the tail mass is mostly concentrated towards the base.

During the necropsy the Author noted that the actual diameter of the tail significantly reduced after it was skinned. This is evident in Figure 5.4. *This observation inspired a hypothesis that the cheetah fur could also be contributing to the angular impulse on the body through aerodynamic effects*. It was also observed that the tail tip contained significantly longer fur than the rest of the tail. In the forthcoming sections, the aerodynamic drag of the cheetah fur (including the tip) is investigated.

## 5.2 Wind Tunnel Testing

The drag force on a section of the tail is the result of movement of the tail relative to the air and is made up of form drag (due to the effect of the projected shape of the tail on the air flow around it) and friction drag (due to the shear stress caused by the effect of the surface moving through the air) [82]. For a bluff body like the tail, the form drag tends to dominate. The drag force follows Benoulli's principle fairly closely and is related to the square of the relative velocity of the tail through the air. This relative velocity is a vector sum of the longitudinal velocity, the rotational velocity and wind velocity. For incremental cross-sectional area, $dA$, the incremental force is [83]:

$$dF = \frac{1}{2} C_d \rho v^2 dA \tag{5.3}$$

where $C_d$ is the coefficient of drag, $\rho$ is the air density, $v$ is the relative fluid velocity. To normalise the effect of scale, the drag force is normalised and the resulting drag coefficient, $C_d$, is typically shown against the Reynolds number [82]:

$$Re = \frac{v \rho l}{\mu} \tag{5.4}$$

Where, $l$ is the characteristic length and $\mu$ is the dynamic viscosity. For this study, the characteristic length is the diameter of a cylinder.

The fur of the tail of the dissected cheetah discussed in the previous sub section was available for testing in a wind tunnel. Two tests were performed to determine the aerodynamic effects. Firstly, to investigate the form drag of the fur a "furry cylinder" test rig was developed. The second test involved the manufacturing of a morphometric wooden tail tip. This was used to investigate the effects of the tip fur as well as the fur drag at varying angle of attack.

The Author would like to acknowledge the work of Mr. Callen Fisher in performing the wind tunnel measurements.

### 5.2.1 *Furry Cylinder*

The drag force of a section of a cylinder normal to the air flow was measured over wind speeds up to 30 m/s using the set-up illustrated in Figure 5.5. This experiment seeks to emulate an infinite cylinder by eliminating end-effects such as vortices.

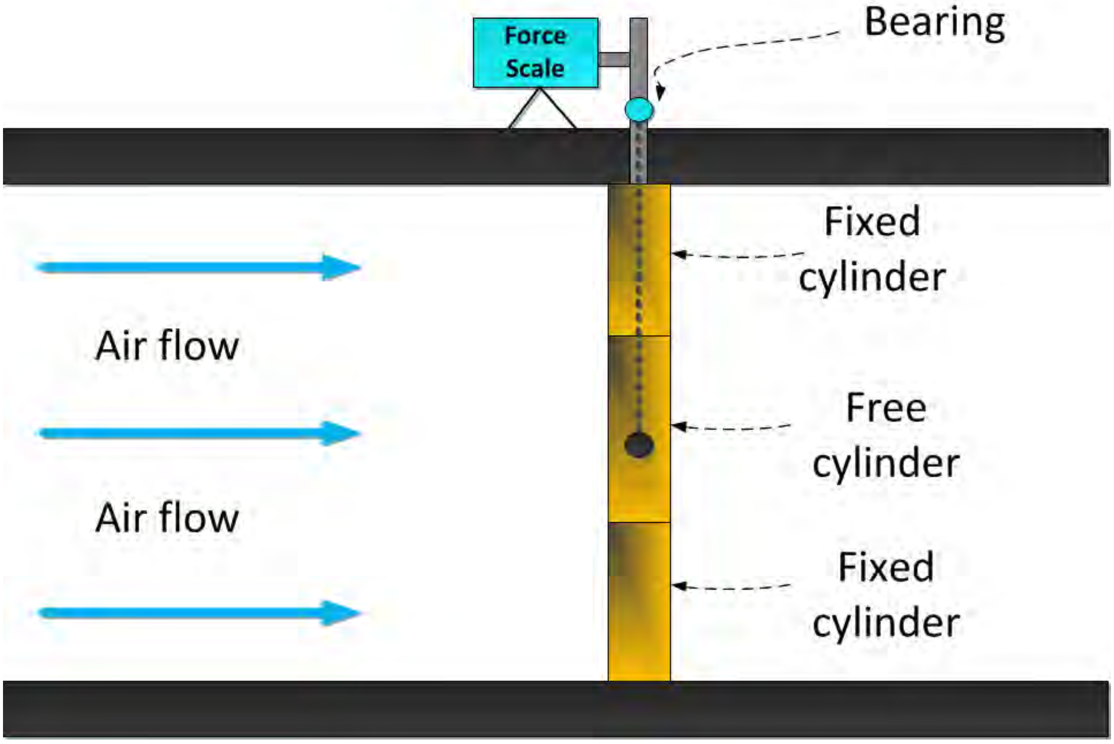

Figure 5.5: Furry cylinder test rig. The cylinder in the middle was allowed to rotate about the bearing while the two on the ends were fixed to the wind tunnel. This would allow edge effects to be ignored.

The test was first performed using a smooth (poly-vinyl-chloride) cylinder of 50 mm diameter. This was to calibrate the rig to known smooth cylinder data [84]. Then the test was repeated using the same cylinder, which was modified by gluing the cheetah pelt along the length of it. The diameter was measured by compressing the fur with Vernier callipers to get the diameter at the skin-fur interface (57 mm). The average length of the fur[7] from the middle of the tail was 12.33 mm (± 5.78 mm). Because the drag includes significant oscillations from vortex shedding, the average drag force over a cycle was used in the results.

---

[7] Ten random samples were taken from the cheetah pelt at the middle of the tail.

Using the force measurements, coefficients of drag were calculated at each velocity for the furry cylinder. Then by using known drag coefficient data for a smooth cylinder [84], the furry cylinder was compared by use of the Reynolds Number. In order for the graphs to align at the lowest speed (so that they can be compared), the furry cylinder diameter was scaled to give it an effective diameter. The resulting plot is shown in Figure 5.6 where the furry cylinder was scaled to 75 mm diameter. This implies an effective fur thickness of (75 mm – 57 mm )/2 = 9 mm. This value is less than the measured tail fur length of 12.33 mm.

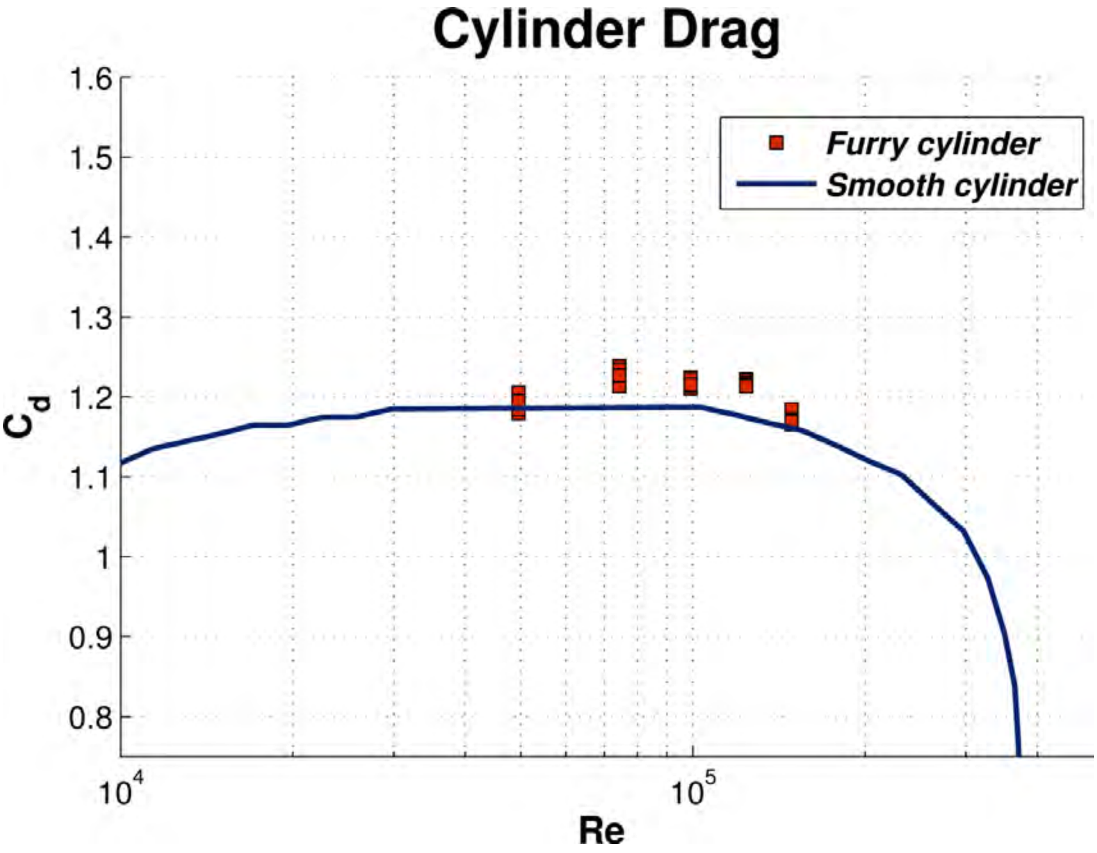

Figure 5.6: Coefficient of drag for the furry cylinder compared to a smooth cylinder. The furry cylinder was scaled up to an effective diameter of 75 mm.

The results of this test are twofold: Firstly, the furry cylinder appears to have the drag characteristics of an effective smooth cylinder with diameter comparable to the outer surface of the fur and not to the skin-fur interface. Secondly, it appears that the furry cylinder's drag coefficient remains fairly constant across the Reynolds numbers investigated.

### 5.2.2 *Morphometric Tail Tip*

Because the tip of the tail is very bushy and typically has the largest velocity and lever arm, there is reason to capture the drag effect of air-flow near the tip of the tail as accurately as possible. For this, a morphometric wooden model of 240 mm length was constructed based on measurements of the vertebrae described in Section 5.1. This was then covered with the pelt from the tip of the tail and the total (rather than per unit) forces were measured normal to the tail at various angles of inclination and wind speeds. The tail tip fur length was measured at random positions and was found to have an average length of 29.17 mm (±5.78 mm) which was longer than that of the rest of the tail. The test rig is shown in Figure 5.7, note that the forces on the exposed wooden section were calibrated out accordingly.

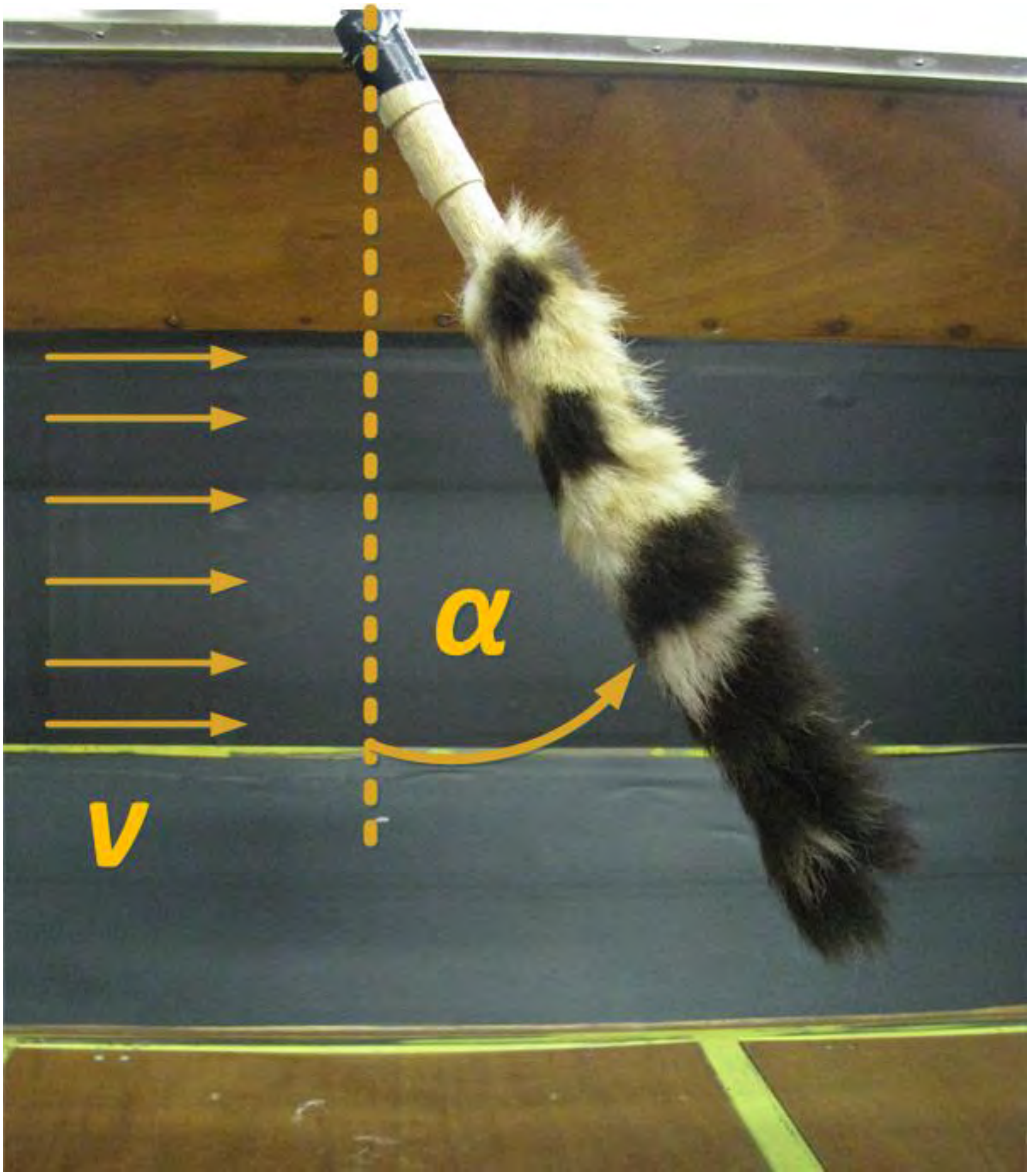

Figure 5.7: The tail tip wind tunnel test is shown. The rig allowed the tail model to be positioned at varying angles (α) relative to the air flow.

The coefficient of drag was initially determined using the projected cross sectional area[8] of the tail without the fur which was 0.0038 m$^2$. However, for comparison to the previous work on the furry cylinder, an effective area of 0.0145 m$^2$ was used to ensure that the datasets drag coefficient align at 10 m/s. The data is graphically shown in Figure 5.8 plotted against the angle with respect to the air flow. The drag coefficient was determined by:

$$C_d = \frac{Fcos(\alpha)}{0.5\rho v^2 A_{eff}} \tag{5.5}$$

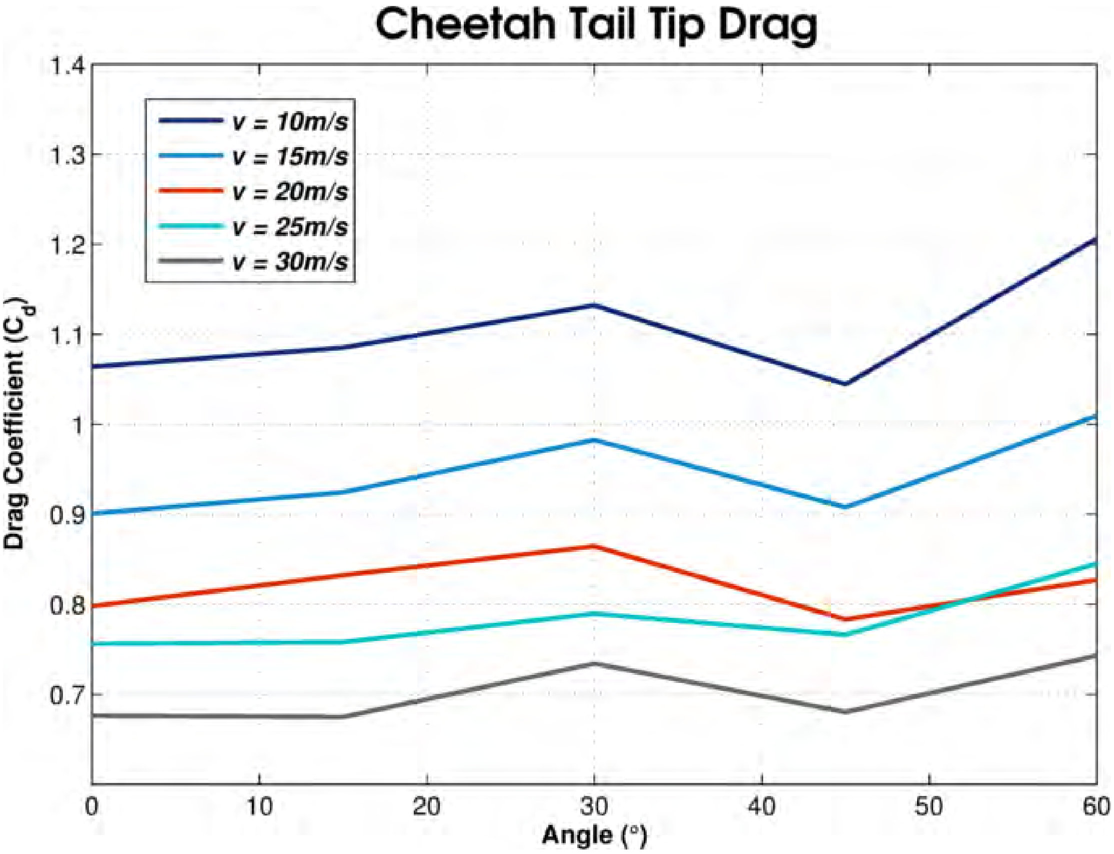

Figure 5.8: Cheetah tail tip drag data scaled to an area of 0.0145 m$^2$.

Evidently, there is a decreasing of $C_d$ at higher velocities. This can be attributed to the observed collapsing of the fur, which would thus reduce the effective cross-sectional area.

From the wind tunnel experiments it is evident that the tail is indeed capable of imparting aerodynamic forces. However, the specific effect on the cheetah body still remained uncertain. In the subsequent section this aerodynamic effect is modelled mathematically during various tail motions.

---

[8] Assuming the tail is has the cross sectional area of a trapezoid.

## 5.3 Mathematical Modelling

### 5.3.1 *Aerodynamic Force and Torque Model*

To adequately introduce the effect of the tail aerodynamics, a generalized force [56] was included in the Euler-Lagrange equations. Considering that the tail is attached to the body, the following diagram is produced shown in Figure 5.9 which illustrates the configuration.

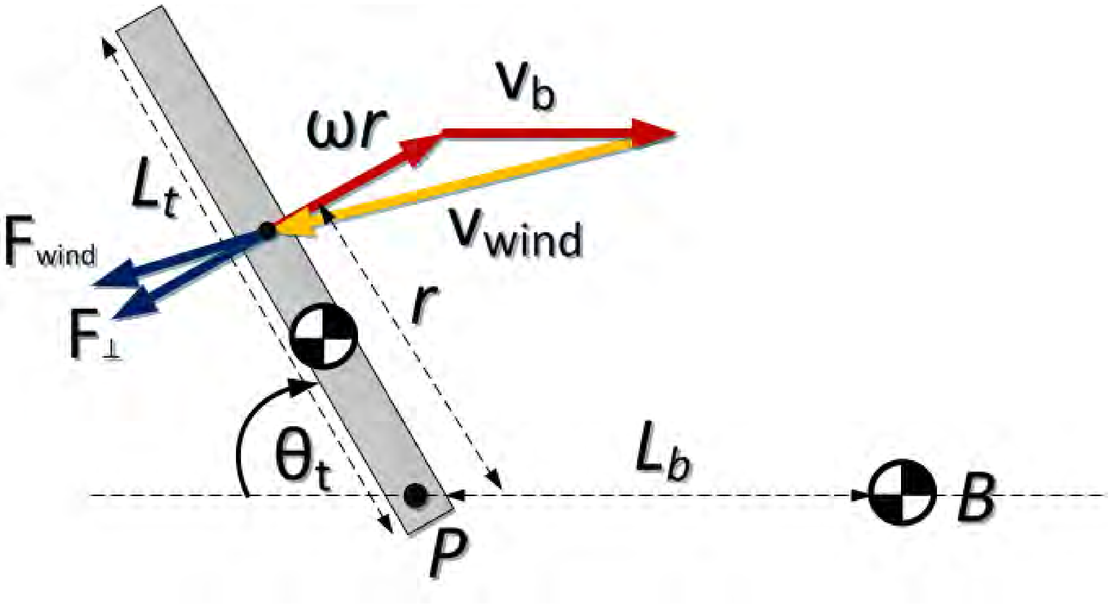

Figure 5.9: Diagram showing the incremental force on a point of distance 'r' from the attachment point of the tail.

Now, to calculate the torque at the point P from the aerodynamic drag, the incremental torque can be expressed as:

$$d\tau = \frac{1}{2}\rho C_d r v^2 D(r) dr \tag{5.6}$$

where, $D(r)$ is the width and $D(r)dr$ is the incremental area. To calculate the total torque produced, equation (5.6) can be integrated along the length of the tail $L_t$ using the diagram in Figure 5.9, resulting in:

$$\tau_d = \int_0^{L_t} \frac{1}{2}\rho C_d D(\omega r + v_b \sin(\theta_t))^2 r dr \tag{5.7}$$

After some simplification, this can be shown for a constant diameter tail to be:

$$\tau_d = \frac{1}{2}\rho C_d D\left(\frac{\omega^2 r^4}{4} + \frac{2\omega r^3 v_b \sin(\theta_t)}{3} + \frac{v_b^2 \sin^2(\theta_t)\, r^2}{2}\right) \tag{5.8}$$

A similar process is followed to determine the perpendicular force and it is shown to be:

$$F_d = \frac{1}{2}\rho C_d D\left(\frac{\omega^2 r^3}{3} + \frac{2\omega r^2 v_b \sin(\theta_t)}{2} + v_b^2 \sin^2(\theta_t)\, r\right) \tag{5.9}$$

### 5.3.2 *Angular Impulse Modelling*

As a metric of performance, the angular impulse was employed as a measure of the tail effectiveness during the manoeuvre. The angular impulse is defined as:

$$J = \int_0^{t_f} \tau_{net}\, dt \tag{5.10}$$

Where $\tau_{net}$ is the net torque on the centre of mass of the body and $t_f$ is the manoeuvre time. Three tail motions were investigated and simulated. These were:

- Motion in the pitch axis
- Motion in the roll axis
- Motion in the yaw axis

The motion in the yaw axis was not specifically investigated up until now for the reason stipulated in Section 1.1. However, with the addition of the aerodynamic effects, it could enlighten the general public view of the tail being employed as a "rudder" by the cheetah.

To model these motions mathematically, the tail was analysed as a rigid beam using the Euler-Lagrange equations. This tail was modelled as pivoting about some point attached a distance $L_b$ from the body COM (see Figure 5.9) and actuated by an input torque. Then, to obtain the torque on the body in the relevant axis, a redundant coordinate for the body rotation ($\theta_b$) was introduced and then constrained. This results in two generalized coordinates, $\boldsymbol{q} = [\theta_b, \theta_t]^T$. As was stated in previous chapters, this constraint torque is essentially the net reaction torque on the body. This can then be used to obtain the angular impulse.

To obtain the aerodynamic force effects on the generalized coordinates, it can first be assumed that the aerodynamic force can be reduced to a point force, acting at some distance $L_d$ from the pivot point (base of the tail). The aerodynamic force is then shown to be:

$$\boldsymbol{F_1} = \begin{bmatrix} -F_d \sin(\theta_b + \theta_t) \\ -F_d \cos(\theta_b + \theta_t) \end{bmatrix} \tag{5.11}$$

This force acts at a position:

$$\boldsymbol{r_1} = \begin{bmatrix} -L_b\cos(\theta_b) - L_d cos(\theta_b + \theta_t) \\ L_b\sin(\theta_b) + L_d sin(\theta_b + \theta_t) \end{bmatrix} \tag{5.12}$$

Then by using equation (1.5) the effect on the generalised coordinates is given by:

$$\boldsymbol{Q_d} = \begin{bmatrix} Q_{\theta_b} \\ Q_{\theta_t} \end{bmatrix} = \begin{bmatrix} -F_d L_d - F_d L_b \cos(\theta_t) \\ -F_d L_d \end{bmatrix} \tag{5.13}$$

However, it should be noted that the point $L_d$ will not be constant during the swing as the velocity will vary. But it is evident that $F_d L_d$ is in fact the torque produced at the contact point, which can be obtained from equation (5.7). Then in a similar manner, $F_d$ can be integrated and obtained for each time step using equation (5.9).

The reader will note however, that the drag coefficient will change as a function of the velocity and angle to the flow (angle of attack). Thus, it was proposed that at each time step, the tail is split into ten sections with each section have a constant drag coefficient and angle of attack. To total torque produced from the tail is then:

$$\tau_d = \sum_{x=1}^{10} \tau_x - \tau_{x-1} \tag{5.14}$$

At each summation the torque $\tau_x$and $\tau_{x-1}$ is calculated at section $x$'s coefficient of drag and angle of attack. A similar process was then performed for the total force.

In order to limit the performance to realistic cheetah tail input torques, a very simple model was developed. The model consisted of a simple peak power calculation.

$$\tau_{in} = \begin{cases} \tau_{cmd}, & \omega \leq \dfrac{P_{max}}{\tau_{cmd}} \\ \dfrac{P_{max}}{\omega}, & otherwise \end{cases} \tag{5.15}$$

The first case represents when the tail muscles are torque limited because of maximum fibre stress, the other case is where the muscles are power limited. Based on discussions in [2], the cheetah muscle has a power capacity of around 240 W/kg[9]. But the tail is actuated by approximately 600 g of muscle [16], producing a $P_{max}$ = 144W. The torque limit was derived from video observations where on occasion the cheetah tail was swung to approximately 34 rad/s in 90°. Now, given the mean inertia of tail, the torque limit was calculated to be approximately 20 Nm.

---

[9] It has been suggested in a study by West [90] that the cheetah muscle possibly has a power capacity of 600 W/kg.

The models were then implemented in Matlab and simulated at various forward velocities and the angular impulses. These results were compared to results for a tail without aerodynamic drag. The tail was stepped to its maximum torque value and the simulation terminated when the tail reached 90°. The parameters for the model were those of the cheetah tail model described in Section 5.1

The results for these simulations are shown in Figure 5.10. It is evident that the aerodynamics greatly increases the angular impulse, particularly as the forward velocity of the body increases.

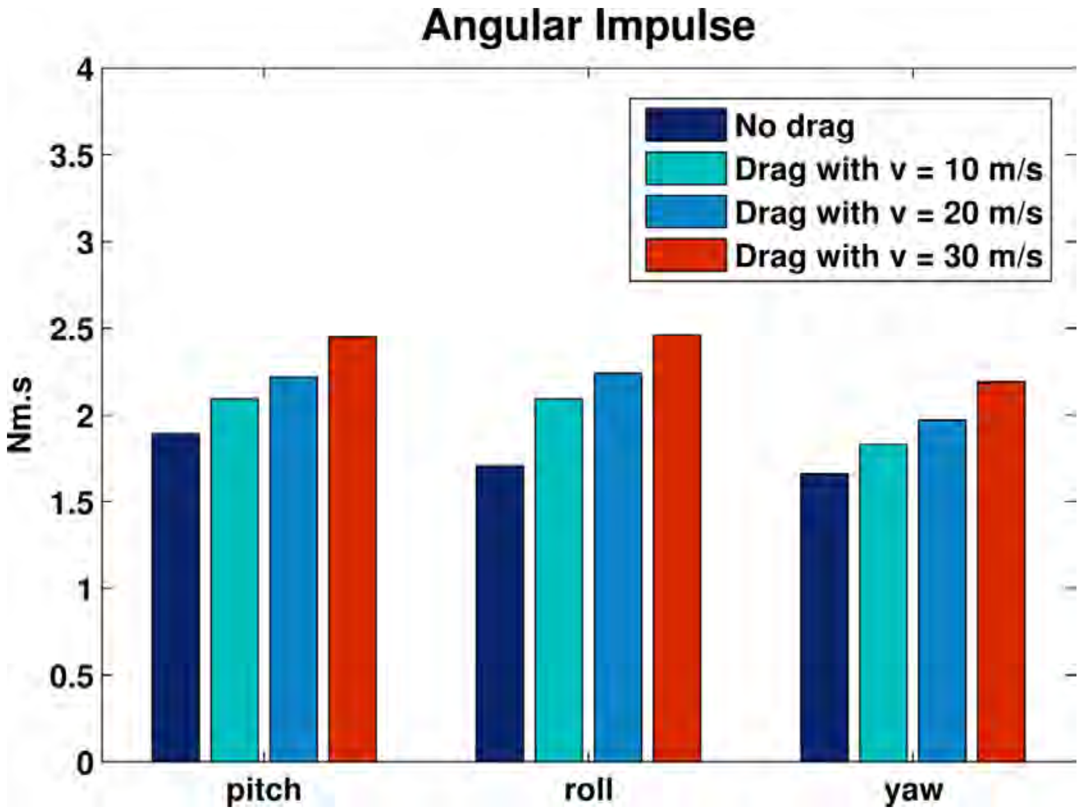

Figure 5.10: Angular impulse during various manoeuvres. The aerodynamics greatly affects the yaw and pitch especially when the body is moving at a forward velocity.

### 5.3.3 *Revised Braking Model*

A more detailed model for the cheetah braking was developed to understand its effects specifically on the loading of the legs. Wilson et al [2] suggests that the rapid deceleration could unload the hindquarters and induce a yaw instability or as discussed in Chapter 2 it could also cause a pitch instability. Moreover, the aerodynamics of the tail could possibly also be assisting deceleration, much like an airbrake in aeroplane or a sports car.

The model of the system is shown in Figure 5.11. The difference between the revised model and that of the LMT model described in Chapter 3 is firstly, the addition of aerodynamic forces on the tail. Furthermore, to calculate the hind and foreleg loading (normal forces), the positions $y_1$ and $y_2$ will be constrained to zero. This will ensure that the appropriate constraint forces are produced and as such the loading on the legs.

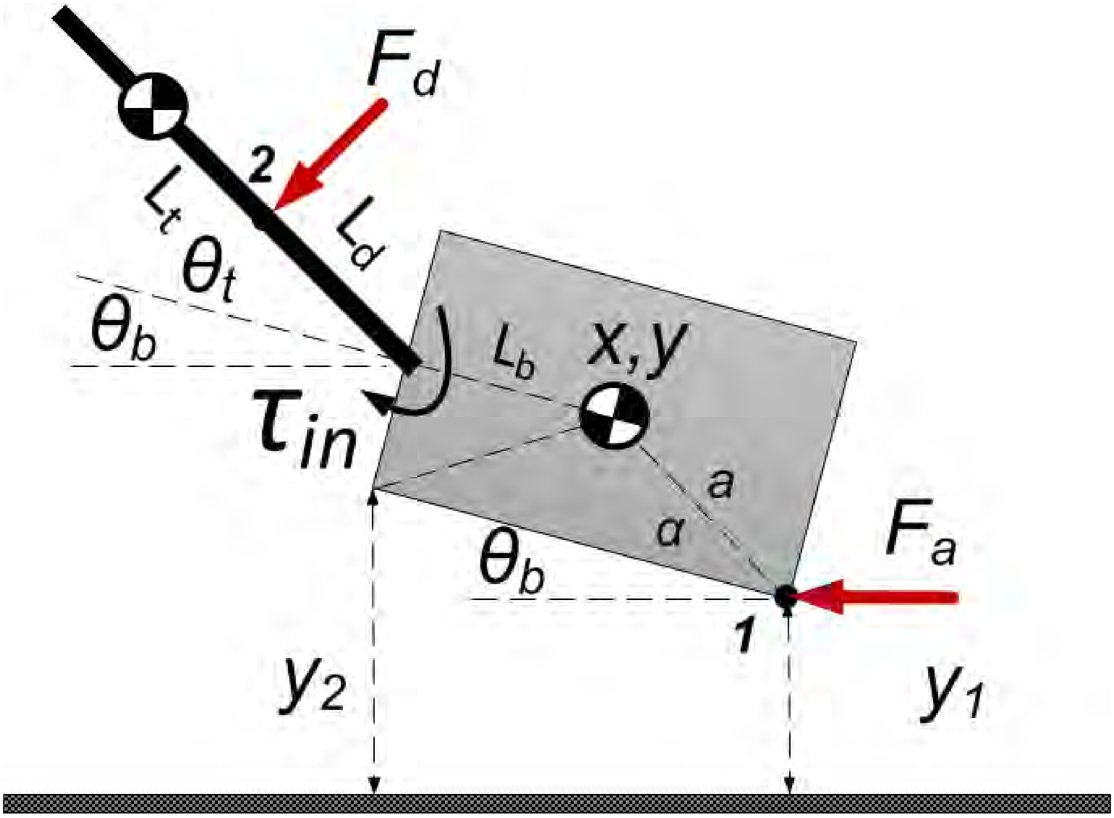

Figure 5.11: Braking model with aerodynamic effects on the tail and front and hind leg loading.

To calculate the loading, the $y_1$ and the $\theta_b$ coordinates can be constrained to be zero. The constraint Jacobian is given by:

$$\boldsymbol{A} = \begin{bmatrix} 0 & 1 & -a\cos(\theta_b + \alpha) & 0 \\ 0 & 0 & 1 & 0 \end{bmatrix} \tag{5.16}$$

Where the generalized coordinate vector is $\boldsymbol{q} = [x \quad y \quad \theta_b \quad \theta_t]^T$. The input tail torque and deceleration force can be included in a similar manner to the LMT model described in Chapter 3 and Section 5.3.2. Thus, the generalized vector is shown as:

$$\boldsymbol{Q} = \begin{bmatrix} -F_d sin(\theta_b + \theta_t) \\ -F_d cos(\theta_b + \theta_t) \\ -F_d(L_d + L_b\cos(\theta_t)) \\ -F_d L_d \end{bmatrix} \tag{5.17}$$

and the input mapping matrix is:

$$\boldsymbol{B} = \begin{bmatrix} -1 & 0 \\ 0 & 0 \\ F_a a \, sin(\alpha + \theta_b) & 0 \\ 0 & 1 \end{bmatrix} \tag{5.18}$$

The dynamics can then be derived using the Euler-Lagrange method.

The aerodynamic forces and torques are calculated using the same models described in Section 5.3.2. The input tail torque is produced by the peak power model. The parameters for the cheetah body (COM position) are detailed in Table 3. The mass employed for the body was 30 kg.

The system was simulated in open loop started at initial velocity of 25 m/s and a constant braking force ($F_a$) of 244.8N was applied . Three configurations of the system were simulated:

- With the tail fixed at an angle of zero degrees
- With the tail applying an input torque of 20 Nm without the effects of air resistance
- With the tail applying an input torque of 20 Nm with the effects of air resistance

Note that the simulation was terminated when the tail reached an angle of 90°. The results for the loading on the legs are illustrated in Figure 5.12.

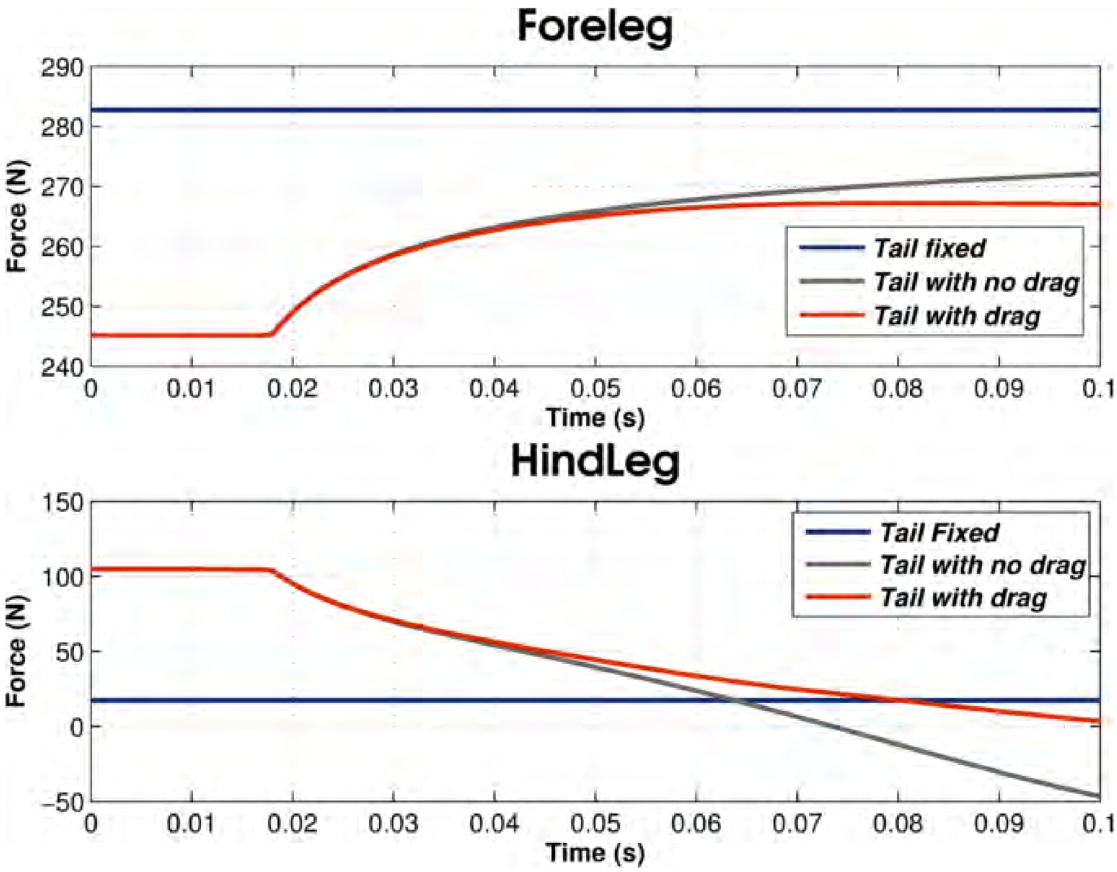

Figure 5.12: Leg loading simulations. It is clear that actuating the tail with aerodynamic forces included reduces the loading on the front legs and increases the loading on the hind legs.

It is clear from the simulations that the tail (in both configurations) increases the loading on the hind legs and decreases it on the front legs. However, by including the aerodynamic forces, the cheetah can sustain the distribution loading for longer than without drag. It is noted that the tail simulations (with and without drag) negatively load the legs towards the end of the stance. However, considering that this test was done completely in open loop, it is understandable and the general effect has been captured. With a feedback controller operating within the actuation limits, the cheetah will naturally be able to control this force more precisely.

The resulting velocity trajectories obtained in the configurations are shown at the top of Figure 5.13. The fixed tail configuration resulted in an average deceleration of 6.5 m/s$^2$. The tail with aerodynamics obtained a value of 7.5 m/s$^2$.

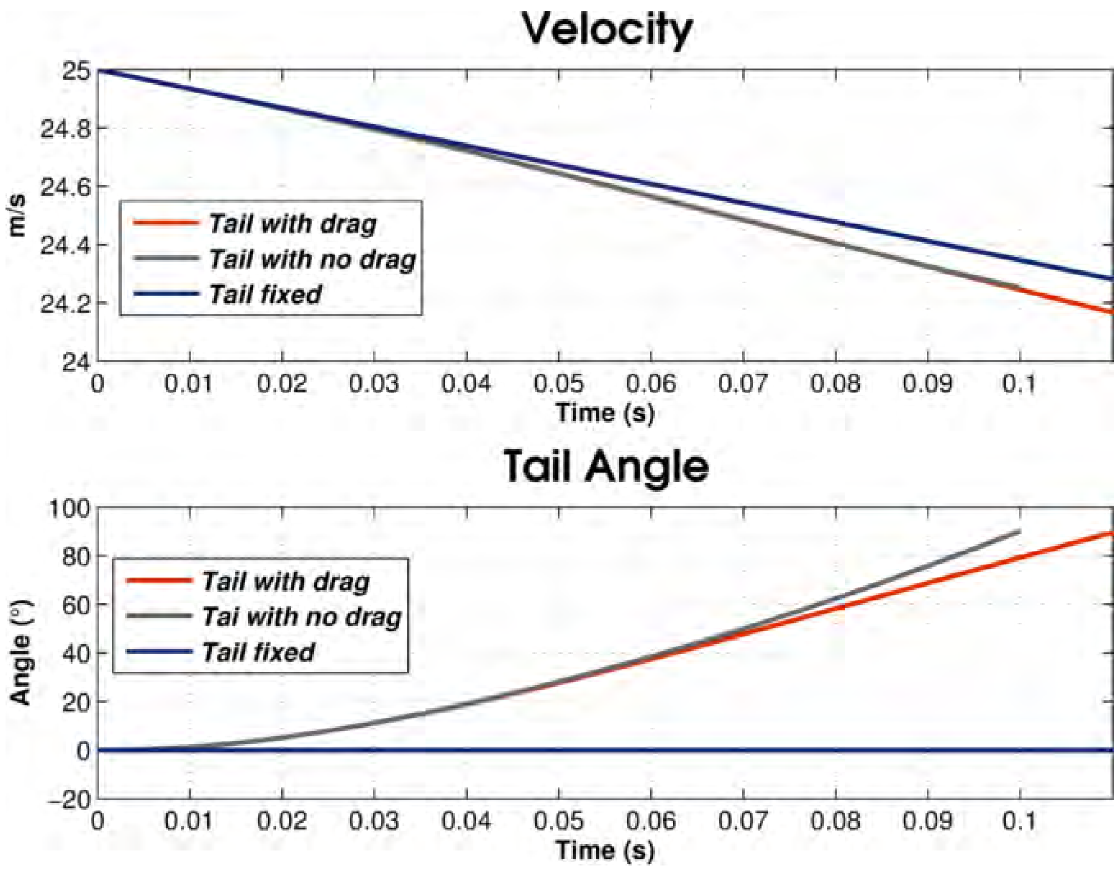

Figure 5.13: Top - Velocity obtained during simulation of the three configurations. Bottom – The resulting tail angles during the simulations.

The bottom of Figure 5.13 depicts the corresponding tail angles. It is evident that the effect of the aerodynamics is that the tail takes around 0.01 s longer to reach the of its travel range. An alternative view to this is that the aerodynamics provides the tail an extra 10°of actuation.

## 5.4 Discussion

Based on the inertia measurements performed by the Author and the publication by Hudson [16], the cheetah tail is, in fact, not as heavy as commonly believed. Moreover, with the centre of mass at approximately 25% of the total tail length from the base, the inertia is not as large as assumed and although its effects are significant, it has been shown that the aerodynamic forces also play a role in the tail motion's effect on the body

The wind tunnel testing is especially interesting as it illuminates the fact that the aerodynamic drag is quite significant. For the furry cylinder tests it was found to increase the effective area by 40%. Additionally, the tip of the tail also appeared to increase its effective area to 0.0145 m$^2$. For an equivalent cylinder diameter, this can be divided by the length of the morphometric tail model (0.24 m) to obtain an equivalent cylinder diameter of 0.6 m. The actual diameter of the tail rig varied from 0.03 m to 0.01 m as illustrated in Figure 5.14. This is significant as it implies that the fur increases the effective area without a weight penalty. The reader will note that to increase volume with muscle or bone would increase the total mass of the cheetah, degrading its acceleration performance.

The exact reasons for the increase in effective area and the observation of the constant drag coefficients remain open questions but are beyond the scope of this thesis. It is postulated that the fur roughness modifies the development of von Karmen vortices [83] so that the drag does not show rapid reduction at the point of boundary layer separation. Furthermore, the decrease in drag force for the tail tip can be attributed to the fur collapsing, thereby making the effective area appear smaller. The collapsing and bending of fur was not observed during the furry cylinder tests.

One might speculate if the cheetah could actuate the fur in order to make the individual hairs stand on end. This could negate the effects of the collapse of the fur observed previously. This hair-raising action is called piloerection [85] but is involuntary in felines and occurs when animals are scared, angry or cold [86]. Whether or not the cheetah is able to deliberately do this during manoeuvres should be investigated in future studies.

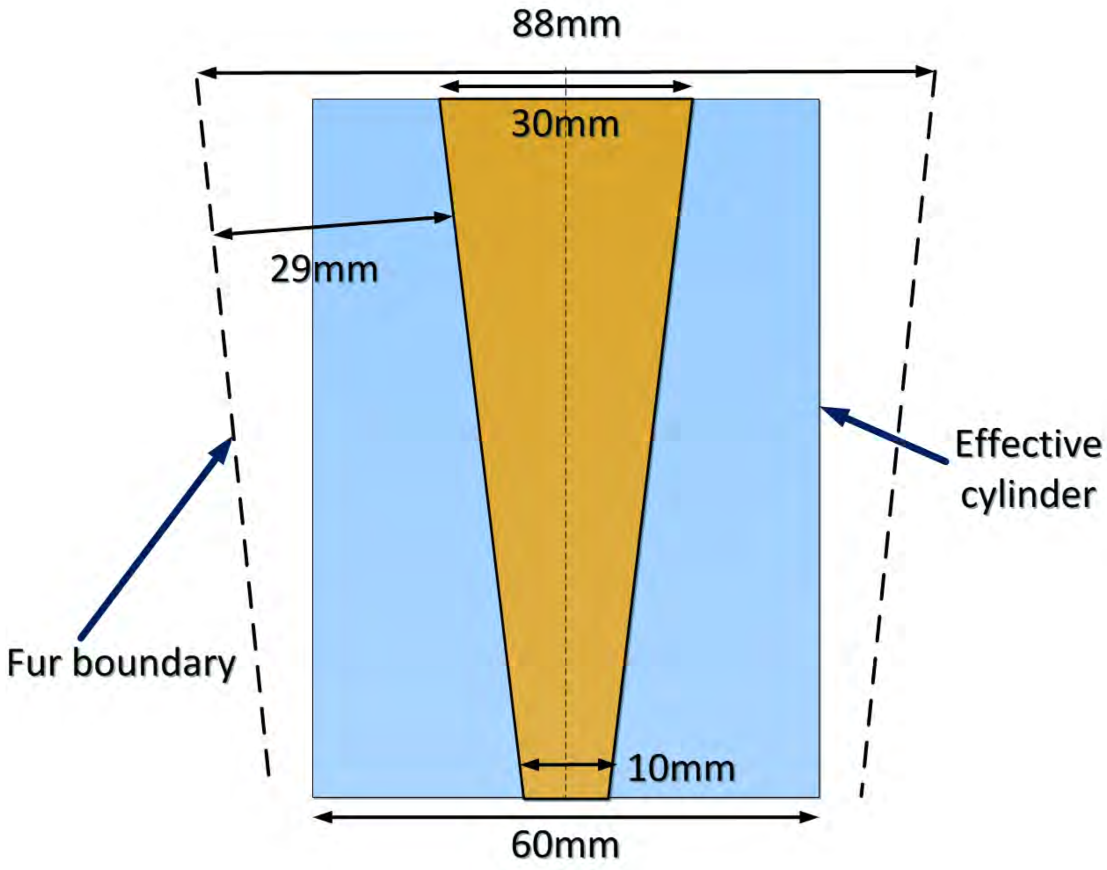

Figure 5.14: Tail tip model diagram shown. The mean fur length was 29mm, however the actual model width varied from 30mm to 10mm. The drag forces produced were equivalent to a cylinder of diameter of 60mm.

The simulation results support the idea that the aerodynamic forces will add to the effectiveness of the tail during manoeuvres. From Figure 5.10, it is evident that this is particular effective when the cheetah is moving at forward velocities during pitch or yaw motion. This supports the notion that the cheetah tail can be used as a rudder to give a large and sudden change of heading of the body. Moreover, the motion in the pitch axis can also contribute to the deceleration of the cheetah and loading of the hind legs, which have a dual effect of increasing pitch stability and lowering the peak forces on the front legs.

It its noted that the loading on the hind legs was not constant during tail actuation, but given that the tail was commanded in open loop, this is reasonable: When one examines the free body diagram of the cheetah body, the tail will also exert a reaction force on the body, which can under certain conditions become negative and cause this. With a feedback controller, this condition could be accounted for by appropriate input torque trajectories.

Lastly, the aerodynamic drag effects of the cheetah tail also imply that during the cone motion described in Chapter 4, the tail will theoretically be able to impart an indefinite roll torque as long as it can keep the cone at a constant velocity.

# Chapter 6

## Conclusion

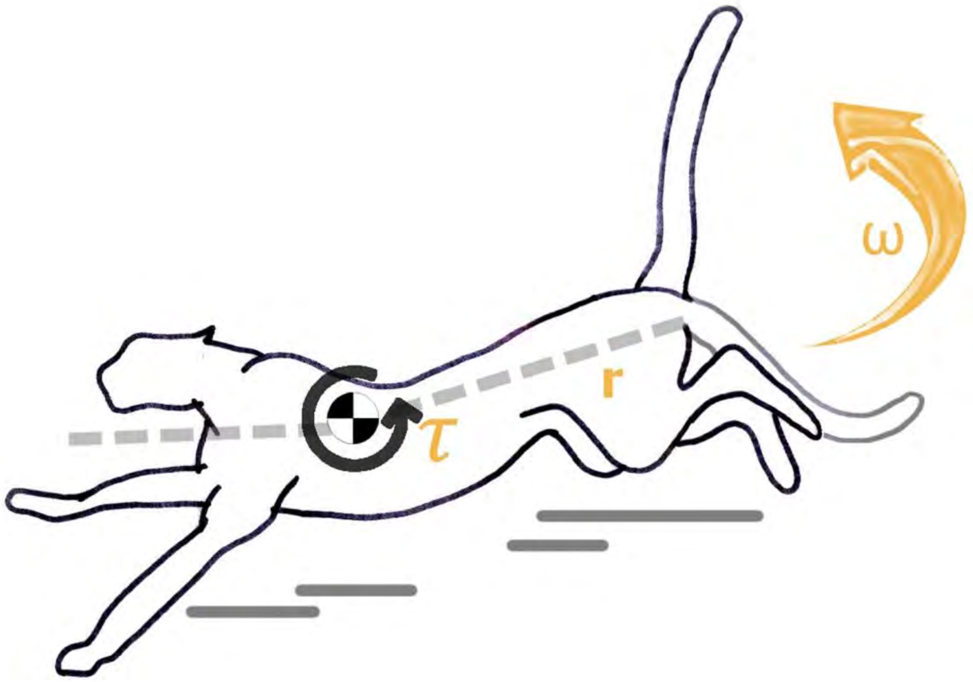

This chapter concludes the thesis with an overview of the work presented and highlights the significance of the research from which conclusions are drawn. Recommendations for future research on this particular topic are made and improvements are also proposed.

## 6.1 Summary of Findings

This thesis has presented a novel investigation to increase our understanding of the observed motions of the cheetah tail during rapid manoeuvres. The investigation was pursued via a multidisciplinary approach, utilizing mathematical modelling, physical experiments on robotic platforms and feedback controller design. It has been shown that the observed tail motions can indeed increase the manoeuvrability of the animal.

Chapters 2, 3 and 4 illustrate that disturbances due to excessive accelerations are a major constraint to the manoeuvrability of the cheetah. Particularly, numerical simulation results show that large centrifugal and linear accelerations cause instability during turn initiation at high-speed and rapid linear acceleration manoeuvres respectively. These occur during the stance phase of the cheetah gallop.

Under the common view that the tail is “heavy” and “high inertia” [4] [5] [6] [7] [8], the tail motions of the cheetah were initially hypothesised to stabilise these manoeuvres by means of inertial forces. In Chapter 2, it was demonstrated that the tail does impart a roll reaction torque on the body, and thereby stabilizes turn initiations at high-speed. This implies that the cheetah would be capable of counteracting significant centrifugal forces while running at high-speed. In this scenario, the cheetah could be employing the tail as an actuator as part of a roll rate feedback control loop. These manoeuvres are limited to short duration turns due to the angular constraints on the movement of the tail.

Chapter 3 demonstrated that the observed motions of the tail in the pitch axis generate a pitching reaction torque on the body. When actuated in this configuration, the tail provides a counteracting torque to prevent toppling from large acceleration forces. When employed in a pitch rate control loop, it is possible for the system to increase its acceleration manoeuvre capability. As in Chapter 2, these manoeuvres are also limited to short durations due to the angular constraints on the tail.

Wildlife documentaries reveal that the cheetah often swings its tail in a cone shape during longer duration turns. This trajectory of the tail is effectively a combination of pitching and yawing. In Chapter 4, it was demonstrated that this motion results in a continuous roll torque on the body. This signifies that the cheetah could possibly sustain a turn at high-speed for much longer, as the tail would not be limited by angular constraints, but only by muscle power limits.

The aforementioned chapters sought to understand the dynamic effects of the various observed tail motions. What is evident is that these particular motions provide an angular impulse on the body in the particular axis of the disturbance. These were done under the assumption that the tail has a high inertia, and as such the angular impulse was only produced by inertial forces. The validity of this assumption was investigated more fully in Chapter 5, when an opportunity arose towards the end of the project to weigh and measure a cheetah tail. Here, it was discovered that the tail actually has a lower inertia than initially assumed. However, wind tunnel tests illustrate that the cheetah fur exhibits significant aerodynamic drag. Numerical simulations revealed that despite the tail inertia being lower than predicted, it can still impart significant angular impulse on the body by using these aerodynamic forces as well. This implies that the cheetah tail could still be employed effectively as an actuator to stabilize rapid manoeuvres. It also is theorised that by swinging the tail at constant velocity in a cone, the cheetah is capable of producing an indefinite roll torque on the body.

These investigations resulted in two novel robotic platforms (*Dima I and Dima II*) being developed. These were compared, in simulation and through experimentation, to equivalent tail-less systems and by employing the tail motions discussed previously they were shown to be capable of increased manoeuvrability. These results have implications for future high-speed manoeuvrable robotic systems, where a tail could stabilize rapid movement transitions across uneven terrain.

## 6.2 Future Work

### *6.2.1 Biology*

This work has focused on developing models of the cheetah tail which are rigid. However, it is indeed possible for a distributed and compliant cheetah tail model to be developed based on the individual vertebral measurements presented in Section 5.1. This model could examine the dynamic effects that the compliance in the tail would have on the cheetah body. For example, it is plausible that by whipping the tail, much higher tail tip velocities will be experienced and this would increase the angular impulse considerably, especially as the tip of the tail has longer fur than the base.

Furthermore, the observations made from the cheetah tail video could be supplemented by a set of distributed sensors fastened along the tail itself. If used in conjunction with a collar such as in Wilson et al [2], it will certainly be possible to build a kinematic estimator to determine a more accurate picture of the tail dynamics in relation to the body motion. This will also allow one to test how well the simple templates developed in this dissertation can be “anchored” [54] into a higher fidelity cheetah model. This possibility is presently being researched by a Master’s project in the Electrical Engineering Department at the University of Cape Town.

### *6.2.2 Robotics*

The controllers presented in Chapters 2, 3 and 4 are designed for 2D planar models. One could incorporate these into a full 3D manoeuvre control system by switching in the relevant controller when a certain manoeuvre is being executed. This could possibly be implemented by a Sliding Mode Controller [61]. Another option is to design a full 3D manoeuvre controller. This could be formulated as a generalized optimal control problem, where the required torque on the body during different manoeuvres would need to be optimized. This could also be extended to include other inputs like propulsion and steering, as it is natural to infer that the cheetah would employ a Mulit-Input-Multi-Output (MIMO) control strategy of commanding leg force and tail motion in a coordinated manner. Optimal motion planning methods [60] could provide a solution to this problem as these methods could find an optimal trajectory while factoring in the constraints on the tail angles.

Inclusion of the aerodynamics of the tail in conjunction with inertial effects provides an interesting mechanical design problem as several compromises will need to be made e.g. speed vs. torque vs. tail weight, and more. In addition the control problem would be interesting, since to include the use of the aerodynamics as well as inertia may make the system uncontrollable in certain configurations especially when the moving at high-speed.

# References

[1] N. C. C. Sharp, "Timed running speed of a cheetah," *Journal of Zoology*, vol. 241, no. 3, pp. 493-494, March 1997.

[2] A.M Wilson et al., "Locomotion dynamics of hunting in wild cheetahs," *Nature*, vol. 498, pp. 185-189, 2013.

[3] National Geographic. (2012) Big Cats Initiative: Big Cat Facts. [Online]. http://animals.nationalgeographic.com/animals/big-cats/facts/

[4] Julia Layton. (2014) What Makes a Cheetah Run So Fast? [Online]. http://animals.howstuffworks.com/mammals/cheetah-speed1.htm

[5] Animal Planet. (2014) Animal Planet: Cheetah Spine and Tail. [Online]. http://www.animalplanet.com/tv-shows/animal-planet-presents/videos/survival-guide-serengeti-cheetah-spine-tail.htm

[6] Sabi Sabi Game Reserve. (2014) Sabi Sabi Wild Facts: The Cheetah. [Online]. http://www.sabisabi.com/wildfacts/cheetah

[7] M.G.L & Harvey, M Mills, *African Predators*. Cape Town: Struikers Publishers, 2001.

[8] S.E. Thompson, *Built for Speed: The Extraordinary, Enigmatic Cheetah*.: Lerner Pub Group, 1998.

[9] M Hilderbrand, "Further Studies on Locomotion of the Cheetah," *Journal of Mammalogy*, vol. 42, no. 1, pp. 84-91, 1961.

[10] National Geographic Channel. Cat Wars: Lion Vs. Cheetah. [Online]. https://natgeotv.com/za/cat-wars-lion-vs-cheetah

[11] Smithsonian Channel. This is Why You Can't Outrun a Cheetah. [Online]. http://www.smithsonianchannel.com/sc/web/video/titles/18351/this-is-why-you-cant-outrun-a-cheetah

[12] N.J Kohut, D.W Haldane, D Zarrouk, and R.S Fearing, "Effect of Inertial Tail on Yaw Rate of 45 gram Legged Robot," in *Proceedings of the Fifteenth International Conference on Climbing and Walking Robots and the Support Technlogies for Mobile Machines*, Baltimore, MD, USA, 2012.

[13] N.J Kohut, A.O Pullin, D.W Haldane, D Zarrouk, and R.S Fearing, "Precise Dynamic Turning of a 10 cm Legged Robot on a Low Friction," in *International Conference on Robotics and Automation (ICRA)*, Karlsruhe, 2013.

[14] A Patel and M Braae, "Rapid Turning at High Speed: Inspirations from the Cheetah's Tail," in *IEEE/RSJ International Conference on Intelligent Robots and Systems (IROS)*, Tokyo, 2013.

[15] A Patel and M Braae, "Rapid Acceleration and Braking: Inspirations from the Cheetah’s Tail," in *IEEE International Conference on Robotics and Automation*, Hong Kong, 2014.

[16] P.E. Hudson, "The structural and functional specialisation of locomotion in the cheetah (Acinonyx jubatus)," Royal Veterinary College, University of London, London, PhD Thesis 2011.

[17] Paul W Webb, "Maneuverability - General Issues," *IEEE Journal of Oceanic Engineering*, vol. 29, no. 3, pp. 547-555, 2004.

[18] D.L Jindrich and M Qiao, "Maneuvers during legged locomotion," *Chaos*, vol. 19, 2009.

[19] R. McNeill Alexander, *Principles of Animal Locomotion*.: Princeton University Press, 2006.

[20] T.C Angle, Gillette R.L, and W.H Weimar, "Kinematic Analysis of Maximal Movement Initiation in Greyhounds," *The Journal of the Australian Veterinary Association*, vol. 90, no. 3, pp. 60-68, 2012.

[21] S.B Williams, Huiling T, Usherwood J.R, Wilson, and A.M, "Pitch then power: Limitations to acceleration in quadrupeds," *Biology Letters*, vol. 5, pp. 610-613, 2009.

[22] T.C. Angle, R.L Gillette, and W.H. Weimar, "Caudal paw displacement during movement initiation and its implications for possible injusry mechanisms," *Veterinary and Comparitive Othropaedics and Traumatology*, vol. 25, pp. 397-401, 2012.

[23] S Williams, J.R Usherwood, K Jespers, A.J Channon, and A.M Wilson, "Exploring the mechanical basis for acceleration: Pelvic limb locomotor function during accelerations in racing greyhounds (Canis familiaris)," *The Journal of Experimental Biology*, vol. 212, pp. 550-565, 2009.

[24] R.M Walter and D.R Carrier, "Effects of fore-aft body mass distribution on acceleration

in dogs".

[25] R.M Walter and D.R Carrier, "Rapid Acceleration in Dogs: Ground Forces and Body Posture Dynamics," *The Jounral of Experimental Biology*, vol. 212, pp. 1930-1939, 2009.

[26] H Tan and A.M Wilson, "Grip and limb force limits to turning performance in competition horses," *Proceedings of the Royal Society*, vol. 278, pp. 2105-2111, 2010.

[27] C.A Moreno, *Biomechanics of non-steady locomotion: Bone loading, tunring mechanics and maneuvering performance in goats*. Cambridge, Massachusetts: Harvard University, 2010.

[28] D.L Jindrich, N.C Smith, K Jespers, and A.M Wilson, "Mechanics of cutting maneuvers by ostriches," *The Journal of Experimental Biology*, vol. 210, pp. 1378-1390, 2007.

[29] A.R and Sufka, K.M. Lammers, "Turning the Corner in Quadrupedal Arboreal Locomotion: Kinetics of Changing Direction While Running in the Siberian Chipmunk (Tamias sibiricus)," *Journal of Experimetnal Zoology*, no. 319, pp. 99-112, 2013.

[30] J. W., Mills, M. G., Wilson, R. P., Peters, G., Mills, M. E., Speakman, J. R.,. & Scantlebury, M. Wilson, "Cheetahs, Acinonyx jubatus, balance turn capacity with pace when chasing prey," *Biology Letters*, vol. 9, no. 5, September 2013.

[31] P.E. Hudson et al., "Functional Anatomy of the Cheetah Hindlimb," *Journal of Anatomy*, vol. 218, no. 4, pp. 363-374, 2011.

[32] P.E. Hudson et al., "Functional Anatomy of the Cheetah Forelimb," *Journal of Anatomy*, vol. 218, no. 4, pp. 375-385, 2011.

[33] A Bowling, "Impact forces and agility in legged robot locomotion," *Journal of Vibration and Control*, vol. 17, no. 3, pp. 335-346, 2010.

[34] H Kazemi, V.J Majd, and M.M Moghaddam, "Modeling and robust backstepping control of an underactuated quadruped robot in bounding motion," *Robotica*, pp. 1-17, 2012.

[35] D.P Krasny and D.E Orin, "Evolution of Dynamic Maneuvers in a 3D Galloping Robot," in *IEEE International Conference on Robotics and Automation*, Orlando, Florida, 2006.

[36] X Wang, M Li, P Wang, and L Sun, "Running and Turning Control of a Quadruped Robot with Compliant Legs in Bounding Gait," in *IEEE International Conference on Robotics and*

*Automation*, Shanghai, China, 2011.

[37] Boston Dynamics. (2012) CHEETAH- Fastest Legged Robot. [Online]. http://www.bostondynamics.com/robot_cheetah.html

[38] A Jusufi, D.T Kawano, T Libby, and R.J Full, "Righting and Turning in mid-air using appendage inertia: Reptile tails, analytical models and bio-inspired robots," *Bioinspiration & Biomimetics*, vol. 5, pp. 1-12, 2010.

[39] R Libby et al., "Tail-assisted pitch control in lizards, robots and dinosaurs," *Nature*, vol. 481, pp. 181-186, 2012.

[40] C Walker, Vierck C, and L Ritz, "Balance in the cat: role of the tail and effects of sacrocaudal transection," *Behavioural Brain Research*, vol. 91, no. 1, pp. 41-47, 1998.

[41] G.A Batholomew and H.H Caswell, "Locomotion in Kangaroo Rats in its adaptive significance," *Journal of Mammology*, vol. 32, pp. 155-169, 1951.

[42] S.G. Larson and J.T. Stern, "Maintenance of aboce-branch balance during primate arboreal quadrapedalism: coordinated use of forearm rotators and tail motion," *American Joirnal of Physical Anthropology*, vol. 129, no. 1, pp. 71-81, 2006.

[43] E Chang-Siu, T Libby, M Tomizuka, and Full R.J, "A Lizard-Inspired Active Tail Enables Rapid Maneuvers and Dynamic Stabilization in a Terrestrial Robot," in *IEEE/RSJ International Conference on Intelligent Robots and Systems*, San Francisco, California, 2011.

[44] A.M Johnson, T Libby, and E Chang-Siu, "Tail Assisted Dynamic Self Righting," in *Proceedings of the Fifteenth International Conference on Climbing and Walking Robots and the Support Technologies for Mobile Machines*, Baltimore, MD, USA, 2012.

[45] J Zhou et al., "Controlling Aerial Maneuvering of a Miniature Jumping Robot Using Its Tail," in *IEEE/RSJ International Conference on Intelligent Robotics and Systems (IROS)*, Tokyo, 2013, pp. 3802-3807.

[46] R Briggs, J Lee, M Haberland, and S Kim, "Tails in Biomimetic Design: Analysis, Simulation and Experiment," in *IEEE/RSJ International Conference on Intelligent Robots and Systems*, Vilamoura, Algarve, Portugal, 2012.

[47] E Chang-Siu, T Libby, M Brown, R.J Full, and M Tomizuka, "A nonlinear feedback

controller for aerial self-righting by a tailed robot," in *International Conference on Robotics and Automation (ICRA)*, Karlsruhe, 2013.

[48] A De, A. M Johnson, and D.E Koditschek, "Monopedel Hopping with a Leg and a Tail," in *Dynamic Walking*, Zurich, 2014.

[49] C Casarez, I Pnenskiy, and S Bergbreiter, "Using an Inertial Tail for Rapid Turns on a Miniature Legged Robot," in *IEEE International Conference on Robotics and Automation (ICRA)*, Karlsruhe, 2013, pp. 5469 - 5474.

[50] N.J Kohut, D Zarrouk, K. C Peterson, and R. S. Fearing, "Aerodynamic Steering of a 10 cm High-Speed Running Robot," in *IEEE/RSJ International Conference on Intelligent Robots and Systems (IROS)* , Tokyo, 2013, pp. 5593 - 5599.

[51] A Patel and M Braae, "An Actuated Tail Increases Rapid Acceleration Manoeuvres in Quadruped Robots," in *International Joint Conferences on Computer, Information, Systems Sciences and Engineering*, 2012.

[52] R,J Full, T Kubow, J Schmitt, P Holmes, and D Koditschek, "Quantifying Dynamic Stability and Maneuverability in Legged Locomotion," *Integrated and Comparative Biology*, vol. 42, no. 1, pp. 149-157, 2002.

[53] D. Weihs, "Stability Versus Maneuverability in Aquatic Locomotion," *Integrative Comparative Biology*, vol. 42, no. 1, pp. 127-134, 2002.

[54] R.J. Full and D. Koditschek, "Templates and Anchors: Neuromechanical hypotheses of legged locomotion on land," *Journal of Experimental Biology*, vol. 202, no. 23, pp. 3325-3332, 1999.

[55] P. Holmes, R.J Full, D. Koditschek, and J. Guckenheimer, "The dynamics of legged locomotion: Models, analysis and challenges," *SIAM Rev.*, vol. 48, no. 2, pp. 206-304, 2006.

[56] D.T Greenwood, *Advanced Dynamics*. Cambridge: Cambridge University Press, 2003.

[57] R.M Murray, Z Li, and S.S Sastry, *A Mathematical Introduction to Robotic Manipulation*.: CRC Press, 1994.

[58] B Siciliano, L Sciavicco, L Villani, and G Oriolo, *Robotics: Modelling, Planning and Control* , 1st ed.: Springer, 2009.

[59] R. Tedrake. (2009) Fully Actuated vs. Underactuated Systems (Course Notes).

[60] A Shkolnik and R Tedrake, "High-Dimensional Underactuated Motion Planning via Task Space Control," in *IEEE International Conference on Intelligent Robots and Systems*, 2008.

[61] J.J.E Slotine and W Li, *Applied Nonlinear Control*. New Jersey: Prentice-Hall International, 1991.

[62] J Betts, *Practical Method sfor Optimal Control and Estimation using Nonlinear Programming*, 2nd ed.: Society for Industrial & Applied Mathematics, 2009.

[63] M Srinivasan, "Trajectory Optimzation: A brief Introduction (Workshop)," in *Dynamic Walking Conference*, 2010.

[64] M & Ruina, A Srinivasan, "Computer Optimization of a Minimal Biped Model Discovers Walking and Running," *Nature*, vol. 5, no. 439, pp. 72-75, September 2006.

[65] M Haberland, J.G.D Karssen, S Kim, and M Wisse, "The Effect of Swing Leg Retraction on Running Energy Efficiency," in *IEEE/RSJ International Conference on Intelligent Robots and Systems (IROS)*, San Francisco, 2011, pp. 3957-3962.

[66] C,M & Hurst, J.W Hubicki, "Running on Soft Ground: Simple Energy-Optimal Disturbance Rejection," in *Proceedings of the Fifteenth International Conference on Climbing and Walking Robots and the Support Technologies for Mobile Mcahines*, Baltimore, 2012, pp. 543-547.

[67] P.E. Hudson, S.A. Corr, and A.M. Wilson, "High speed galloping in the cheetah (Acinonyx jubatus) and the racing greyhound (Canis familiaris): spatio-temporal and kinetic characteristics. ," *Journal of Experimental Biology*, vol. 215, no. 14, pp. 2425-2434, 2012.

[68] A Patel et al., "The Cheetah Tail: Aerodynamics and Inertia of a Torque Actuator," *Nature*, (Under Review).

[69] A.A Biewener, "Maneuverability versus Stability," in *Animal Locomotion*.: Oxford University Press, 2003, p. 58.

[70] Nat Geo Wild, I Predator: Cheetah Vs. Antelope, 2010.

[71] FreeRTOS. (2013) FreeRTOS. [Online]. http://www.freertos.org/

[72] M.A. Sotelo, "Lateral Control Stratgy fo Autonmous Steering of Ackerman-like Vehicles," *Robotics and Autonomous Systems*, vol. 45, pp. 223-233, 2003.

[73] L.L Marker and A.J Dickman, "Morphology, Physical Condition and Growth of the Cheetah (Acinonyx Jubatus) ," *Journal of Mamalogy*, vol. 84, no. 3, pp. 840-850, 2003.

[74] F Mainardi and G Spada, "Creep, Relaxation and Viscosity Properties for Basic Fractional Models in Rheology," *The European Physical Journal, Special Topics*, vol. 193, pp. 133-160, 2011.

[75] D.E Kirk, *Optimal Control Theory: An Introduction*. Mineola, New York: Dover Publications, 2004.

[76] Z Ugray et al., "Scatter search and local NLP Solvers: A Multistart Framework for Global Optmization," *INFORMS Journal on Computing*, vol. 3, no. 19, pp. 328-340, 2007.

[77] J Coetser, "Low-cost Inertial Navigation System," University of Cape Town, Cape Town, Honours Thesis 2013.

[78] L.J Rosenzweig, *Anatomy of the cat: Test and Dissection Guide*. Dubuque: Brown Publishers.

[79] J.E Crouch, *Text-atlas of Cat Anatomy*. Philadelphia: Lea & Febiger, 1969.

[80] R.M. Alexander, "Dinosaur Biomechanics," *Proceedings of the Royal Society of Biological Sciences*, no. 273, pp. 1849-1855, 2006.

[81] J Dowling J, J,L Durking, and D,M Andrews, "The uncertainty of the pendulum method for the determination of the moment of inertia.," *Medical Engineering and Physics*, vol. 28, no. 8, pp. 837-841, October 2006.

[82] J Anderson, *Fundamentals of Aerodynamics* , 5th ed.: McGraw-Hill, 2010.

[83] J.F Douglas, *Fluid Mechanics*, 4th ed.: Prentice Hall, 2000.

[84] W.F Lindsey, *Drag of Cylinders of Simple Shapes*.: NACA, 1938.

[85] J.W.S. Bradshaw, *The Behaviour of the Domestic Cat*, 1st ed.: CABI, 1992.

[86] L. P. Case, *Canine and Feline Behavior and Training: A Complete Guide to Understanding our Two Best Friends*, 1st ed.: Cengage Learning, 2009.

[87] T.G West et al., "Power Output of Skinned Skeletal Muscle Fibres From the Cheetah (Acinonyx jubatus)," *Journal of Experimental Biology*, vol. 15, no. 216, pp. 2974-2982, August 2013.